Thesis for the Degree
of Doctor

Study of the Nuclear Stopping in Isospin Asymmetric Nuclear Collisions at 0.4A and 1.5A GeV

by

Young Jin Kim

Department of Physics

Graduate School

Korea University

June 21, 2004

Abstract

In this thesis, we investigate the nuclear stopping phenomenon in $^{96}_{44}$Ru($^{96}_{40}$Zr) on $^{96}_{44}$Ru($^{96}_{40}$Zr) collisions at bombarding energies of $0.4A$ and $1.528A$ GeV by using the FOPI detector at the SIS/GSI. First of all, the centrality dependence of proton and deuteron rapidity distributions in Ru + Ru collisions at both energies is presented. Then the degree of nuclear stopping at both energies is studied by two observables of the isospin tracer method. For the most central collisions, the experimental results at both energies show partial transparency and incomplete mixing of the projectile and target nuclei. The effect is increasing when beam energy goes from $0.4A$ to $1.528A$ GeV. Data are compared with Isospin Quantum Molecular Dynamics(IQMD) calculations under various assumptions on both the compressibility of the nuclear Equation-of-State(EoS) and the nucleon-nucleon cross section in medium. The rapidity distributions of protons and deuterons for the most central collisions at $0.4A$ GeV can be reproduced by the IQMD calculation with the hard EoS and a free nucleon-nucleon cross section. The IQMD calculation with the soft EoS and the reduced free nucleon-nucleon cross section can reproduce the proton rapidity distribution for the most central collisions at $1.528A$ GeV. However, the IQMD model does not have the sensitivity to reproduce the isospin tracing observables at $1.528A$ GeV.

Contents

List of Figures

List of Tables

Chapter 1

Introduction

Heavy-ion collisions are the unique tool to produce a large volume of nuclear matter at high temperatures and densities in the laboratory [1, 2, 3, 4]. The variation of density with energy allows exploring nuclear matter in entirely uncharted region in hadron phase diagram, which is shown in figure 1.1. The production of such an abnormal(hot and/or dense) state enables us to investigate not only its gross properties of the fireball, but also the basics of Quantum Chromodynamics(QCD), which is the theory of strong interaction. At beam energies of 1 - 2A GeV, two to three times the normal nuclear density can be reached by nucleus-nucleus collisions at early times, but the condition is predicted to be merely kept only about 15 fm/c. If the global equilibration can be established in such a short time interval is yet an open question [2, 5]. Presently, heavy-ion collision experiments provide data in a very broad energy range from the SIS/GSI($\sqrt{s} \simeq 2A$ GeV), the AGS/BNL($\sqrt{s} \simeq 10A$ GeV), the SPS/CERN($\sqrt{s} \simeq 20A$ GeV), and the RHIC/BNL($\sqrt{s} = 200A$ GeV). Heavy-ion reaction at the SIS and the AGS generates a relatively low temperature and high baryonic density fireball, but a relatively high temperature and low baryonic density fireball is expected to be created at the RHIC.

In figure 1.2, the schematic view of nucleus-nucleus collision and the simulated reaction event in Au + Au at 2A GeV are given. Upper left plot of figure 1.2 shows the definitions of impact parameter(b), participants which are nucleons in the overlap region, and spectators which are nucleons who do not directly participate in the reaction. According to the transport model

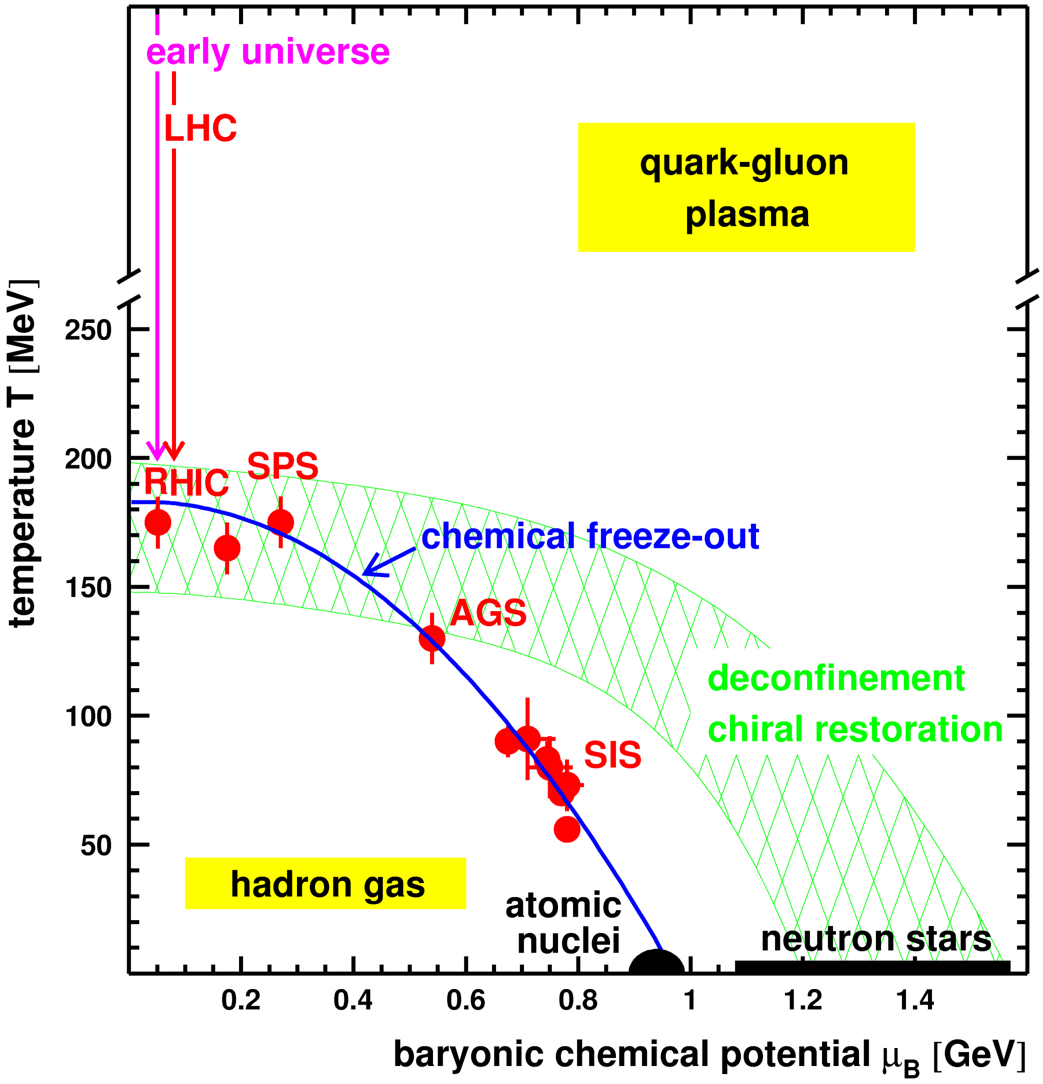

Figure 1.1: Phase diagram of nuclear matter in terms of temperature T and the baryonic chemical potential μ_B and its relation to heavy-ion collisions.

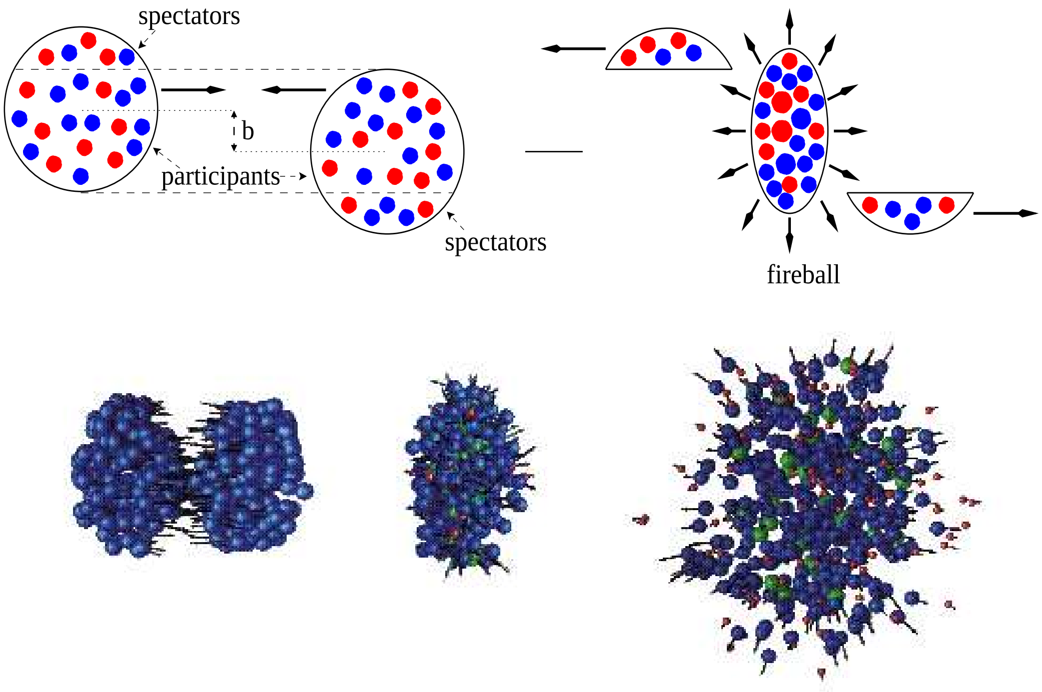

Figure 1.2: Schematic view of nucleus-nucleus collision(top) and the simulated reaction event in Au + Au at $2A$ GeV by the IQMD(bottom).

calculations, participant nucleons create the fireball(the hot and dense nuclear matter) and the fireball becomes cool and freeze-out to the final state hadrons about 10 - 15 fm/c after colliding. Lower plot of figure 1.2 is time span view of heavy-ion reactions. Heavy-ion collisions are such a complex multi-body reactions and it can make extremely excited state of hadronic matter which occurs phase transition to the quark-gluon plasma(QGP) [6].

Equation-of-State(EoS) and Heavy-Ion Physics at the GSI

Figure 1.3 shows the energy per baryon(T=0) as a function of the normalized baryonic density($\rho/\rho_\circ$) in a relativistic hadron transport model calculations which is based on Boltzmann-Uehling-Uhlenbeck(BUU) [7], where $\rho_\circ$ is the normal nuclear matter density of 0.17/fm^3. In figure 1.3, the solid line corresponds to the hard EoS, the dashed line to the soft EoS, while the dashed-dotted line results from the hard EoS with the second-order phase transition. The result of the calculations shows that the stiffer increase can be expected for the hard EoS. In addition, figure 1.3 shows that there is possibility to change of the EoS from hard to soft or vice versa if the system suffers the onset of a phase transition to new state. According to G. Peilert *et al.* [8], the momentum dependence of the nuclear interaction in infinite cold nuclear matter does not influence on the EoS, but they claim that the momentum dependent interaction(MDI) leads to an additional repulsion between nucleons in heavy-ion collisions. Such the MDI reduces the yield of pions and kaons substantially, while the transverse momentum transfer for beam energies $\geq$ 400A MeV increases. Therefore, the MDI leads the nonequilibrium effects in heavy-ion collisions and the determination of the EoS can not be simply extracted from experimental data [9, 10].

The EoS can be changed by its compressibility [11]:

$$K = 9\rho^2 \frac{\partial}{\partial \rho^2} \left(\frac{E}{A}\right) |_{\rho=\rho_\circ} \tag{1.1}$$

where the value of K is used to be 380 MeV for the hard EoS and 200 MeV for the soft EoS. The functions shown in figure 1.3 are expected to be extracted from experiments. Recently, the isospin effect in heavy-ion collision experiment is investigated [12, 13, 14, 15, 16, 17]. The EoS of neutron rich matter

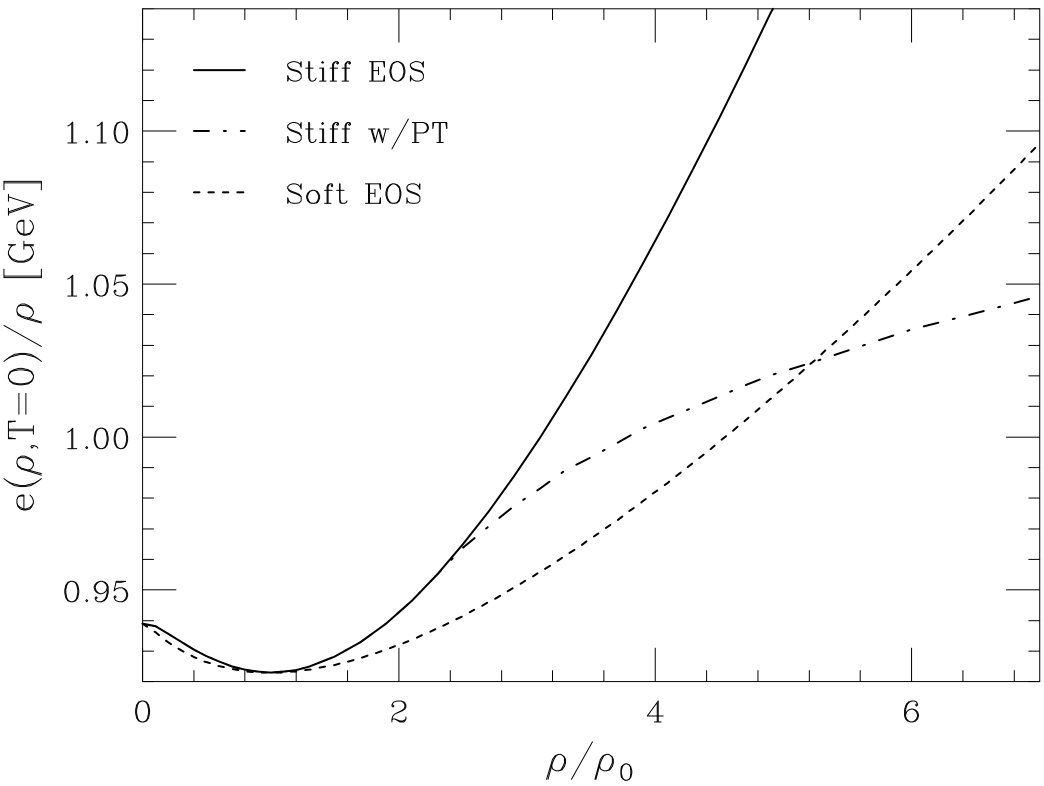

Figure 1.3: Energy per baryon as a function of the normalized baryonic density($\rho/\rho_\circ$) [7]. See the text for more details.

of isospin asymmetry, $\delta \equiv (\rho_n - \rho_p)/(\rho_n + \rho_p)$, can be written as

$$e(\rho, \delta) = e(\rho, 0) + E_{sym}(\rho)\, \delta^2 + O(\delta^4), \tag{1.2}$$

where $e(\rho, 0)$ is the energy per nucleon in isospin symmetric nuclear matter and E_{sym} is the density dependent nuclear symmetry energy [18]. In experimental side, this effect has been studied at low energies only(up to 53A MeV), and it will be extended to higher beam energy experiments.

In the SIS energy regime, one of the main goals of heavy-ion collisions is the determination of the compressibility K of the nuclear Equation-of-State which is essential for the understanding of the dynamics of supernova and the formation of neutron stars. Many physics observables are proposed to be sensitive to K, accordingly, various observables in heavy-ion collisions have been studied. For instance, the hydrodynamic behavior(collective motion) of bulk nuclear matter(flow) [19, 20, 21, 22, 23, 24, 25] and the in-medium properties of hadrons in a hot and dense environment [26, 27, 28, 29, 30, 31, 32] have been extensively investigated. However, collective flow phenomena are proven to be strongly affected by the momentum dependent part of the mean field so that the former one can not be simply disentangled [9, 10]. Similarly, other proposed observables for estimating the nuclear Equation-of-State have been discovered unreliable with various reasons. Therefore, the determination of the nuclear Equation-of-State is still under debate.

Isospin Quantum Molecular Dynamics

The Isospin Quantum Molecular Dynamics(IQMD) model is a nonequilibrium transport model which considers the isospin degree of freedom for nucleon-nucleon cross section, the Coulomb interaction, the Yukawa potential, and the momentum dependence of the interaction [11, 33, 34]. In the model, the nucleons are represented by Gaussian wave packet and classical equations-of-motion are used to propagate their centroids in an interaction potential. In the potential, there is local term which can be parameterized with a potential depending on the density and this allows a direct connection to the nuclear Equation-of-State. The calculations are based on event-by-event and the reactions are treated as binary collisions between nucleons with Pauli exclusion principle.

Nuclear Stopping

The degree of nuclear stopping in heavy-ion collisions is one of the essential observables which are necessary to understand the basic reaction dynamics: it is crucial information for estimating the energy and particle densities of the compressed nuclear matter at an early stage of the participant fireball. It is also closely related to the question of whether the (at least) local equilibrium model [35, 36, 37] is valid or a more elaborate nonequilibrium transport approach [5, 9, 38] is required for a description of the fireball.

The issue of equilibration is expected to be influenced by the in-medium effects(such as of hadron mass as well as more basic Pauli blocking and Fermi motion) on the initial scattering processes, by early soft deflections in the momentum dependent mean fields, and by finite size(corona) effects. An understanding of all these effects is a prerequisite for a quantitative extraction of the Equation-of-State from nucleus-nucleus collisions.

In many cases, nuclear stopping has been studied by baryon rapidity distributions at various beam energy ranges and collision system size. Observables of interest are the width of rapidity distributions and the overall shape of the source [25, 39, 40, 41, 42, 43, 44, 45]. At beam energies larger than $1A$ GeV, the experimental data show that these distributions are not compatible with the assumption of an isotropically expanding source. The origin of this observation has become one of the most discussed subjects, since very similar rapidity distributions can be produced by transparency or the longitudinal expansion after thermal equilibrium of projectile and target nucleons.

In two different transport models, contradictory predictions were come out. The first one is the IQMD and the model which predicts that the transparency effect can be seen at $0.15A$ and $1.5A$ GeV and it is more pronounced at $1.5A$ GeV in ^{50}Cr + ^{48}Ca collisions [46]. However, the results of the coupled-channel Boltzmann-Uehling-Uhlenbeck(CBUU) model with $^{96}_{44}$Ru + $^{96}_{40}$Zr reactions at $0.4A$ and $1.5A$ GeV showed that the transparency effect became smaller for higher beam energy [47]. Common to both models are the transparency effect at both energies.

Kinematical Variables

In the presentation of the analysis results in heavy-ion collisions, there are some commonly used kinematical variables. One is the so called rapidity in the laboratory frame defined by

$$y_{Lab} = \frac{1}{2} \ln \left(\frac{E + P_z}{E - P_z} \right) = \frac{1}{2} \ln \left(\frac{1 + \beta_z}{1 - \beta_z} \right), \tag{1.3}$$

where E is the energy of the particle and P_z, β_z are momentum and velocity on the z-axis of the particle, respectively. Here, natural units $\hbar$=c=1 are used. Under a boost in the z-direction to a frame with velocity β, y_{Lab} can be simply shifted by $\tanh^{-1}\beta$ without changing the distribution shape. Therefore, the shape of the rapidity distribution dN/dy_{Lab} is invariant under Lorentz transformation. In FOPI, the normalized rapidity is commonly used which is defined by

$$y^{(0)} = \frac{y_{Lab}}{y_{cm}} - 1, \tag{1.4}$$

where y_{cm} is the center-of-mass rapidity. For the mass symmetric system, -1, 1, and 0 correspond to target, projectile, and the center-of-mass rapidities, respectively. The center-of-mass rapidity is usually called the mid-rapidity.

We also use often the transverse momentum of the particle:

$$P_t = Psin\,(\theta) \tag{1.5}$$

where P is momentum of the particle and θ is the emission polar angle. Once particles are identified its transverse momentum can be normalized by the following formula:

$$P_t^{(0)} = \frac{P_t}{m \cdot \beta_{cm} \cdot \gamma_{cm}} \tag{1.6}$$

where m is the mass of the particle, and β_{cm} and γ_{cm} are the velocity and Lorentz gamma factor of the center-of-mass, respectively. In addition, the spectrum of the particle is represented in its invariant form. The invariant cross section can be written as

$$E\frac{d^3\sigma}{d^3P} = \frac{d^3\sigma}{d\phi dy P_t dP_t} = \frac{d^2\sigma}{2\pi P_t dP_t dy} = \frac{d^2N}{2\pi P_t dP_t dy}, \tag{1.7}$$

where ϕ is the azimuthal angle.

In this thesis, FOPI detector components and experimental setup in 1996 will be described in chapter 2 and the method of analysis will be explained in chapter 3 in detail. The analysis results and its physics discussions will be presented in chapter 4. In chapter 5, conclusions of the work will be given. The part of the results at 0.4A GeV in this thesis was published and one can find it in reference [48].

Chapter 2

Experiment

In this chapter, the FOPI detector components and the experimental setup for the isospin experiment in 1996 is explained.

2.1 Beam and Target

The accelerator facility at Gesellschaft für Schwerionenforschung(GSI) in Darmstadt, Germany consists of three components. The Universal Linear Accelerator(UNILAC) provides ions for an experiment at low energies and it, also, acts as a pre-accelerator for Schwerionensynchrotron(Heavy-Ion Synchrotron, SIS). The Experimental Storage Ring(ESR) makes it possible to cool ion beams and use them for internal ring experiments, and the SIS accelerates heavy-ion beams up to $2A$ GeV.

For heavy-ion beams, the available beam kinetic energy per atomic mass is described by the formula

$$E_{beam}/A = m_p c^2 \left(\sqrt{1 + \left(\frac{B\rho c}{m_p c^2} \frac{Q}{A} \right)^2} - 1 \right) \tag{2.1}$$

where m_p is the mass of proton, $B\rho$ is the magnetic rigidity of the synchrotron, and Q and A are the charge and the mass number of heavy-ion beams. Overall view of accelerator facilities and experimental areas is shown in figure 2.1, and some important parameters of the SIS are demonstrated in figure 2.2.

In 1996, the isospin experiment was performed by the FOPI collaboration with various energy(0.4, 1.0, 1.528, 1.69A GeV) $^{96}_{44}$Ru and $^{96}_{40}$Zr beams on $^{96}_{44}$Ru and $^{96}_{40}$ZrO$_2$ targets. $^{96}_{44}$Ru target of 431 mg/cm^2 was supported in a very thin 10 mm diameter Al ring and it contained 96.52% A=96 species in isotope abundances. $^{96}_{40}$ZrO$_2$ target of 507 mg/cm^2, which had Zr components of 380 mg/cm^2 with 95.6% A=96 in isotope abundances, was filled into 10 mm diameter and held between two Kapton foils of 3.65 mg/cm^2 each. Both targets were designed to have 1% interaction probability in a given minimum beam intensity and a given thickness of the target. The summary of the projectile-target combinations for the isospin experiment is given in Table 2.1.

E_{beam} (A GeV)	Beam	Target
0.4/1.0/1.528	$^{96}_{44}$Ru	$^{96}_{44}$Ru
	$^{96}_{44}$Ru	$^{96}_{40}$ZrO$_2$
	$^{96}_{40}$Zr	$^{96}_{44}$Ru
	$^{96}_{40}$Zr	$^{96}_{40}$ZrO$_2$
1.69	$^{96}_{44}$Ru	$^{96}_{44}$Ru
	$^{96}_{44}$Ru	$^{96}_{40}$ZrO$_2$

Table 2.1: Summary of the isospin experiment in 1996.

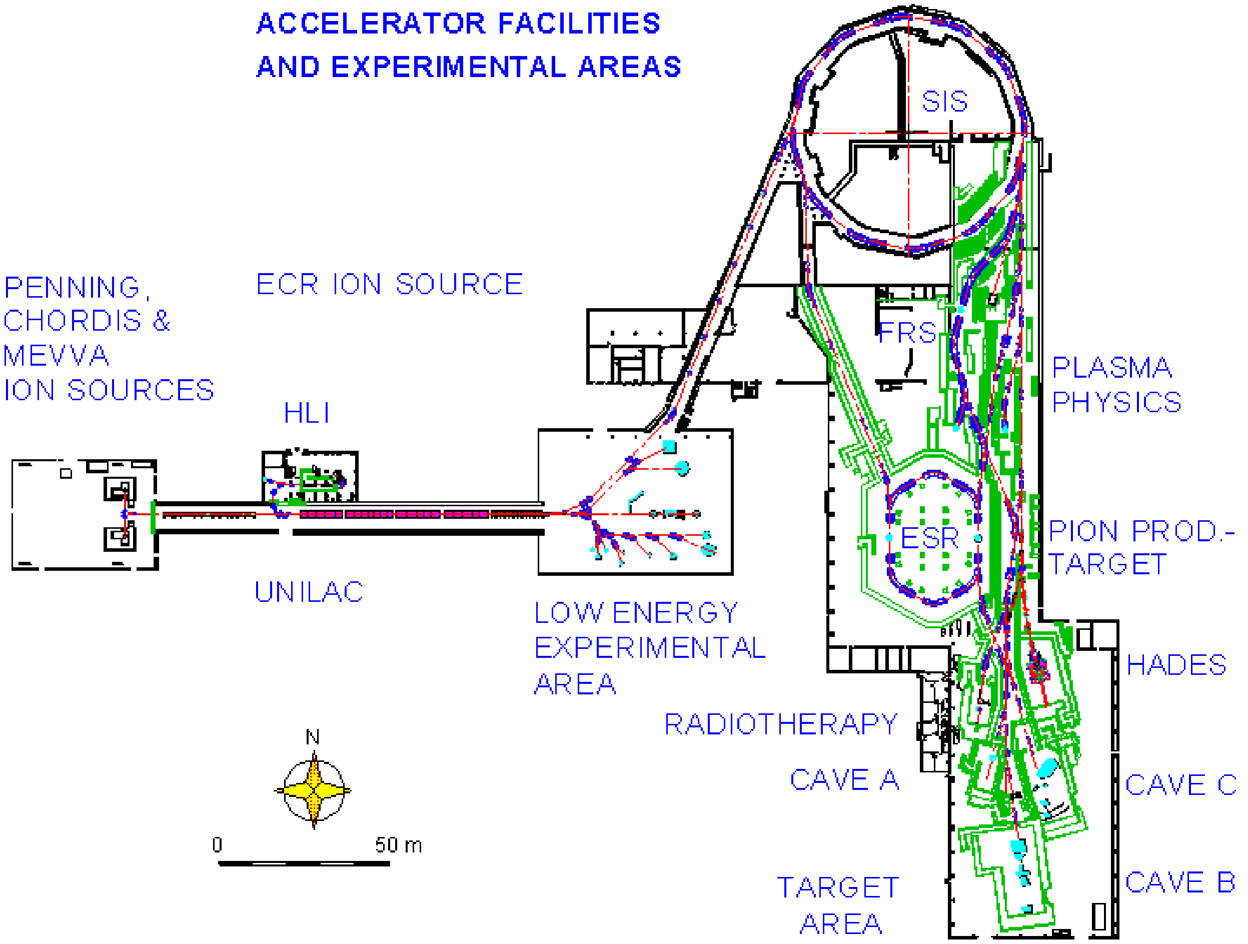

Figure 2.1: Overall view of accelerator facilities and experimental areas at the GSI: The FOPI detector is located in cave B.

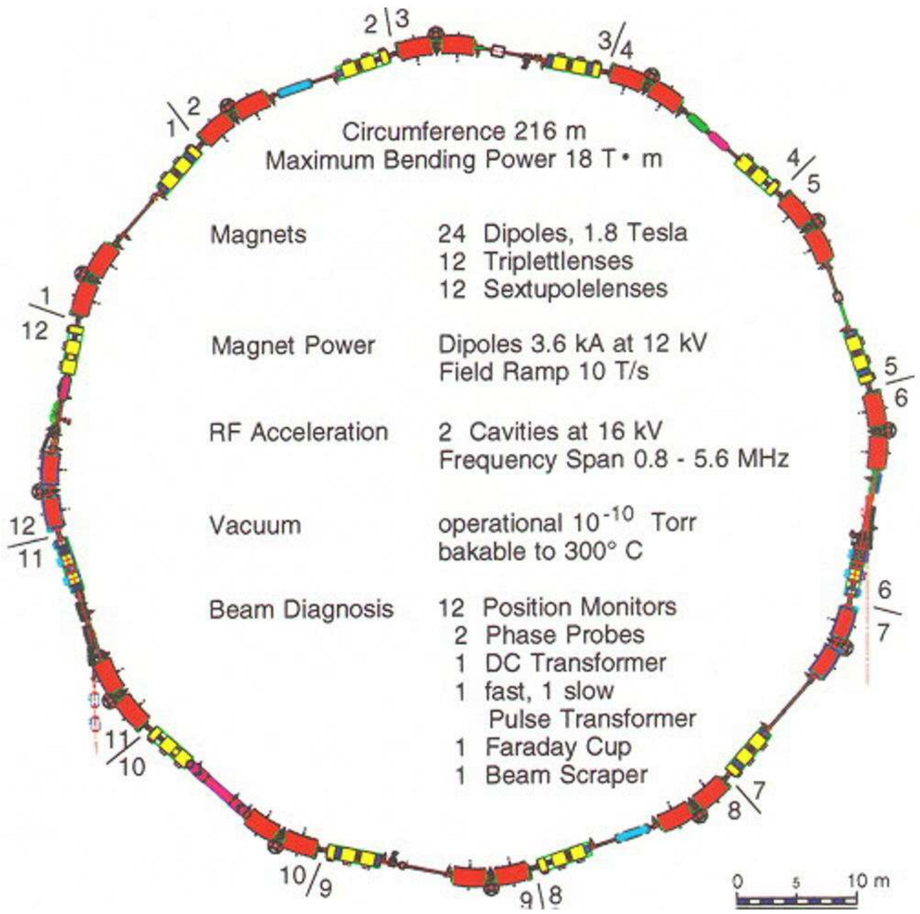

Figure 2.2: Details of the SIS.

Two major goals of the isospin experiment are

1. The degree of projectile and target nucleon mixing study: investigation of nucleon propagation in medium with N/Z measurements.

2. Strangeness production: investigation of the yield and the flow of strange particles.

The main reason of using $^{96}_{44}$Ru and $^{96}_{40}$Zr is that they are stable isobaric nuclei with the largest possible N/Z difference in the Periodic Table. In this thesis, all of physics results are focused on the delivering information of the first major goal of the isospin experiment namely the nuclear stopping phenomenon. In order to reduce the statistical errors and eliminate the systematic errors as much as possible in the physics results, it is required to accumulate more collision statistics and combine four different sets of beam-target combinations. Therefore, data at $0.4A$ and $1.528A$ GeV are analyzed in this thesis.

2.2 FOPI Detector

FOPI is the fixed target experiment of measuring event by event charged particles at the SIS energy range(0.1 - 2A GeV). The detector at this energy regime is requested to have very low detection threshold, large dynamic range, high granularity, and good particle identification in both charge and mass in order to get almost complete possible event characterization [49]. Due to the various requirements for the different particle type, the FOPI detector is divided into several sub-detector systems which have nearly complete azimuthal symmetry [50]. The FOPI detector is able to measure charged particles from pion to heavy fragments up to Z=15 and it is capable to identify not only resonant but also shortly lived neutral particles with invariant mass reconstruction of their charged decay products [28, 32, 50, 51, 52, 53, 54, 55]. The FOPI detector is shown in figure 2.3.

2.2.1 Plastic Wall

Plastic Wall covers the laboratory polar angle(θ_{Lab}) from 1° to 30° in a full azimuth with 764 plastic scintillators, and it measures the time of flight(TOF) and the mean energy loss(ΔE) of charged particles. Plastic Wall consists of two parts: Outer Plastic Wall(PLAWA) and Zero Degree Detector(ZDD).

Outer Plastic Wall(PLAWA)

The PLAWA covers θ_{Lab} from 7° to 30° and it is made of 512 scintillator strips which are grouped into 8 radial sectors of 64 modules. Each strip has a rectangular cross section of 1.8×2.4 cm^2 and each module is read out by photo multiplier tube on each side. One module provides four signals, which are two energy signals(E_L, E_R) and two time signals(T_L, T_R), and ΔE, TOF, and the position of incidence along the strip(POS) information are derived from four signals by the following relations:

$$\Delta E \propto \sqrt{E_L E_R}, \tag{2.2}$$

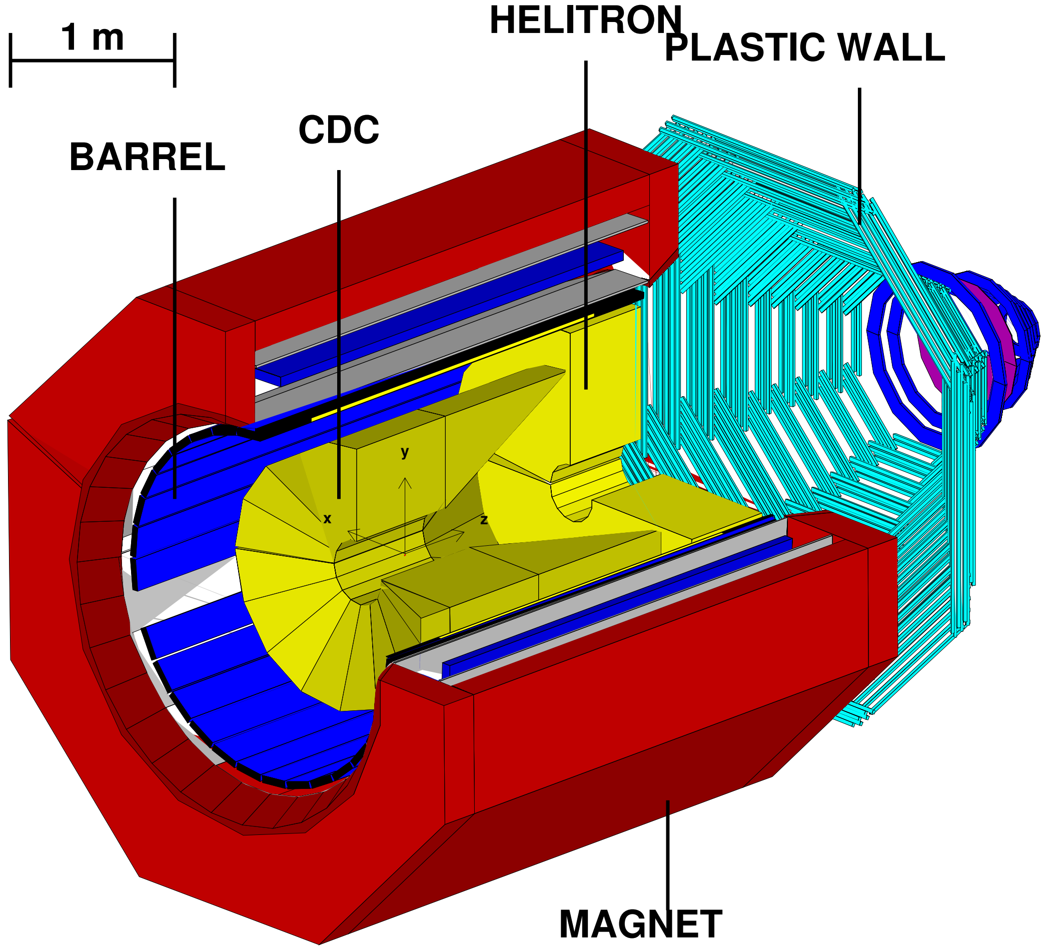

Figure 2.3: FOPI detector with various sub-detector components.

$$\text{TOF} \propto \frac{1}{2}(T_L + T_R), \tag{2.3}$$

$$\text{POS} \propto \frac{1}{2}(T_L - T_R) \quad \text{or} \quad \text{POS} \propto \ln(E_L/E_R). \tag{2.4}$$

The active scintillator lengths are different from 45 cm at θ_{Lab}=7° to 165 cm at θ_{Lab}=30° and TOF resolutions vary between σ=80 and 120 ps which means from σ=1.2 to 2 cm of POS resolutions [49]. From the correlation between ΔE and velocity which can be calculated by using TOF and total flight path of the particle information, one can identify the charge of incident particles. Figure 2.4 is given for the example of charge distributions at the PLAWA, and it shows clear charge distribution up to Z=6 at 0.4A GeV and Z=2 at 1.528A GeV.

The PLAWA gives fast information of the charged particle multiplicity in an event, thus it is suited for the trigger system in which the isospin experiment had three specific event trigger at the hardware levels [49].

- Minimum Bias Trigger: Multiplicity ≥ 1 at the PLAWA
- Medium Bias Trigger: about 50% of the rate of the minimum Bias Trigger
- Central Bias Trigger: about 10% of the rate of the minimum Bias Trigger

Zero Degree Detector(ZDD)

The ZDD is made of 252 trapezoidal shape scintillator paddles which are arranged in seven concentric rings, and it covers θ_{Lab} range between 1° and 7°. The ZDD measures TOF and ΔE, and it delivers the charge and the velocity of incident particles similar to the PLAWA.

2.2.2 Central Drift Chamber(CDC)

The Central Drift Chamber(CDC) is the main tracking system of the FOPI detector and it has a full azimuthal coverage of θ_{Lab} from 33° to 145°. The CDC has a length of 2 m and radial distances between 20 and 80 cm

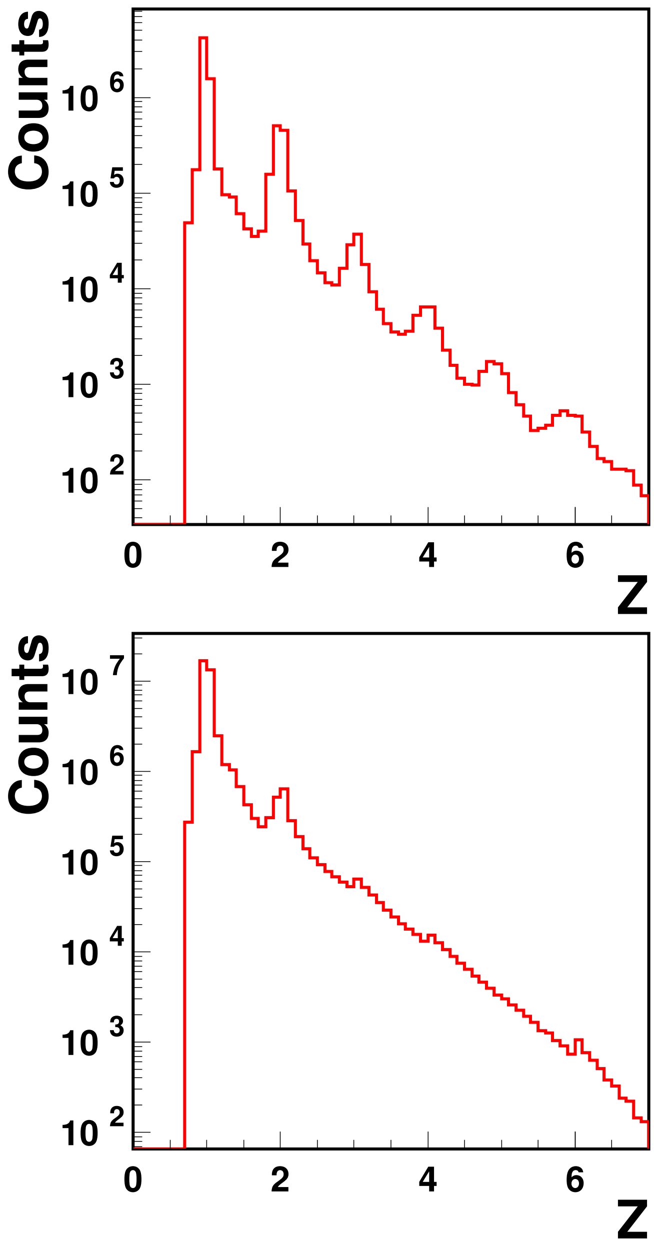

Figure 2.4: Charge distributions at the PLAWA in Ru + Ru collisions at $0.4A$(top) and $1.528A$(bottom) GeV.

from the target position. In the xy plane direction, the CDC is divided into 16 sectors each containing 60 sense wires and 61 potential wires all of which are aligned parallel to the beam axis. The sense wires are 30 μm thick W-Rh(20%) with a resistance of 500 Ω/m. The lengths of the sense wires vary between 86 and 190 cm depending on radial coordinate [50]. The CDC is operated with a mixture of 88% Ar, 10% Isobutane, and 2% CH_4 at a slight overpressure under the applying drift voltage of -15 kV and potential voltage of -1.63 kV. High voltages on the drift and potential wires provide homogeneous and strong electric fields. The ionization electrons, which are produced by charged particles passing through the gas, drift towards the sense wires where the signals are collected. The signals on the sense wires are read out by FlashADCs on both ends, which gives a possibility to reconstruct the position of the hit along the wire via charge division.

The CDC is placed inside of the superconducting solenoidal magnet which produces homogeneous magnetic field of 0.6 T($\pm$1.5% in the central volume) along the beam axis. The paths of charged particles are curved by the magnetic field, thus the CDC is able to measure the momentum and the specific energy loss, which allows for the particle identification of the reaction products by the following formula [56, 57, 58]:

(a.k.a. Bethe-Bloch formula)

$$-\frac{dE}{dx} = 4\pi N_a r_e^2 m_e c^2 \rho \frac{Z}{A}\frac{z^2}{\beta^2}\left[\frac{1}{2}\ln\left(\frac{2m_e\gamma^2 v^2 W_{max}}{I^2}\right) - \beta^2 - \frac{\delta}{2} - \frac{C}{Z}\right] \quad (2.5)$$

N_a: Avogadro's number = 6.022×10^{23} mol^{-1},
r_e: classical electron radius = 2.817 fm,
m_e: electron mass = 0.511 MeV/c^2,
c: the speed of light,
ρ: mass density of medium,
Z, A: charge and atomic mass number of the medium,
z: charge of the incident particle in unit of e,
v: the velocity of the incident particle,
β: v/c,
γ: $1/\sqrt{1-\beta^2}$,
W_{max}: maximum energy transfer in a single collision

$W_{max} = \frac{2m_ec^2\beta^2\gamma^2}{1+2\gamma m_e/M+(m_e/M)^2}$ with the incident particle of mass M

$W_{max} = 2m_ec^2\beta^2\gamma^2$ for $M \gg 2\gamma m_e$,

I: mean excitation energy

$I = 12Z + 7$ eV for $I < 13$ and $I = 9.76Z + 58.8Z^{-0.19}$ eV for $I \geq 13$,

δ: density effect correction,

C: shell effect correction,

$4\pi N_a r_e^2 m_e c^2 = K = 0.3071$ MeVg^{-1}cm^2.

Once particles are identified, its transverse momentum and momentum can be calculated by the following formulae:

$$P_t = e \cdot Z \cdot B \cdot R, \tag{2.6}$$

$$P = P_t / \sin(\theta), \tag{2.7}$$

P_t: transverse momentum of the charged particle (GeV/c),

e: elementary charge $= 0.3$ T^{-1}m^{-1} (GeV/c),

Z: charge number of the charged particle,

B: magnetic field (T),

R: radius of the charged particle track in the xy plane (m),

P: momentum of the charged particle (GeV/c),

θ: polar emission angle of the charged particle.

While the charged particle traverses the gas volume of the detector, it leaves a track of ionization along its trajectory and one can calculate the positions of ionization(hits). However, each hit has a symmetric partner(mirror hit) relative to the sense wire planes because the direction of drift electrons can not be measured. Mirror hits make the mirror track and it gives the ambiguity of finding the real track. In order to have a criterion to distinguish between real and mirror tracks, the sense wire planes are tilted by 8° relative to the radial direction starting from the beam axis. Within this geometry, the mirror tracks do not originate anymore from the target and figure 2.5 demonstrates the effect of the tilting of the sense wire planes. Furthermore, the sense wires within the planes are alternatively staggered by ± 100 μm, which could be also used to reject the mirror tracks.

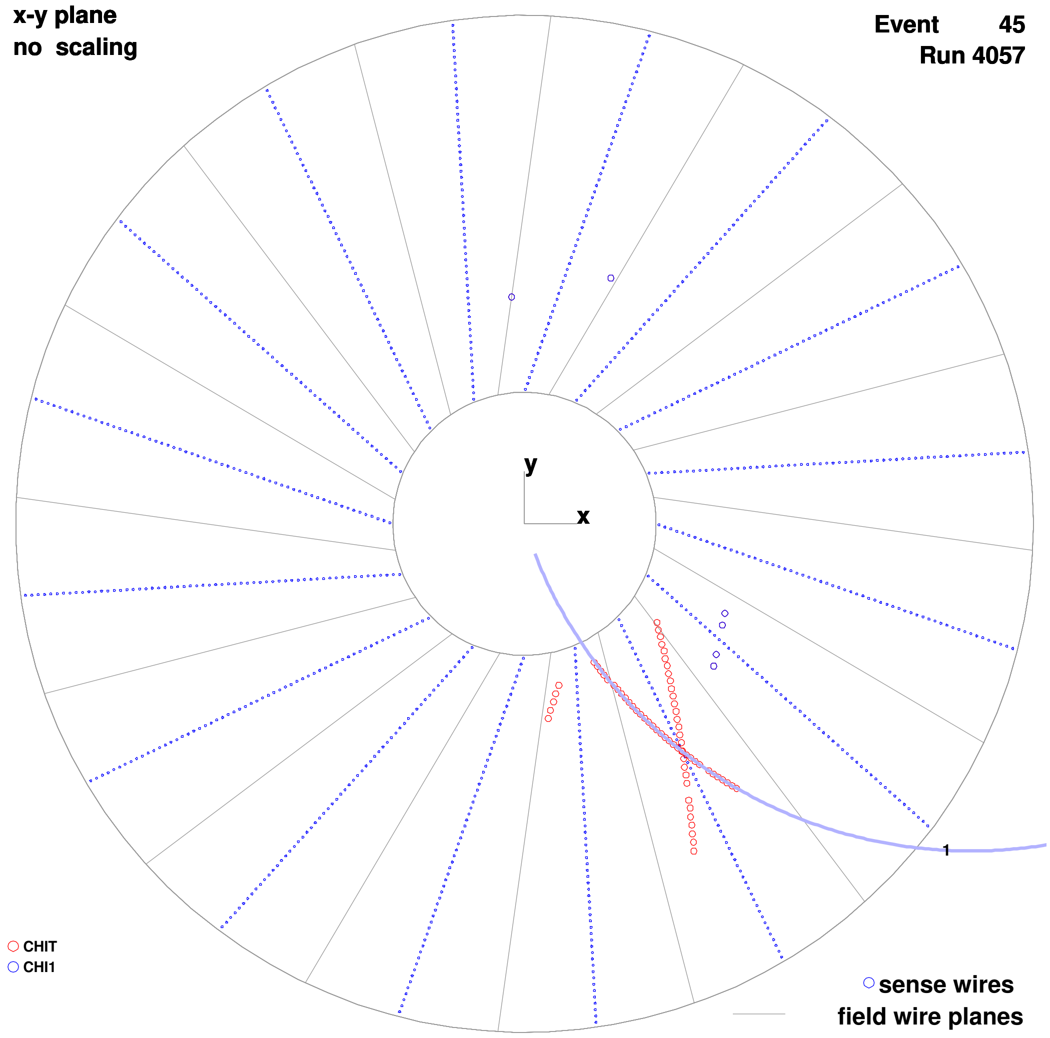

Figure 2.5: View of the CDC in the xy plane. Sectors in the CDC are tilted and dotted lines are the sense wires. Real hits(open circles under thick solid line), reconstructed track(thick solid line with indexing 1) along real hits, and mirror hits(other open circles) are shown.

CDC Calibration and Tracking

In central events of Au + Au collisions, up to 100 particles are emitted in the CDC acceptance. Average hit multiplicity per track is 50, and 5000 hits are recorded on 960 sense wires in a single event [50]. Therefore, it will be challenge to distinguish hit positions from the signals on the sense wires and to reconstruct tracks along the hits by tracking algorithms. FOPI has developed and used several tracking algorithms which can be divided into two categories as local and global methods. Local tracking method starts to look in window of small track density in the xy plane, which is usually the outer circumference of the CDC, and selects three hits which define a circle what passes through the vertex at $(x,y)=(0,0)$. After this step, the search continues by testing whether hits further inside the CDC can be identified as a circle. If there are associated hits within the windows, the circle fit is repeated by including new hits and the search continues until hits at the inner circumference of the CDC are reached. The hits on one circle are identified as the track of the charged particle [59, 60, 61]. In other tracking method, global tracking has to transform the coordinates of hits with certain parameterized form first, and, then it searches for peaks in a histogram(Conformal Mapping) or in one level(Hough transformation) [62, 63]. Detail performance comparison with tracking algorithms can be found in reference [64]. In particular, the local tracking method has been used for the isospin experiment.

In order to reconstruct hit positions in the xy plane, three important global parameters, which are total time-offset, drift velocity, and Lorentz angle, should be determined. The hit positions in the xy plane are measured by the formula:

$$\begin{pmatrix} x_m \\ y_m \end{pmatrix} = \begin{pmatrix} x_w \\ y_w \end{pmatrix} \pm \begin{pmatrix} \cos\alpha_L \\ \sin\alpha_L \end{pmatrix} v_D\,(t - t_w - t_c - t_\circ) \tag{2.8}$$

where x_m, y_m are the measured hit position and x_w, y_w are the sense wire position which is included in the CDC geometry data base for all sense wires, α_L is Lorentz angle, which is defined as the angle between the drift direction of the electron and the electric field, and v_D is drift velocity, which is defined as the velocity of drift electron in the gas due to the electric field. Here, t is the measured time and $t_\circ$ is total time-offset, t_w is wire-wise time-offset, and t_c is crate-wise time-offset. Figure 2.6 shows the effects of using wrong parameters. For wrongly determined total time-offset case, the real trace of the track is divided into two parallel pieces. The trace of the track is broken at the intersection of the cathode plane and it is turned around the trace of the real track for wrongly determined drift velocity case. The trace of the track is, also, broken at the intersection of the cathode plane and the coordinates of hits are rotated with the angle around the position of the sense wires for wrongly determined Lorentz angle case. However, one has to be careful to determine proper values of drift velocity and Lorentz angle, because they are correlated each other. In the isospin experiment, three global parameters are determined for total time-offset $t_\circ$=182 ns, drift velocity v_D=45.3 μm/ns, and Lorentz angle α_L=30°. Each of these values is the mean value of fit results with Gaussian function on each plot shown in figure 2.7.

For the reconstruction of hit positions at the z coordinate, one has to deal with the charge division and it is well known method to measure the coordinates along the sense wire in wire chambers. When an avalanche occurs on a resistive sense wire of the length L at a distance $x < L/2$ from the right end side, then the left end side is at L-x, and the signal sees less resistance towards the right than to the left. Therefore, a higher signal will arrive on the right end side and the signal ratio is given by Q_L/Q_R=$x/(L-x)$. Figure 2.8 is given for the schematic plot of the z-calibration of the CDC. For the CDC case, we use the following formulae which include some corrections.

$$\frac{Q_R^c}{Q_L} = \frac{R_L}{R_R} = \frac{l_w^{eff}/2 + (z - z_w)}{l_w^{eff}/2 - (z - z_w)} \tag{2.9}$$

$$z = z_w + \frac{l_w^{eff}}{2} \cdot \frac{Q_R^c - Q_L}{Q_R^c + Q_L} \tag{2.10}$$

z is the measured hit position in the z-axis and z_w is the position of the middle of the sense wire from the target(z=0). Q_R^c is the corrected charge signal at the right end side and l_w^{eff} is the effective wire length. They are defined as following:

$$Q_R^c = \frac{Q_R}{1 - C_{reduc}^0 - (60 - n_w) \cdot C_{reduc}^1/60}, \tag{2.11}$$

$$l_w^{eff} = l_\circ \cdot (1 + 2R_\circ/R_w)\,, \tag{2.12}$$

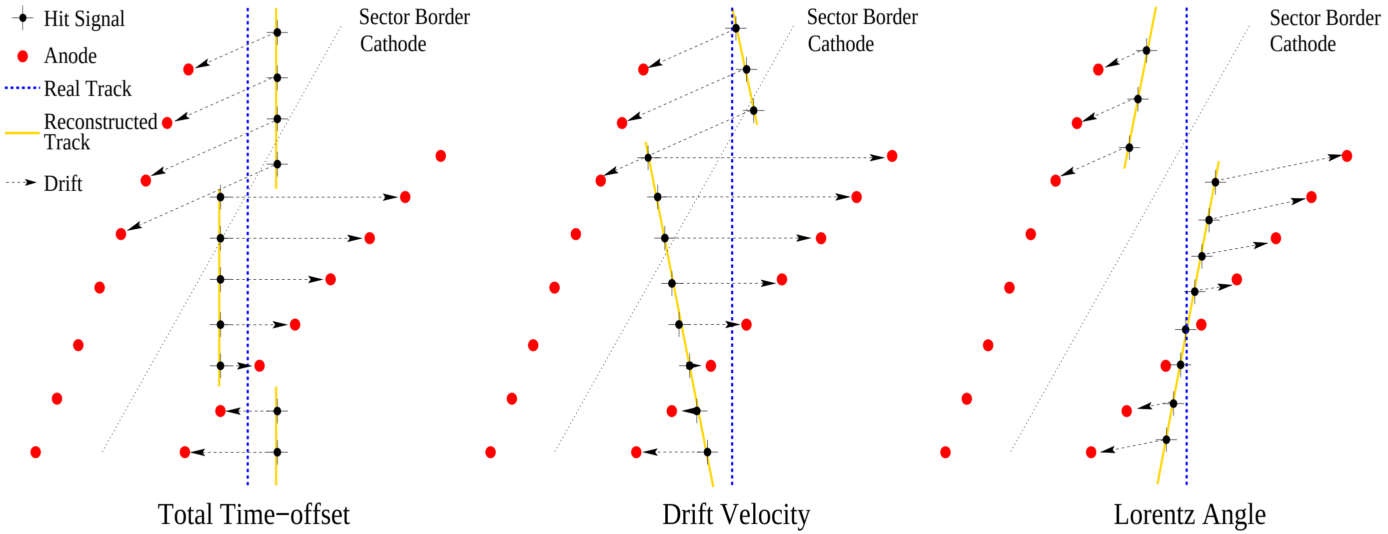

Figure 2.6: Examples of using wrong three global parameters: total time-offset(left), drift velocity(middle), and Lorentz angle(right). In all cases shown are the broken trace of the track.

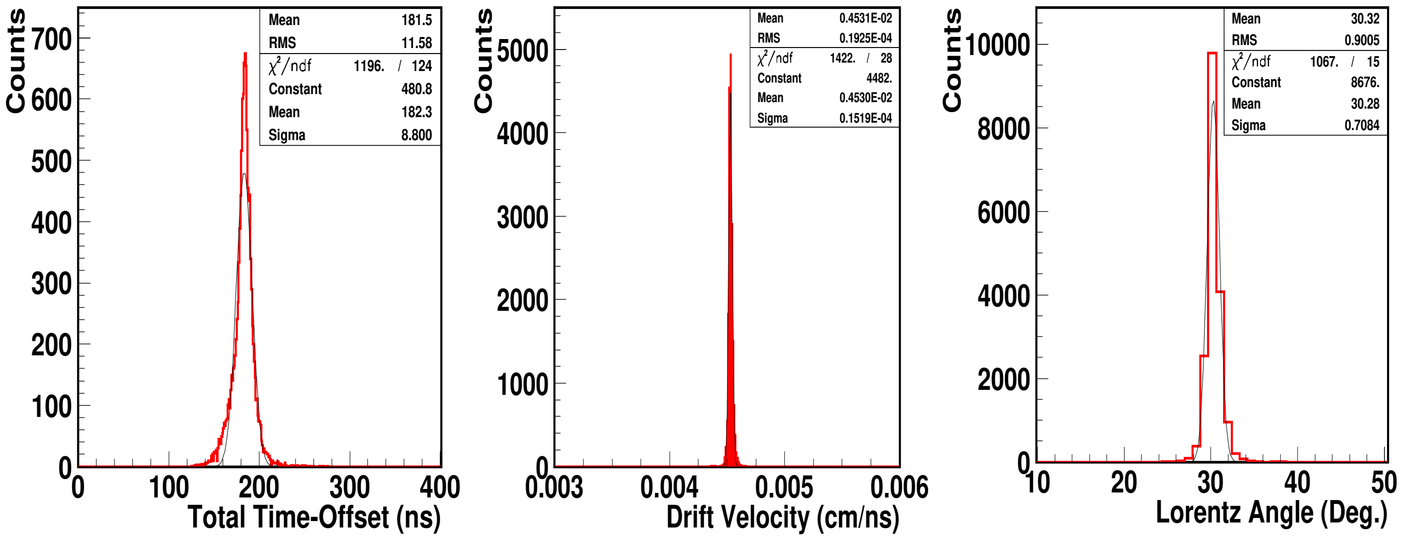

Figure 2.7: Estimated global parameters for the CDC calibration: total time-offset(left), drift velocity(middle), and Lorentz angle(right). The fit results with Gaussian function on each plot are shown.

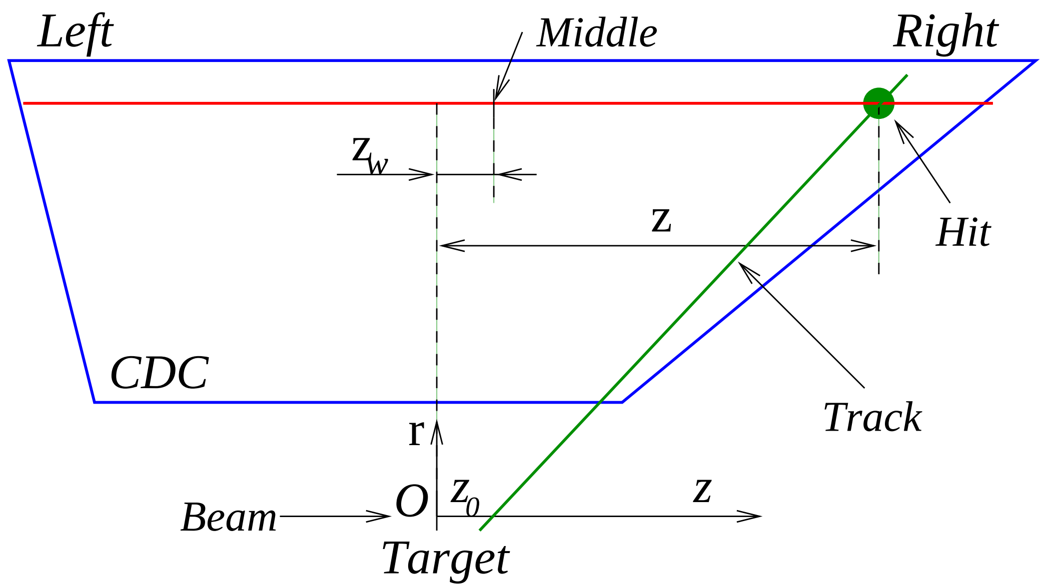

Figure 2.8: Schematic plot of the z-calibration in the rz plane: See the text for the details.

where n_w is the number of each sense wire from inside cylinder, and $l_\circ$ and R_w are the length and the resistance of individual sense wire, respectively. $R_\circ$ is the resistance of preamplifier at the end of the wire. z_w and $l_\circ$ are already included in the CDC geometry data base, and R_w is simply calculated with using the value of $l_\circ$ and the resistance of the wire(500 Ω/m). For the z-calibration, two cable reduction factors(C^0_{reduc}, C^1_{reduc}) are variables and criteria of the z-calibration are θ_{Lab} distribution, in which the lower limit of the distribution should be $\sim$30°, the front peak of the distribution should be $\sim$33°, and one can see the target deep at θ_{Lab}=90°, and the position signal from the Plastic Barrel strip along the z-axis, in which the limit should be $\sim$135 cm from the target position.

After the reconstruction of hits, position resolutions of hits are estimated at $\sigma$$\sim$300 μm in the xy plane and $\sigma$$\sim$10 cm in the z-axis. With the presence of the measured hit positions, the tracking algorithm, which is the local tracking method for the isospin experiment, reconstructs the charged particle tracks of the path followed the hits by using the circle fit in the xy

plane and the straight line fit in the rz plane. Figure 2.9 is an example of the reconstruction of the tracks in the rz plane.

The primary vertex is the position of the interaction point between nucleus in beam and nucleus in target, thus it should be very close to the origin of the coordinates. For the determination of the primary vertex, one has to integrate over the projected points of all tracks in the CDC in an event. It is possible to have some difference between the primary vertex projected by the reconstructed tracks and real vertex. The distance between the primary vertex and each track is defined as *d0* in the xy plane and *z0* in the z-axis. In figure 2.8, *z0* is demonstrated in the distance between the origin of the coordinates and the crossing point on the z-axis of the track. In figure 2.9, however, one can see that the position of the primary vertex in the z-axis is shifted to downstream side(positive z coordinates direction). It is due to the position resolution along the z-axis, and this can drive the distorted polar angle information of the particle. Therefore, one can correct it with the tracks originating from the target position in the z-axis. The correction is called the refitting procedure of the track reconstruction and it brings the position of the primary vertex in the z-axis to the origin of the coordinates. The effect of the refitting of the tracks is depicted in figure 2.10. More details about the primary vertex and *d0*, *z0* distributions of tracks will be discussed in chapter 3.

Particle identification in the CDC relies on the Bethe-Bloch formula given in equation 2.5. It uses the statistical distribution of the truncated mean energy loss(dE/dx) and the rigidity(P/Z) of charged particles. From the correlation between $\log(dE/dx)$ and P/Z of particles, mass distribution of particles is obtained by using the parameterized Bethe-Bloch formula:

$$\mid dE/dx \mid = par1 \cdot \left[c_1 \cdot \frac{Z^{par5}}{\beta^2} \cdot \left[\ln \left(par4 + c_2 \cdot (\beta\gamma)^{2 \cdot par2} \right) - \beta^{2 \cdot Z^2} \right] \right]. \quad (2.13)$$

Here,

$$\beta^2 = \frac{(P \cdot Z)^2}{(P \cdot Z)^2 + (m/par3)^2}, \quad (2.14)$$

where m, Z, P are the mass, the charge, and the momentum of the charged particle, respectively, and c_1=KZ/A, c_2=$2m_e$/I are constants. *par1*, *par2*, ..., and *par5* are free fitting parameters for the mass reconstruction. These

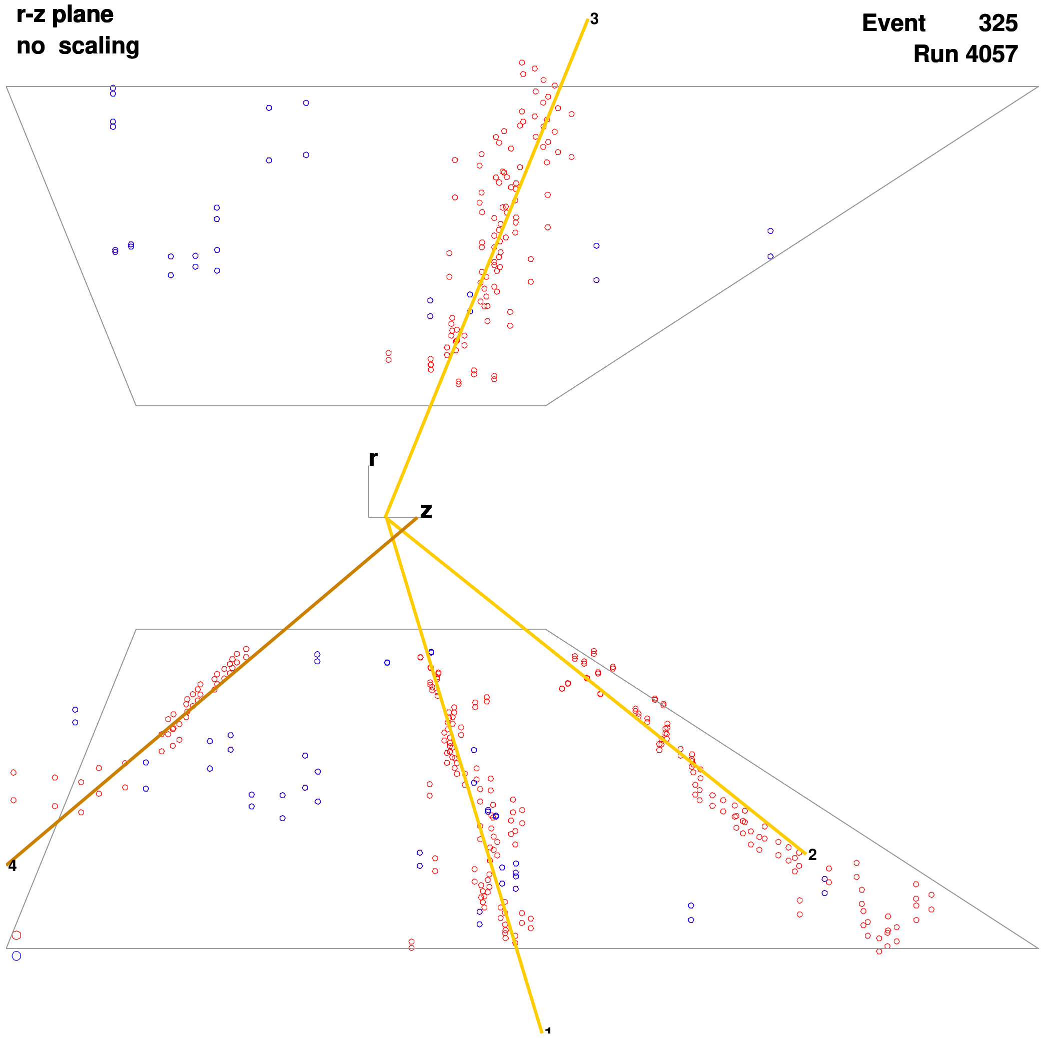

Figure 2.9: View of the CDC in the rz plane: All hit(real+mirror) positions along the z-axis and the reconstructed tracks with lines are shown.

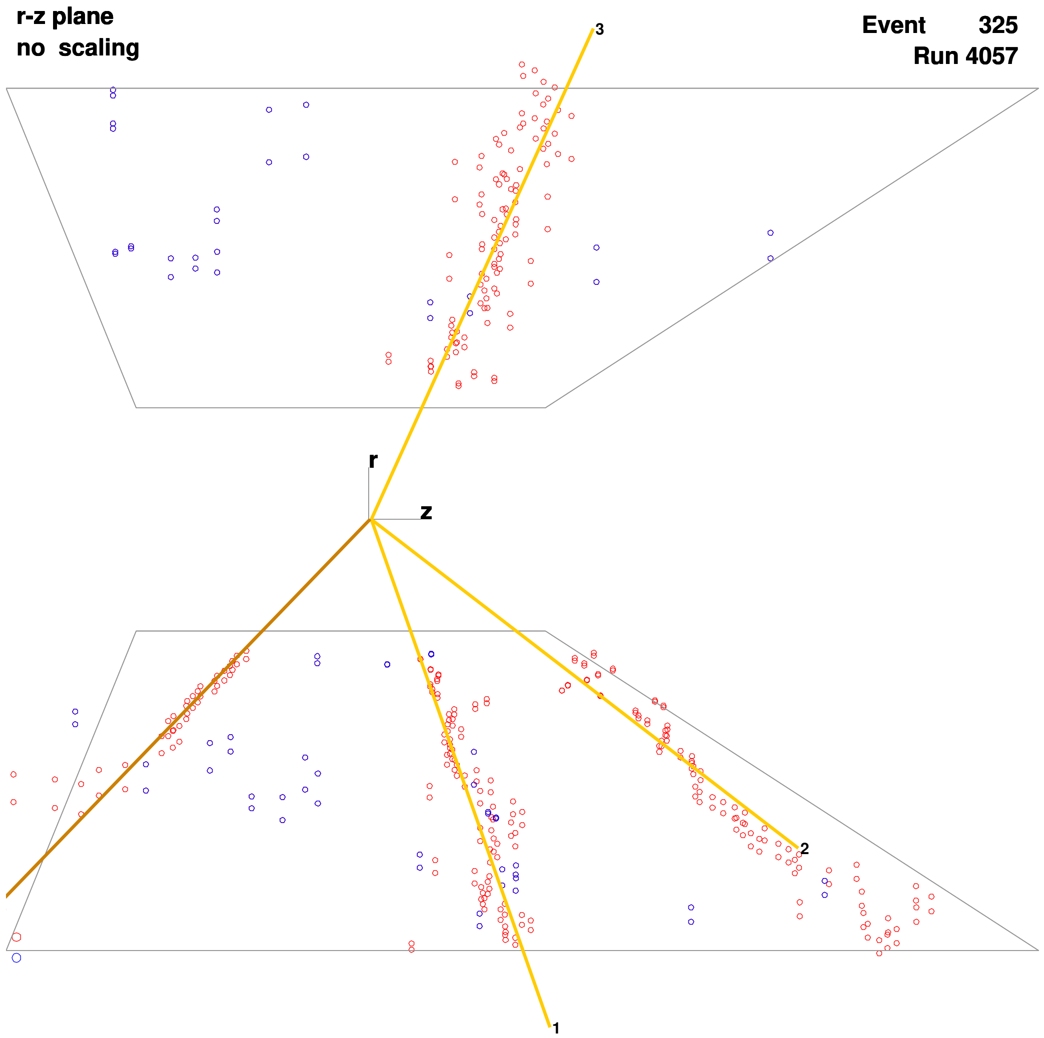

Figure 2.10: The same as figure 2.9, but the reconstructed and refitted tracks with lines are shown.

parameters should be estimated and adjusted during the CDC calibration. The correlation between $\log(dE/dx)$ and P/Z in the CDC is shown in figure 2.11 and the energy loss resolution ($\sigma(dE/dx)/(dE/dx)$) as a function of dE/dx in the CDC is estimated between 15 and 25%. The transverse momentum resolution ($\sigma(P_t)/P_t$) is determined by simulations with the IQMD as an event generator and the GEANT package [65], and it rises from 4% for $P_t < 0.5$ GeV/c to about 12% for P_t=2 GeV/c [50]. Figure 2.12 shows the reconstructed tracks in an event and various lines represent different particle species by the particle identification.

2.2.3 Plastic Barrel

Plastic Barrel is surrounding the CDC and it consists of 180 individual plastic scintillator strips placed inside the magnet. Plastic Barrel covers around 85% of the full azimuth in θ_{Lab} from 39° to 130°. Each strip has a rectangular cross section of 4×3 cm^2 with the length of 240 cm, and the distance from the target of 111 cm. All strips are running parallel to the beam axis. The signals on the strip are read out by photo multiplier tube on each side and they provide TOF and POS information. Plastic Barrel has the TOF resolution of σ∼300 ps and the POS resolution of σ∼8 cm.

Plastic Barrel has been used by the geometrical matching between the tracks at the CDC and the hits at the Plastic Barrel strips. With certain matching conditions, the charge and the TOF information from the Plastic Barrel allow to improve the particle identification with information provided by the CDC. For example, one can identify charged kaons by using the correlation between momentum information from the CDC and velocity information from the Plastic Barrel.

2.2.4 Helitron

Helitron is the forward drift chamber and it has been used for the tracking of charged particles. Helitron is able to separate isotopes in the forward directions to the elements identified by the PLAWA within θ_{Lab} from 7° to 30°. The inner cylinder structure is held by the cathode frames which are

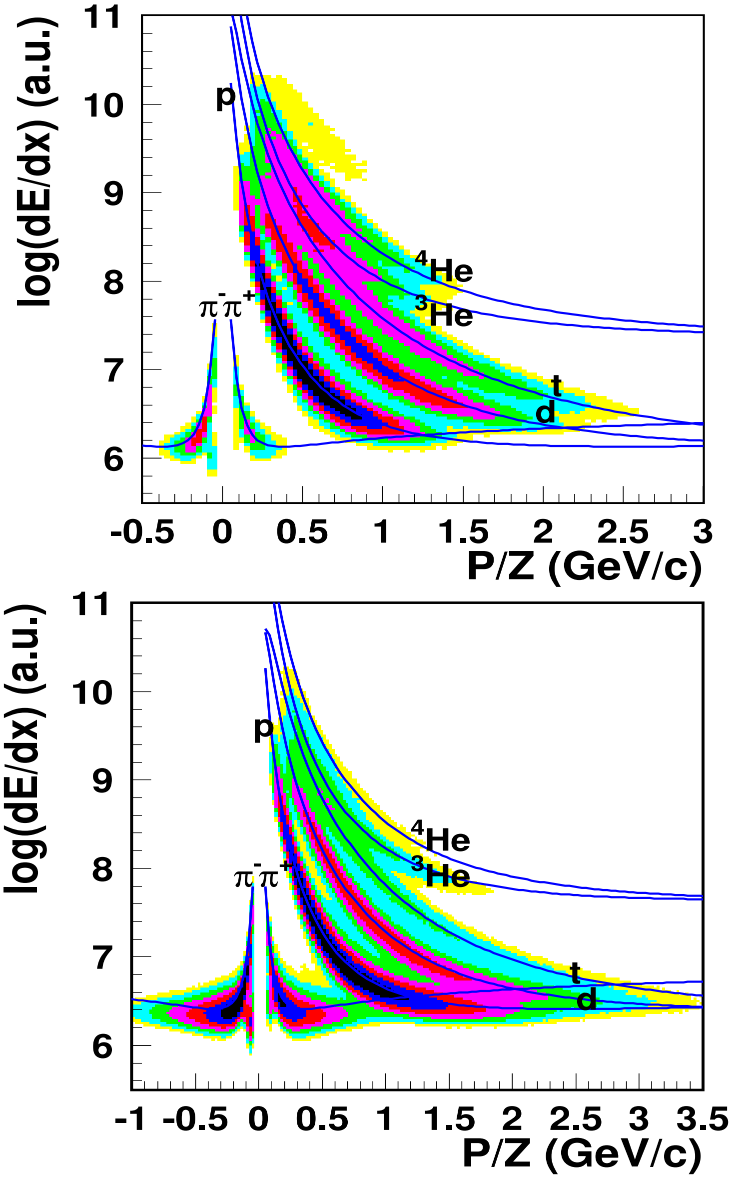

Figure 2.11: Correlation between $\log(dE/dx)$ and P/Z in the CDC: lines are the parameterized energy loss in a given momentum with the nominal particle mass for each particle species. These figures are for Ru + Ru collisions at $0.4A$(top) and $1.528A$(bottom) GeV.

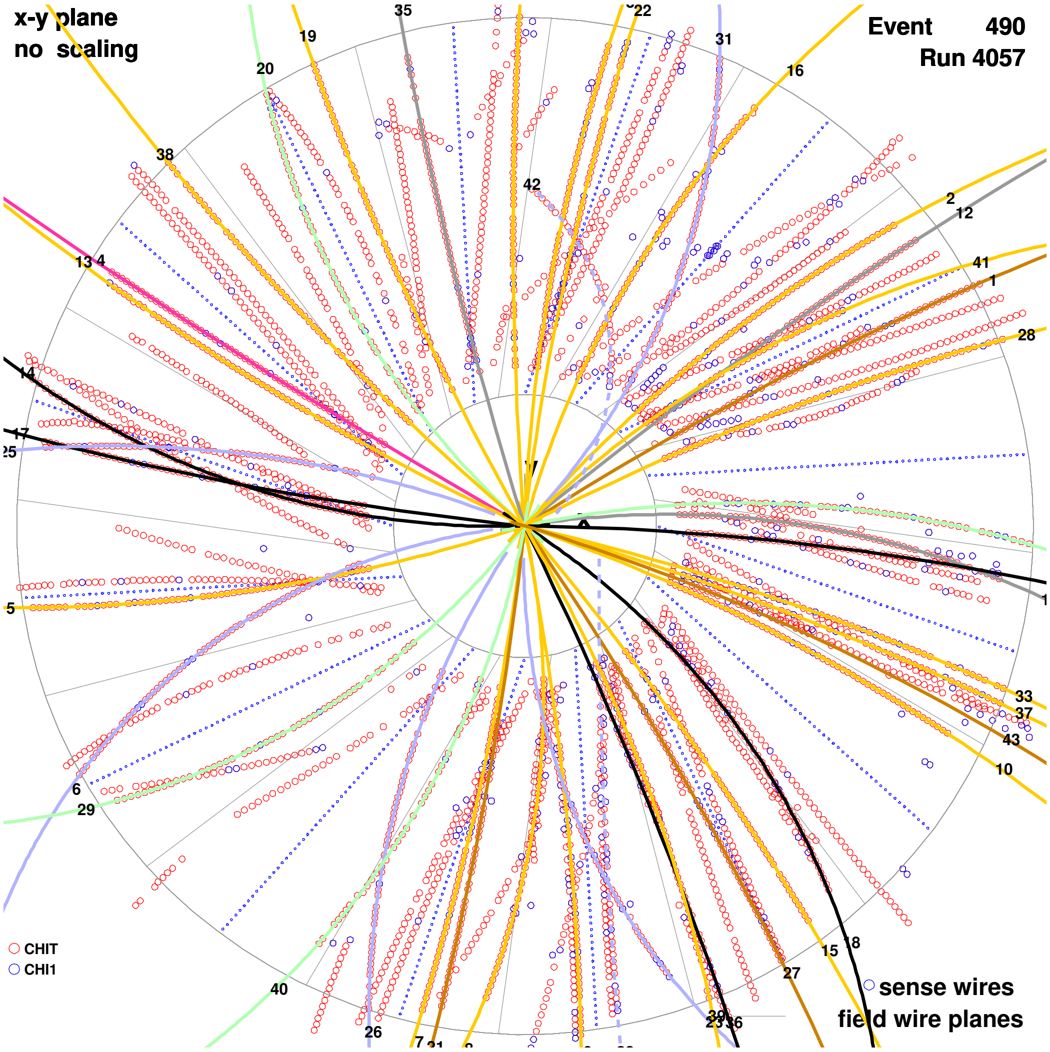

Figure 2.12: Particle tracks in an event at the CDC: the figure is the view in the xy plane and it is from Ru + Ru collisions at 1.528A GeV. All hit(real+mirror) positions are displayed. The curvatures of positive(negative) particles are clockwise(counterclockwise). The reconstructed tracks are represented with different lines by the particle identification.

fastened radially like a bicycle wheel. Helitron is subdivided into 24 sectors each containing 54 sense wires and 53 potential wires all of which are perpendicular to the beam axis. The potential wires are made of 125 μm diameter CuBe, and the sense wires are 50 μm diameter NiCr with 1 kΩ/m resistivity [50]. Helitron is operated with the same gas mixture as the CDC, and the tracking method and the reconstruction of the particle mass are similar to those of the CDC [54, 61, 66]. As same as the relation between the CDC and the Plastic Barrel, one can use the correlation between momentum information from Helitron and velocity information from the PLAWA for the particle identification. The correlation between momentum and velocity is shown in figure 2.13.

2.2.5 Beam Counter System

Beam counter system consists of three components. Halo 1, and start counter are located inside the vacuum beam pipe, and Halo 2 is placed in front of the target. Halo 1 is the veto counter to define the position and the spot size of the beam. Start counter is made of two plastic scintillator foils of 280 μm thickness each and the signals are read out by photo multiplier tube. Start counter is installed at the downstream side from Halo 1 counter, and it has been used for counting the number of nuclei in the beam and for providing the reference time signal to sub-detector components. The time resolution of start counter is around 50 ps. Halo 2 is the additional veto counter and it is placed at the upstream side of the target. Halo 2 has small opening window in the middle of the counter and it provides the on-line information of beam focusing by the anticoincidence technique with Halo 1. Figure 2.14 is the schematic view of the beam counter system.

2.2.6 Detector Acceptance

Table 2.2 summarizes the detector acceptance of each sub-detector. Figure 2.15 illustrates the detector acceptance in the phase-space of Z=1 baryons with different impact parameter ranges in the IQMD simulation of Ru + Ru collisions at 0.4A GeV. For the most central collisions, produced particles are mainly populated in the mid-rapidity region, and target and

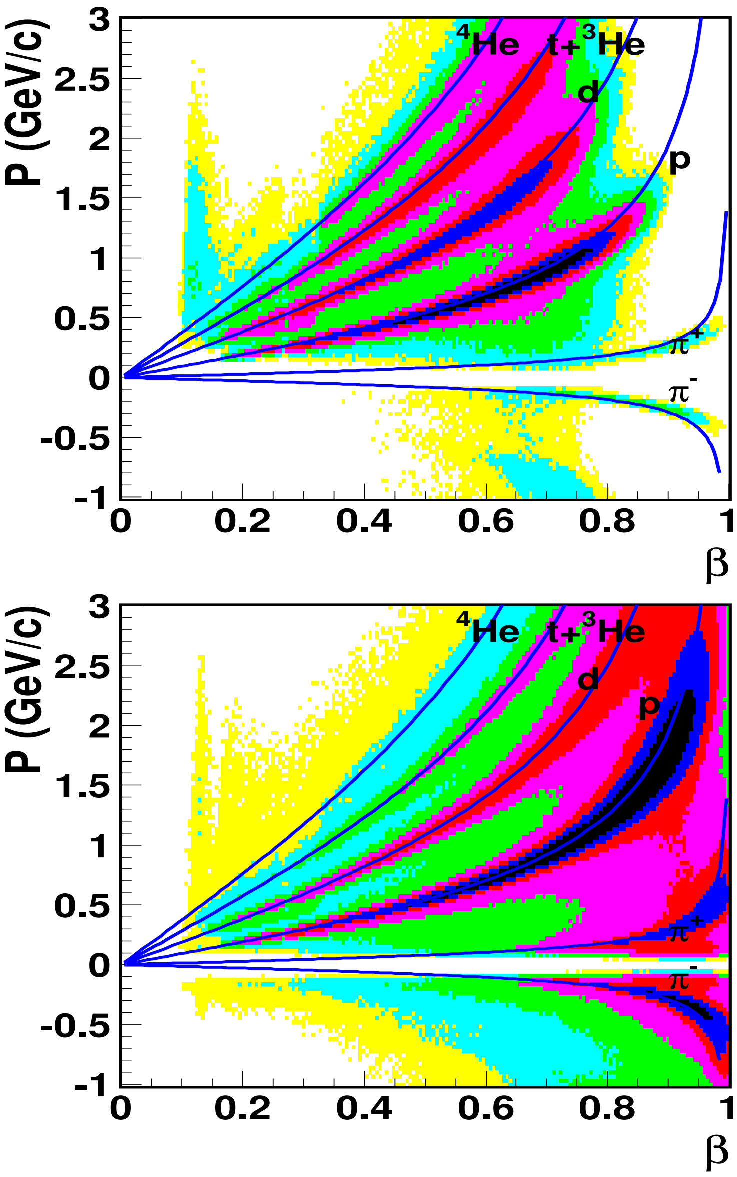

Figure 2.13: Correlation between the momentum from Helitron and the velocity from the PLAWA: lines are the expected momentum in a given velocity with the nominal particle mass for each particle species. These figures are for Ru + Ru collisions at $0.4A$(top) and $1.528A$(bottom) GeV.

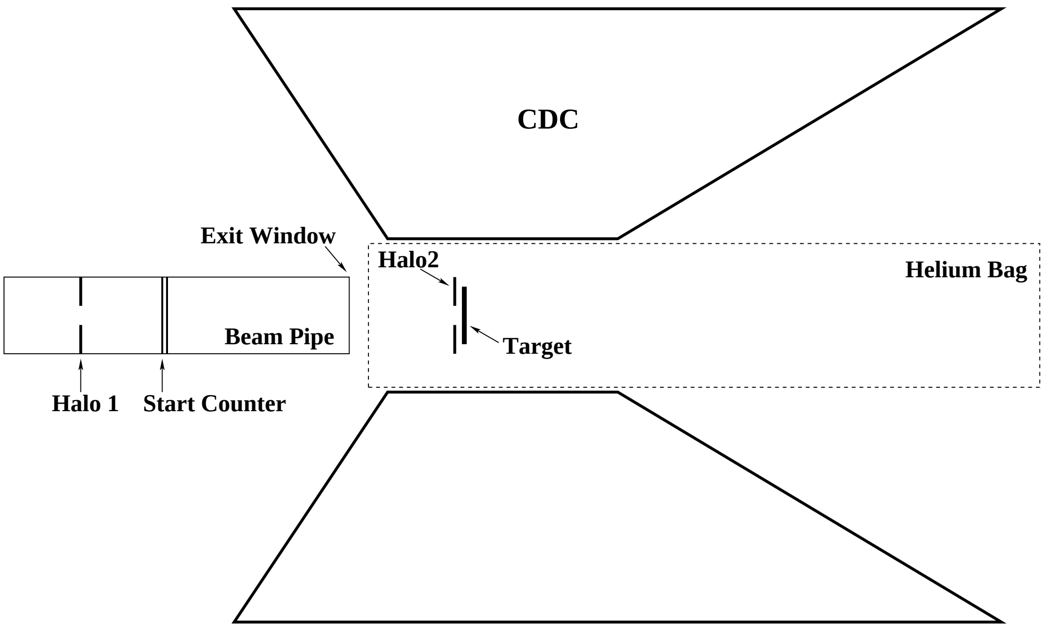

Figure 2.14: Schematic view of the beam counter system.

projectile components are not distinguishable. Components of the target and the projectile are separated in the mid-central collisions and there is clear breakup of target and projectile in the peripheral collisions. Figure 2.16 is the detail drawing of the experimental setup in 1996.

Detector	Acceptance (θ_{Lab})	Type
Zero Degree	1° - 7°	Plastic Scintillator
Outer Plastic Wall	7° - 30°	Plastic Scintillator
Helitron	7° - 30°	Drift Chamber
Central Drift Chamber	33° - 145°	Drift Chamber
Plastic Barrel	39° - 130°	Plastic Scintillator

Table 2.2: Summary of the acceptance for each sub-component of FOPI detector.

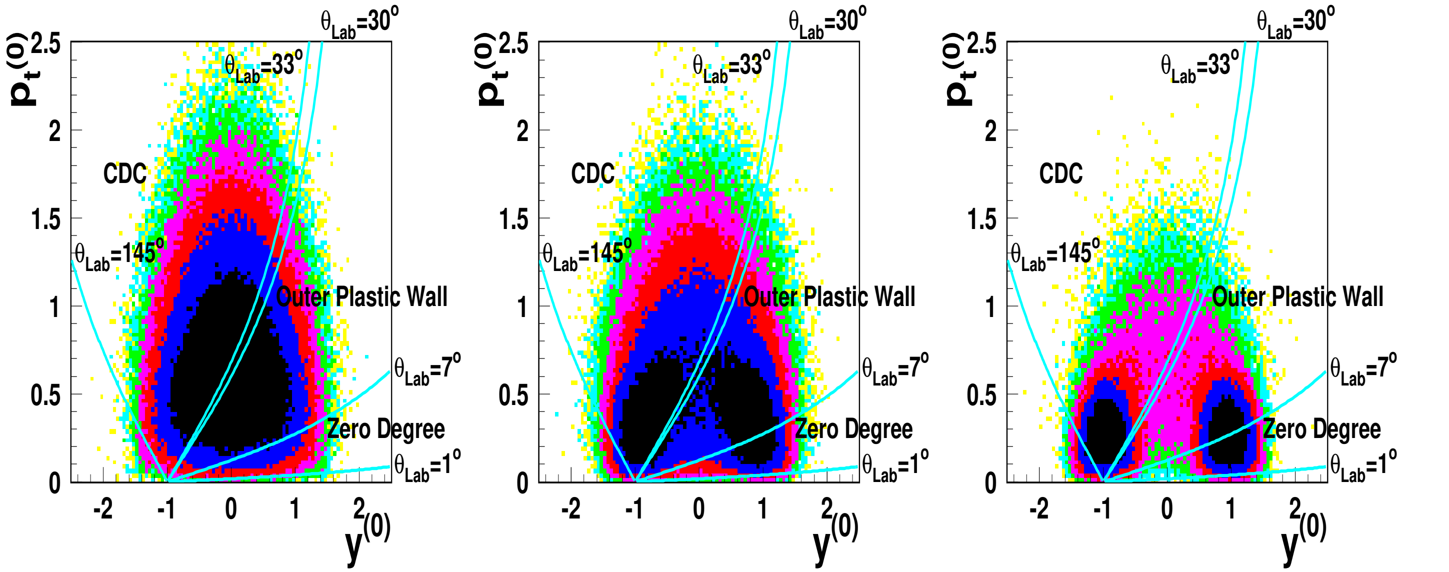

Figure 2.15: Illustration of the detector acceptance in the phase-space. These plots are the full 4π phase-space of Z=1 baryons from the IQMD simulation of Ru + Ru collisions at 0.4A GeV. Different impact parameter ranges are chosen for 0 - 2 fm(left), 4 - 6 fm(middle), and 8 - 10 fm(right).

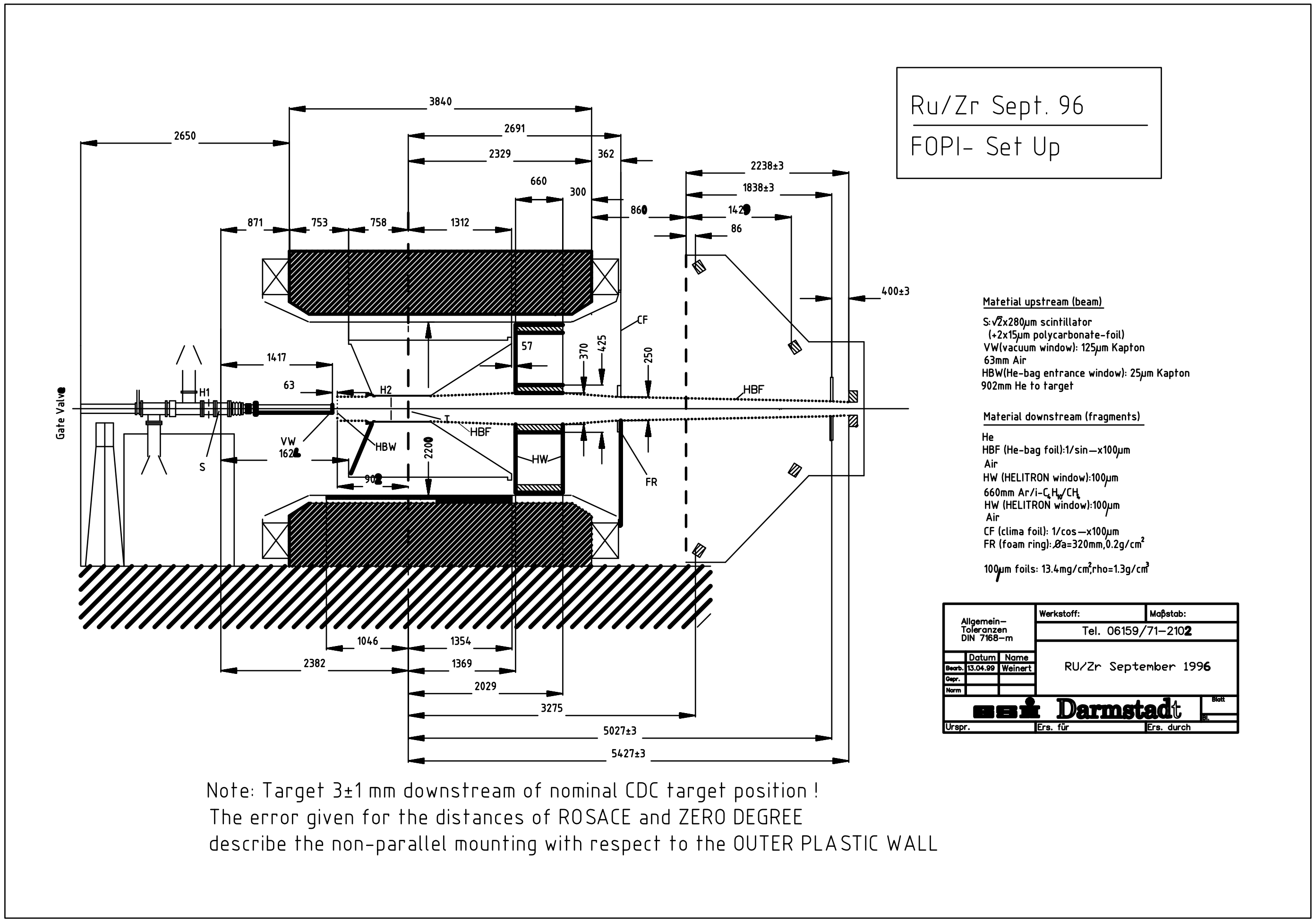

Figure 2.16: Complete FOPI experimental setup in 1996.

Chapter 3

Analysis

In this chapter, the data analysis procedure is discussed in detail. It includes the event selection and the particle identification in the CDC and Helitron in addition to the detector efficiency correction.

3.1 Event Selection

For the data analysis, one has to remove undesired events and select specific event class. In the following sections, the techniques for the rejection of background events and for the selection of the centrality are discussed.

3.1.1 Double Event

In a given event, all of the signals on the sub-detector systems have to be digitalized by electronics, and the digitalized signals are combined by software and they are stored on the storage devices. However, each detector has a different response time and two drift chambers in the FOPI detector system are the slowest. For instance, the CDC has 45 μm/ns drift velocity of ionized electrons and the maximum drift time of electrons in the CDC is around 5 μs. It means that, if the event is accepted by the trigger condition, all of the hit information in the CDC is collected on the sense wires in 5 μs.

Therefore, it is important to be sure that there is no reaction event before and after the given event within the 5 μs time period. If this is not the case, the CDC is not able to resolve between two events, and the events are mixed. This special case is called as "double event". The average time interval between two incoming ion beams is in the order of 20 μs, and the reaction probability between ions in beam and nuclei in target is about 1%. In this condition, the average reaction time between two events is around 2 ms, thus the double events are very rare. The most of the double events are rejected by the trigger system which is based on the much faster PLAWA signals, but some case, which is caused by two ions coming into 100 ns time interval one after the other, is still remained. For the rejection of this specific double event, one can use the start counter information which are arrival time and deposited energy of the beam in two thin plastic scintillator foils, as the start counter has 100 ns time interval of QDC gate. The deposited energy is expected to be higher for the specific double events than normal events. In figure 3.1, the deposited energy and the arrival time distributions at the start counter are shown. The deposited energy distribution has double peak structure and the specific double events are registered in the second peak at the higher QDC channel. Therefore, the double events can be rejected by taking only the first peak. In addition, the arrival-time distribution has a sharp peak structure and the events below and above the peak are rejected as the arrival times are not reasonable.

3.1.2 Vertex

During the experiment, in addition to the real events, there also exist background events, which originate from the interaction of the beam with materials at the upstream side of the target. One can not avoid background events because beam can interact with beam pipe, exit window material of vacuum beam pipe, and air molecules, etc. Part of the background events is rejected by the halo detectors and the trigger system, but many of them are still accepted as real events by the trigger system. In order to reduce the contribution of the background events, one applies cut to the reconstructed primary vertex distributions. The beam spot can move some mm(s) in the xy plane by beam focusing during the experiment. As a result, the primary

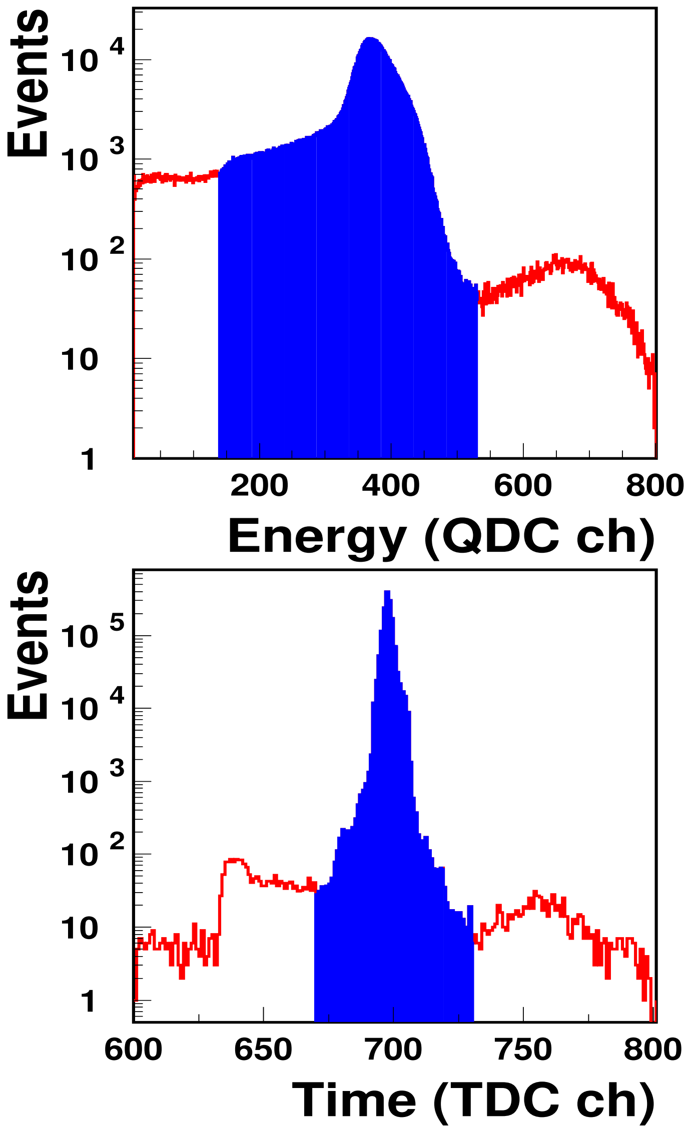

Figure 3.1: Energy(top) and time(bottom) distributions from the start counter. Data are for in Ru + Ru collisions at 1.528A GeV. Energy distribution has double peak structure and the double events cause the second peak at higher QDC channels. Time distribution shows sharp single peak structure. The events in dark shaded areas are chosen for the analysis.

vertex positions in the xy plane deviate a small distance from the origin of the coordinates. The target has the thickness on the order of 100 μm and the primary vertex position in the z-axis should be close to zero. Figure 3.2 shows the primary vertex position distributions in Ru + Ru collisions at 1.528A GeV. The most of the primary vertex positions in the xy plane are populated around 0 with very small deviation. However, the primary vertex position distribution in the z-axis shows very broad and several structures. The broad shape of the distribution shows that the interaction of beam with other materials(not with target) can happen along the whole z-direction, but the dominant peak in the distribution is from the real interactions.

When the primary vertex position along the z-axis is reconstructed, the vertex position of the inside region between z=-20 and 20 cm is chosen for forcing the vertex to be fixed at the target position, but the events with the vertex position outside of this region are left as it is for the analysis of weak decaying particles. The right plot of the z-vertex distribution in figure 3.2 is a close look between z=-20 to 20 cm, and it shows that the primary vertex position in the z-axis is fixed at the target position. The shaded region of each vertex distribution is selected for the following analysis: $|V_x| < 1$ cm, $|V_y| < 1$ cm, and V_z=0. The vertex cuts on x and y distributions reject about 1% of total events. For the z-vertex cut, about 9% of the total events are rejected and if we consider only limited $|V_z|$ values less than 20 cm, less than 1% are rejected. In the end, ~9% of the total events are eliminated as the background events by the vertex cuts in this analysis.

3.1.3 Oxygen Contamination

Oxygen contamination is due to the interaction between ions in the beam and oxygen nuclei in ZrO_2 target. For the rejection of such events, one can use the charged particle multiplicity distributions. The particle multiplicity by the Plastic Wall is dominated by the charged particles at forward hemisphere and the particle multiplicity at the CDC is dominated by the charged particles at backward hemisphere. Total charge from the reaction between Ru on Zr and Zr on Ru should be similar in full phase-space. Therefore, one can expect different charged particle multiplicity distributions from the reactions between pure Zr and $Zr0_2$ targets. Upper plots in figure 3.3

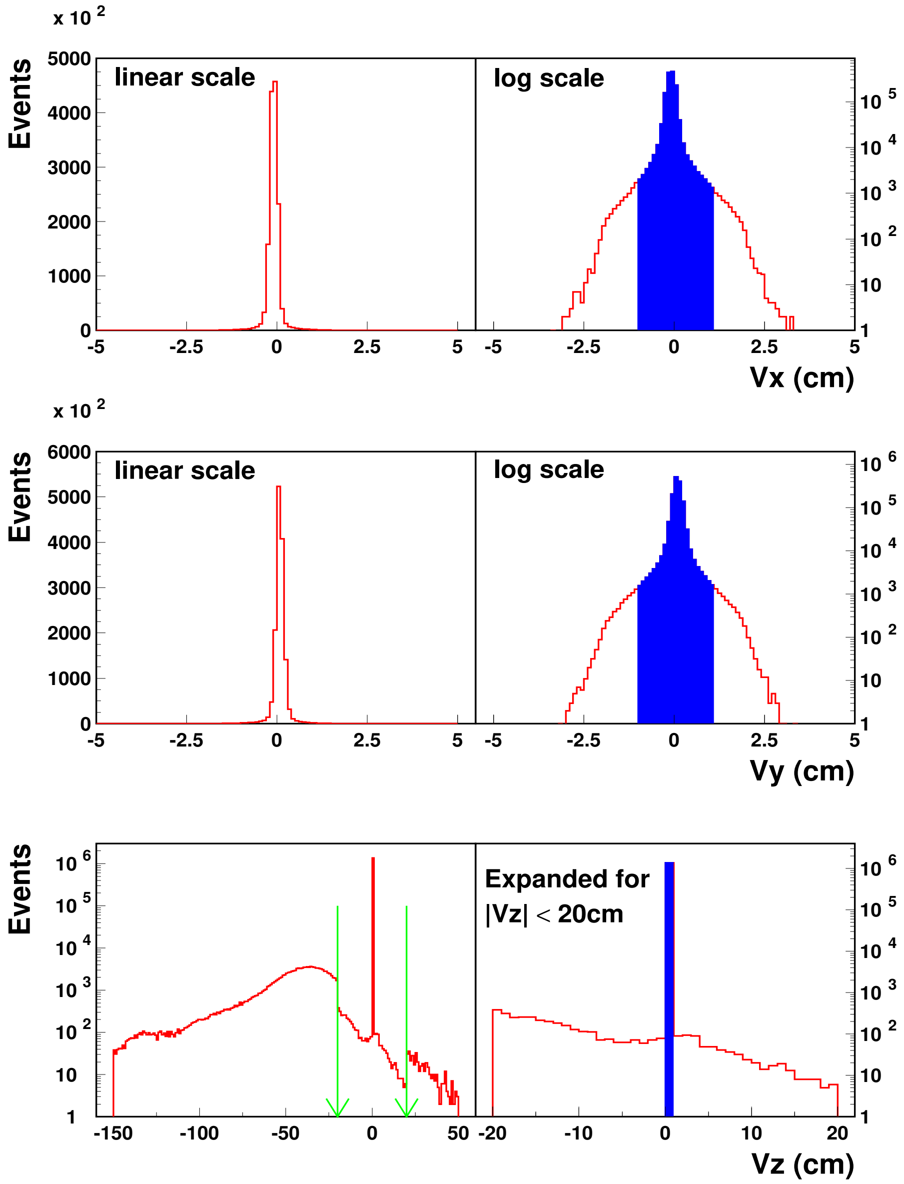

Figure 3.2: Primary vertex position distributions in Ru + Ru collisions at 1.528A GeV: vertex in x (V_x), in y (V_y), and in z (V_z) direction from top to bottom. The shaded areas are taken for this analysis. Detailed explanations are in the text.

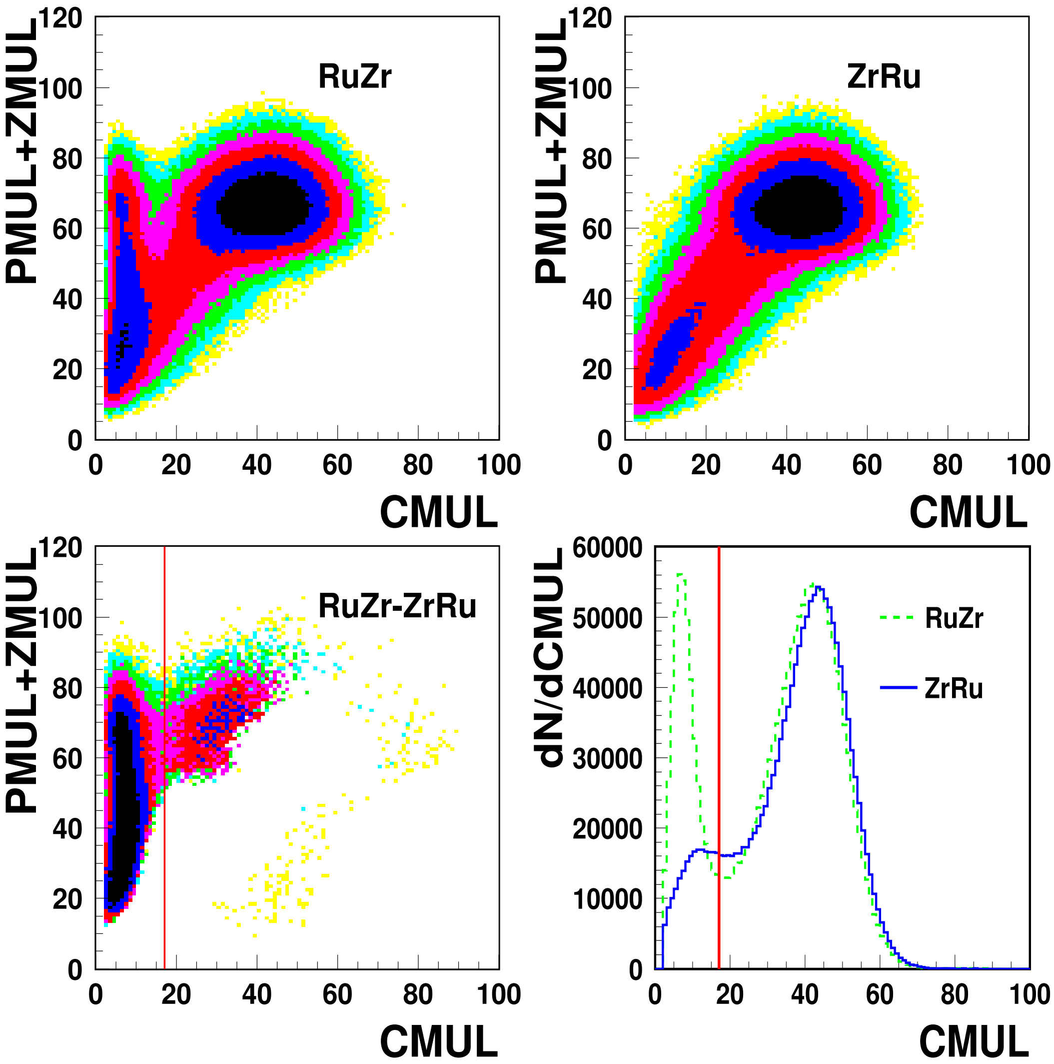

Figure 3.3: Oxygen contamination at 1.528A GeV: Correlation between the Plastic Wall(PMUL+ZMUL) and the CDC multiplicities(CMUL) in Ru + ZrO_2(upper left) and Zr + Ru(upper right) collisions. (Lower left) Background events by oxygen content in ZrO_2 target is clearly shown by the subtraction of the upper two plots. (Lower right) The CDC multiplicity in Ru + ZrO_2(Zr + Ru) collisions is plotted with the dashed(solid) line. The CDC multiplicity values above the vertical solid line are taken for this analysis.

show the correlation between the Plastic Wall(PMUL+ZMUL) and the CDC multiplicities(CMUL) in Ru + ZrO_2(left plot) and Zr + Ru(right plot) collisions. For Zr + Ru collisions in upper right plot shows clear correlation between both multiplicities. In contrast, there is additional structure in the correlation at Ru + ZrO_2 collisions in low CMUL region. It shows that the background events by the oxygen content of ZrO_2 target cause wide variation in the Plastic Wall multiplicity but very limited variation in the CDC multiplicity. Lower left plot in figure 3.3 is the subtraction of upper two plots and shows the main contaminated events are localized in the low CDC multiplicity region in the correlation. Lower right plot in figure 3.3 also shows that Ru + ZrO_2 collisions have abnormally huge peak at low CDC multiplicity than Zr + Ru collisions. For the analysis at $1.528A$ GeV, CDC multiplicities higher than 17 are applied to the ZrO_2 target data in order to reject the oxygen contamination. Although Ru target experiments do not have such a contamination, the cut on the CDC multiplicity is also applied because this cut can influence on the centrality selection. However, according to F. Rami *et al.* [67], the effect of the oxygen contamination is negligible for the physics results at $0.4A$ GeV so that we omit this cut for the analysis at lower beam energy.

3.1.4 Centrality Selection

In order to select the collision centrality of events, FOPI uses several criteria, and two of them will be discussed in this thesis. One is the total charged particle multiplicity, and another is the ratio of the total transverse to longitudinal kinetic energies at the center-of-mass system.

Total Multiplicity

The charged particle multiplicity is based on the idea that more charged particles are produced in more central collisions. It means that high charged particle multiplicity is associated with the event with small impact parameter and vice versa. The total charged particle multiplicity(TMUL) is defined by the sum of multiplicities from the CDC(CMUL) and the Plastic Wall(PMUL+ZMUL):

$$\mathrm{TMUL} = \mathrm{CMUL} + \mathrm{PMUL} + \mathrm{ZMUL}. \tag{3.1}$$

Figure 3.4 is an example of the TMUL distributions at $1.528A$ GeV. All distributions are weighted by the scaling factors of each trigger. Each line and symbol corresponds to each trigger events, i.e., solid line and open triangle for the minimum, dashed line and open square for the medium, and dashed-dotted line and open circle for the central bias events. The symbols in figure 3.4 depict the TMUL distributions after applying the cut for rejecting oxygen contamination. One has to point out that the cut for rejecting oxygen contamination gives reasonable result. For instance, the TMUL distribution of the collisions on ZrO_2 target shows a shoulder around TMUL $\sim$50 for minimum and medium bias events, which is absent in collisions with Ru target. After applying the cut, the shoulder disappears as shown in the symbols. For central events, similar modification on the TMUL distributions occurs. However, this cut limits the peripheral event selection and one has to take it into account for the centrality selection. For example, the TMUL distribution $\geq$ 75 for Zr + Zr minimum bias events is trustworthy for the centrality selection without influence from the cut, and the integration of the distribution $\geq$ 75 region gives the geometrical cross section of 650 mb.

Solid line distributions in figure 3.4 correspond to the minimum bias trigger events and the full integral of these distributions gives the total geometrical cross section in principle. The total geometrical cross section and the maximum geometrical impact parameter can be calculated by the following formulae based on the geometrical sharp cut off approximation:

$$\sigma_{geo} = 10 \cdot \pi \cdot (R_{projectile} + R_{target})^2 \quad \text{(mb)} \tag{3.2}$$

with

$$R = r_o \cdot A^{1/3}, \quad r_o = 1.2 \text{ fm}, \tag{3.3}$$

and

$$b_{geo} = \sqrt{\frac{\sigma_{geo}}{10 \cdot \pi}} \quad \text{(fm)}. \tag{3.4}$$

According to these formulae, the geometrical cross section and the maximum geometrical impact parameter are 3800 mb and 11 fm for the Ru(Zr) + Ru(Zr) collisions. Unfortunately, the minimum bias event distributions(solid lines) do not correspond to the total geometrical cross section in reality. At the low multiplicity region in the TMUL distributions, the contamination by the background events is large. In addition, particles are not able to be measured

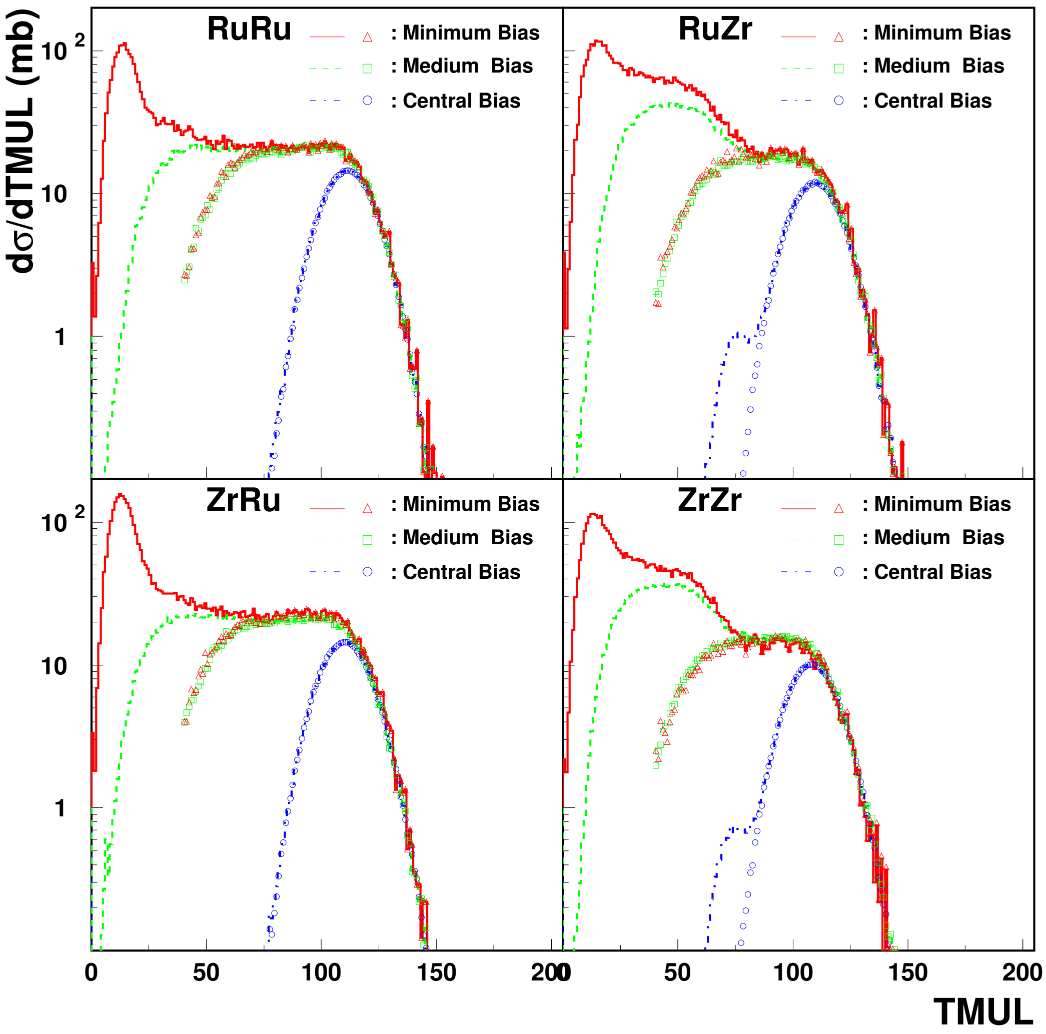

Figure 3.4: Total charged particle multiplicity(TMUL) distributions at 1.528A GeV: Ru + Ru collisions(upper left), Ru + Zr collisions(upper right), Zr + Ru collisions(lower left), and Zr + Zr collisions(lower right). All distributions are weighted by the scaling factors of each trigger. See the text for more details.

in very peripheral collisions due to the experimental limitations. Despite of it, we can still integrate the multiplicity distribution of certain region for the collision centrality.

The multiplicity distributions exhibit a typical plateau for intermediate values and falls off for the highest multiplicities [44]. The events are sorted by the correlation between the multiplicity and impact parameter which is demonstrated in figure 3.5. Plots in figure 3.5 are the results from the IQMD simulations under filtering detector geometry. One can notice that the correlation has saturation at the high multiplicity region, which means that the centrality selection with TMUL is not sensitive enough for resolving very central collision events. The standard method of selecting centrality with the multiplicity is following. The highest multiplicity bin is defined by cutting at half of the plateau value and the rest part of the distribution is subdivided into four equally spaced bins. Also, each of multiplicity bins can be subdivided into several bins if necessary.

E_{rat} Variable

As already mentioned above, E_{rat} is defined as the ratio of the total transverse ($E_{\perp}$) to longitudinal ($E_{||}$) kinetic energies at the center-of-mass system:

$$E_{rat} = \sum_{i=1}^{M} E_{\perp,i} / \sum_{i=1}^{M} E_{||,i}, \tag{3.5}$$

where M is the measured baryonic multiplicity at the CDC and the PLAWA in an event. Higher E_{rat} values correspond to the central events and vice versa. Figure 3.6 demonstrates the correlation between impact parameter and E_{rat}. On the contrary to figure 3.5, figure 3.6 shows no saturation at the high E_{rat} region and the linear correlation from the most central to the mid-central impact parameter ranges exists. Therefore, E_{rat} is a suitable variable to select the most central event classes [9, 11, 25, 44, 47]. For the experimental data, a similar effect can be seen in the correlation of E_{rat} and TMUL, which is the upper plot of figure 3.7. The saturation effect above the TMUL values of 80 is found in Ru + Ru collisions at 1.528A GeV. In addition, the plot shows that some of E_{rat} values are correlated to the lower TMUL and it can drive the wrong centrality selection. In order to avoid this, one has to apply

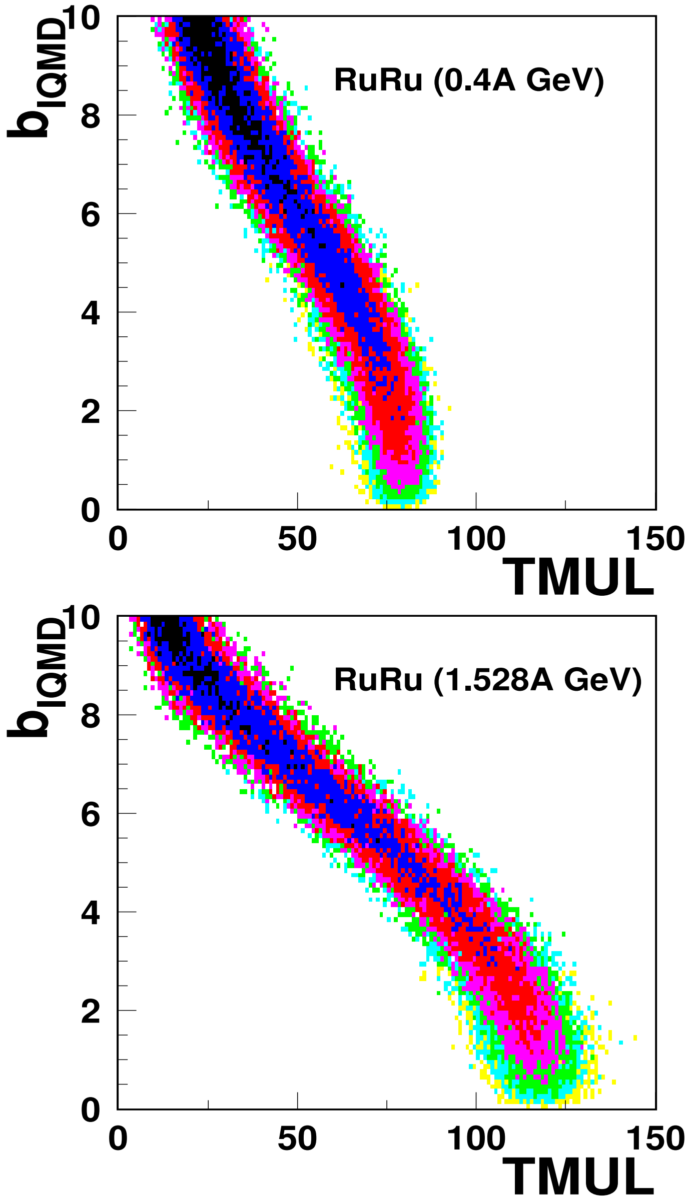

Figure 3.5: Correlation between impact parameter and TMUL in the IQMD simulations in Ru + Ru collisions at $0.4A$(top) and at $1.528A$(bottom) GeV. Both plots show clear correlation between two variables.

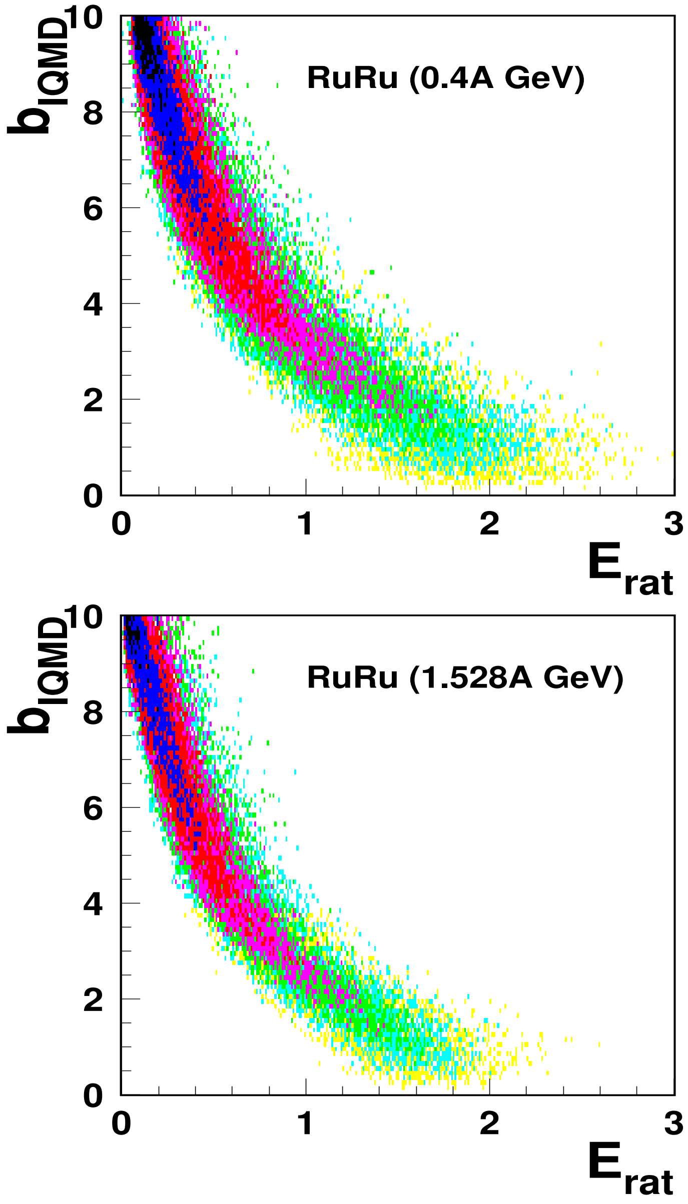

Figure 3.6: Correlation between impact parameter and E_{rat} in the IQMD simulations in Ru + Ru collisions at $0.4A$(top) and at $1.528A$(bottom) GeV.

the low TMUL cut for the calculation of E_{rat} and the cut(TMUL $\geq$ 40) for 1.528A GeV data is applied in the following analysis as depicted by line.

In this thesis, the centrality of events is determined by E_{rat}. Each of experimental E_{rat} distributions at 0.4A GeV, which corresponds to the measured geometrical cross section at the minimum bias trigger, is given in the lower plot of figure 3.7. Figure 3.8 shows E_{rat} distributions at 1.528A GeV in which the cut for the rejection of oxygen contaminated events(CMUL $\geq$ 17) and the lower TMUL cut(TMUL $\geq$ 40) are applied. All plots in figure 3.8 are weighed by the scaling factors of each trigger. The centrality selections for the analysis are summarized at Table 3.1 for both energies.

E$_{beam}$ (A GeV)	System	Centrality	E_{rat}	σ_{geo} (mb)	b_{geo} (fm)
0.4	Ru + Ru	E_{rat} A	$\geq$ 1.40	$\leq$ 116	$\leq$ 1.9
		E_{rat} B	1.05 - 1.40	116 - 235	1.9 - 2.7
		E_{rat} C	0.80 - 1.05	235 - 302	2.7 - 3.1
		E_{rat} D	0.60 - 0.80	302 - 432	3.1 - 3.7
	Ru + Zr	E_{rat} A	$\geq$ 1.43	$\leq$ 119	$\leq$ 1.9
	Zr + Ru	E_{rat} A	$\geq$ 1.47	$\leq$ 118	$\leq$ 1.9
	Zr + Zr	E_{rat} A	$\geq$ 1.48	$\leq$ 116	$\leq$ 1.9
1.528	Ru + Ru	E_{rat} A	$\geq$ 0.91	$\leq$ 67	$\leq$ 1.5
		E_{rat} B	0.72 - 0.91	67 - 197	1.5 - 2.5
		E_{rat} C	0.57 - 0.72	197 - 378	2.5 - 3.5
		E_{rat} D	0.44 - 0.57	378 - 627	3.5 - 4.5
	Ru + Zr	E_{rat} A	$\geq$ 0.89	$\leq$ 67	$\leq$ 1.5
	Zr + Ru	E_{rat} A	$\geq$ 0.92	$\leq$ 71	$\leq$ 1.5
	Zr + Zr	E_{rat} A	$\geq$ 0.86	$\leq$ 73	$\leq$ 1.5

Table 3.1: Centrality selections with E_{rat} distributions. The most central collision criterion has been determined for all of four systems at both energies. For Ru + Ru collisions at both energies, less central event classes are also determined for further analysis.

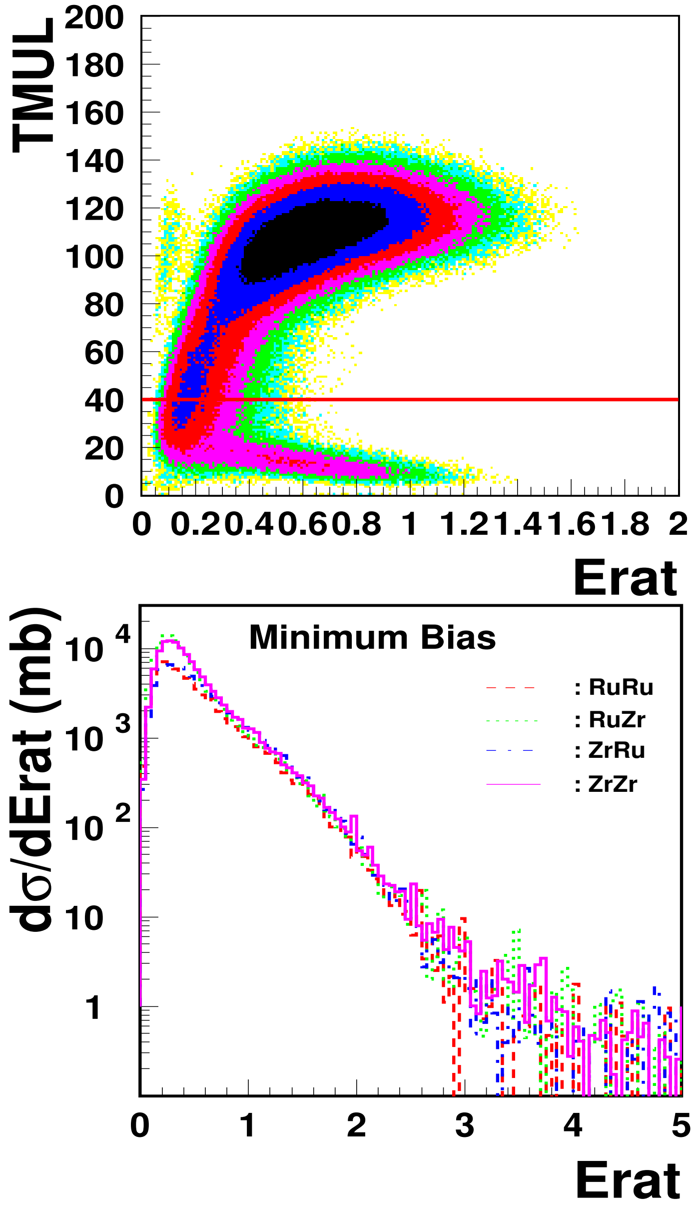

Figure 3.7: Correlation between TMUL and E_{rat}(top) in Ru + Ru collisions at 1.528A GeV, and E_{rat} distributions of the minimum bias events(bottom) at 0.4A GeV.

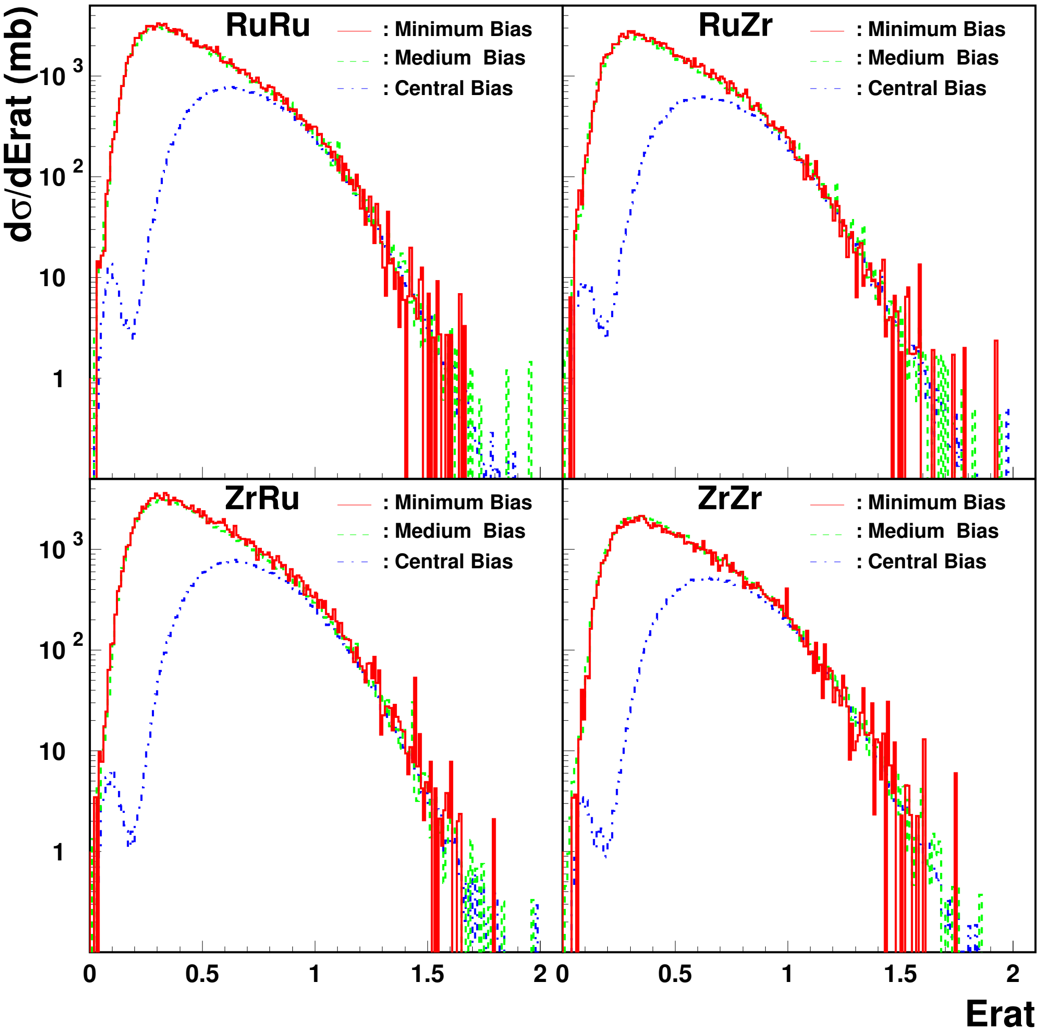

Figure 3.8: E_{rat} distributions in Ru + Ru(upper left), Ru + Zr(upper right), Zr + Ru(lower left), and Zr + Zr(lower right) collisions at 1.528A GeV. All distributions are weighted by the scaling factors of each trigger. The cut for rejecting oxygen contamination and the low TMUL threshold value are applied.

3.1.5 Autocorrelation Effect

Typically, the autocorrelation effect causes a distortion of the spectra by the momentum space topologies. If the produced particles have a collective movement, the particle of interest has a large probability to follow the rest. It makes that E_{rat} value is increased and the event is interpreted as more central than reality. In this case, the width of particle rapidity distribution($dN/dy^{(0)}$) becomes narrower and the height of the distribution becomes higher. Also, in the flow analysis, the autocorrelation effect generates an artificially enhanced flow of particles [68]. In order to remove the autocorrelation effect, the particle of interest should be excluded from the calculation of E_{rat} when constructing E_{rat} selected single particle observables such as rapidity distribution or flow profile. In addition to the flow analysis, one has to exclude the particle of interest when the reaction plane is reconstructed. Figure 3.9 is the IQMD simulation results of Ru + Ru collisions at $0.4A$ GeV. The upper plot shows the proton rapidity distribution for $b_{geo} \leq 2$ fm by E_{rat} and the lower plot is the proton flow profile for b_{geo} between 4 - 6 fm by the the TMUL. Both plots show sizeable autocorrelation effect and these effects are more pronounced in experimental data.

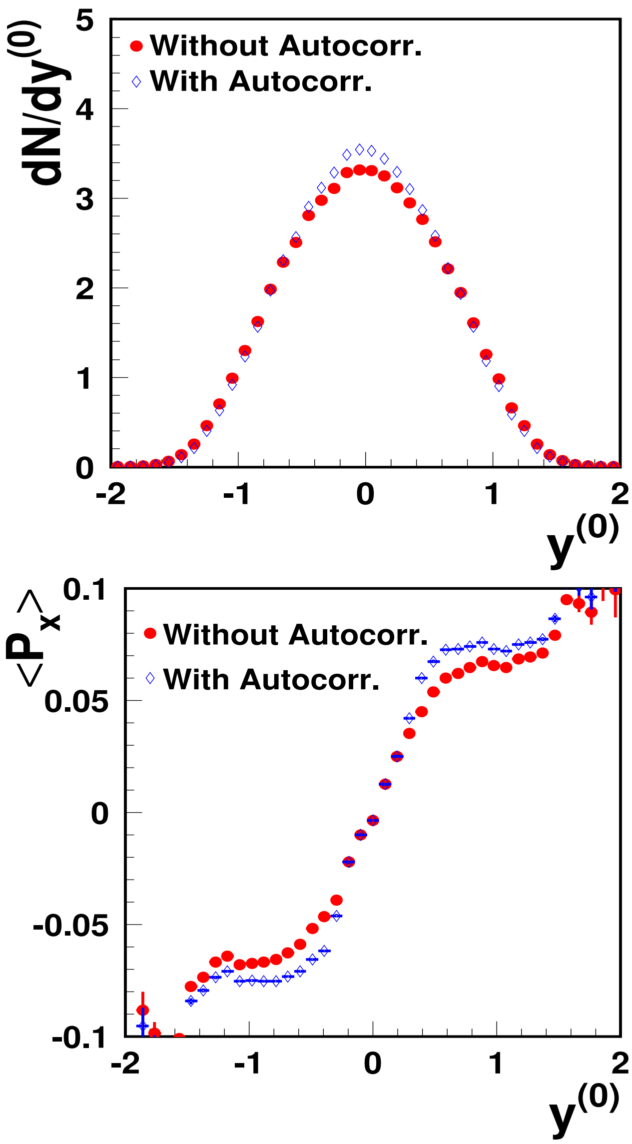

Figure 3.9: Autocorrelation effects at the rapidity distribution(top) and the flow profile(bottom) of protons. The results with(without) the autocorrelation effect are depicted by open diamonds(closed circles). All results are from the IQMD simulation of Ru + Ru collisions at $0.4A$ GeV. See the text for more details.

3.2 Track Selection and Particle Identification

In this section, track selection and particle identification at both the CDC and the Helitron will be discussed.

3.2.1 CDC

d0 and *z0*

As mentioned at the previous section 2.2.2, one has to consider the minimum distances between each track and the primary vertex as they can be used to judge the quality of the tracks. It is physically possible that some of tracks do not point to the primary event vertex because they are not originated from the primary vertex. For example, if they are daughter particles from weakly decaying resonances. However, it is also possible that some of tracks show large deviations of *d0* and *z0* due to imperfect detector resolution and wrong track reconstruction. The deviation of *d0* is mainly comes from the reconstructed mirror tracks, whereas the large *z0* distribution is due to the finite hit resolution along the z-axis. As mentioned earlier, we let all tracks in $|d0| \leq 0.5$ cm and $|z0| \leq 20$ cm refitted by fixing the origin at the primary vertex, but we also recycle the abandoned tracks out of these criteria. According to M. Stockmeier [69], the free fitted *d0* and *z0* values of tracks have the momentum dependence as demonstrated in figure 3.10. Both free fitted *d0* and *z0* distributions are wide at low momentum and they become narrower going to higher momentum. In this thesis, the free fitted *d0* and *z0* distributions are subdivided into each 100 MeV/c momentum bin, and each of them is fitted by the Gaussian function. For the cuts on free fitted *d0* and *z0*, $\pm3\sigma$ cuts on them with respected to mean values in a given momentum bin are taken for the following analysis. The result is shown in figure 3.10 by open(for the mean values) and closed(for the $\pm3\sigma$ values) symbols.

Particle Identification

As discussed in the section 2.2.2, particle identification in the CDC is based on the momentum and the specific energy loss of the reaction products.

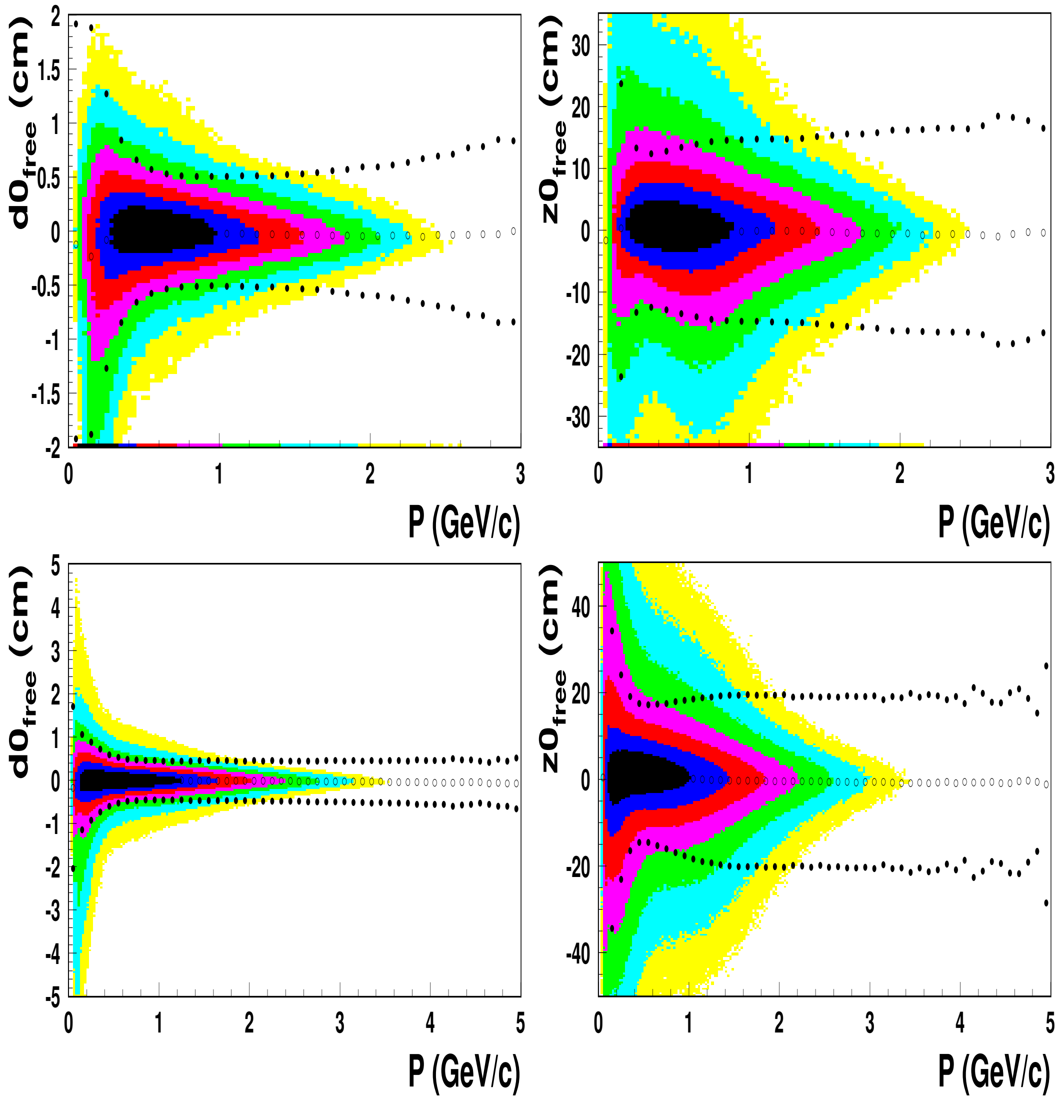

Figure 3.10: Distances between individual track and the primary vertex. $d0$($z0$) is defined as the distance in the xy plane(z-axis). Upper plots are at $0.4A$ GeV and lower plots are at $1.528A$ GeV in Ru + Ru collisions. Left(right) column is the momentum dependence of $d0$($z0$). The mean values from the results of fitting with the Gaussian function on $d0$($z0$) in a given momentum bin are depicted by open circles and $\pm 3\sigma$ cuts are illustrated by closed circles.

As shown in figure 2.11, particle mass can be reconstructed by the parameterized Bethe-Bloch formula. By linearizing these fitted functions, we obtain the mass distributions of the CDC(we call it as the CDC mass) shown in figure 3.11. Each distribution in figure 3.11 shows the separated and developed particle mass peaks around their nominal mass values in the Particle Data Group Table [58]. However, plots in figure 2.11 show that there is ambiguity in between particles especially at high momentum. As a result of it, one can not clearly judge the particle type of reaction products at the valley regions in the CDC mass distributions. Together with the Plastic Barrel, the correlation between the momentum information from the CDC and the velocity information from the Plastic Barrel enhances the capability of the particle identification, but the detector acceptance of the Plastic Barrel is limited. Additionally, one may use the correlation between the mass and the momentum of particles in the CDC, and it helps to judge the limit of the particle identification for a given momentum. The shaded areas in figure 3.11 indicate the selected mass ranges of protons and deuterons in this analysis. Different momentum cuts are applied to different particle species if necessary.

3.2.2 Helitron

Geometrical Matching

In order to separate isotopes from reaction products at forward hemisphere, one has to use Helitron and the PLAWA. It can be done with charge and velocity information from the PLAWA and momentum and the specific energy loss information from Helitron. Both detectors cover θ_{Lab} from 7° to 30° in the full azimuth, but θ_{Lab} between 9° and 26° are reliable region where particles are passing through the full depth of Helitron along the z-axis. In the reliable θ_{Lab} region, the geometrical matching between the track in the Helitron and the hit in the PLAWA has been performed for the differences in θ and ϕ: $\Delta\theta$ from -5° to 9° depending on the θ values and $\Delta\phi < \pm 7°$, where $\Delta\theta(\Delta\phi)$ is defined by $\theta(\phi)_{\mathrm{Helitron}}$-$\theta(\phi)_{\mathrm{PLAWA}}$. With these cuts, the most of proton candidates are accepted, but many of background tracks are rejected at both beam energies.

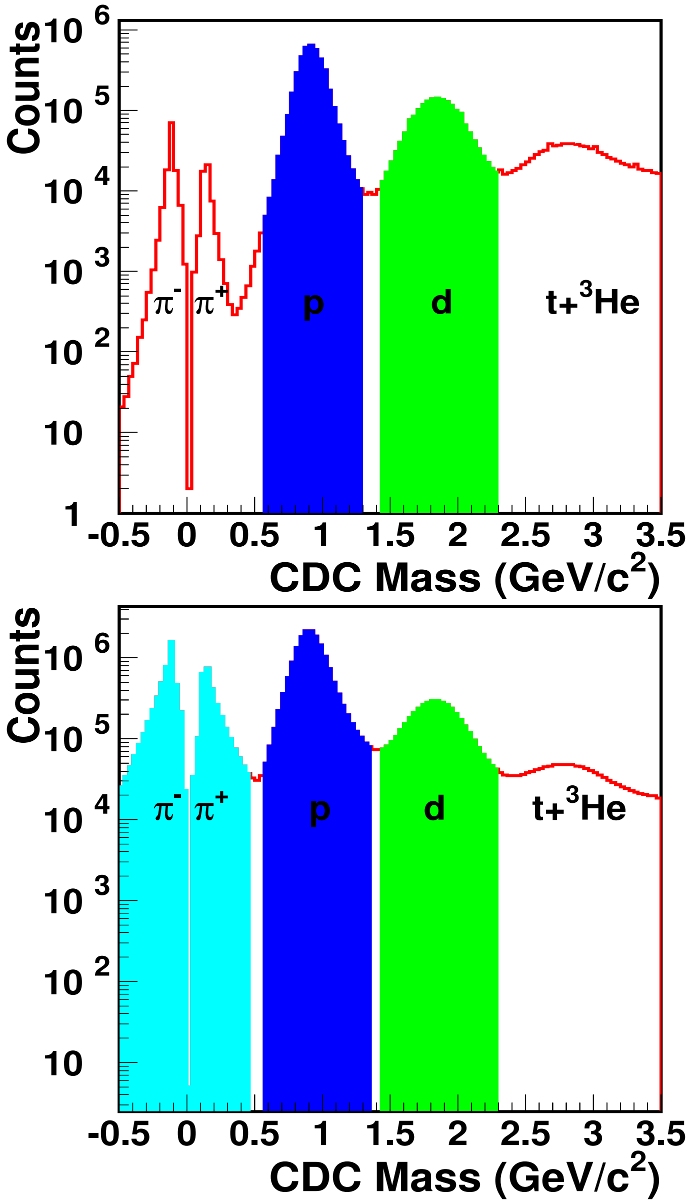

Figure 3.11: CDC mass distributions in Ru + Ru collisions at $0.4A$(top) and $1.528A$(bottom) GeV. Shaded mass ranges correspond to the selected mass regions for this analysis.

Particle Identification

Particle identification in the Helitron is basically similar to that in the CDC. In addition to the particle selection in the Helitron mass distributions in figure 3.12, the correlation between momentum from the Helitron and the velocity from the PLAWA in figure 2.13 is used, which enhances the signal to background ratio. However, plots in figure 2.13 show large overlap of each particle branch with huge background at low velocity and negative particle regions. It is due to the small active area of Helitron, which causes the sign ambiguity of the track curvature and the problem of the rejection for mirror tracks. These problems result in the limited capability of the particle identification in the Helitron in that the pion peak in the mass distribution has a huge background with relatively small reconstruction efficiency, although the peak itself is clearly visible. However, the isotopic separation is still possible above certain mass value in the Helitron mass distribution with the help of the correlation between momentum and velocity. Particle identification done for this analysis is depicted in figure 3.12 by the shaded mass ranges.

After particles are identified, the phase-space of protons in the normalized transverse momentum versus the normalized rapidity are plotted as shown in figure 3.13. θ_{Lab} cuts on the CDC and the Helitron are added by solid lines.

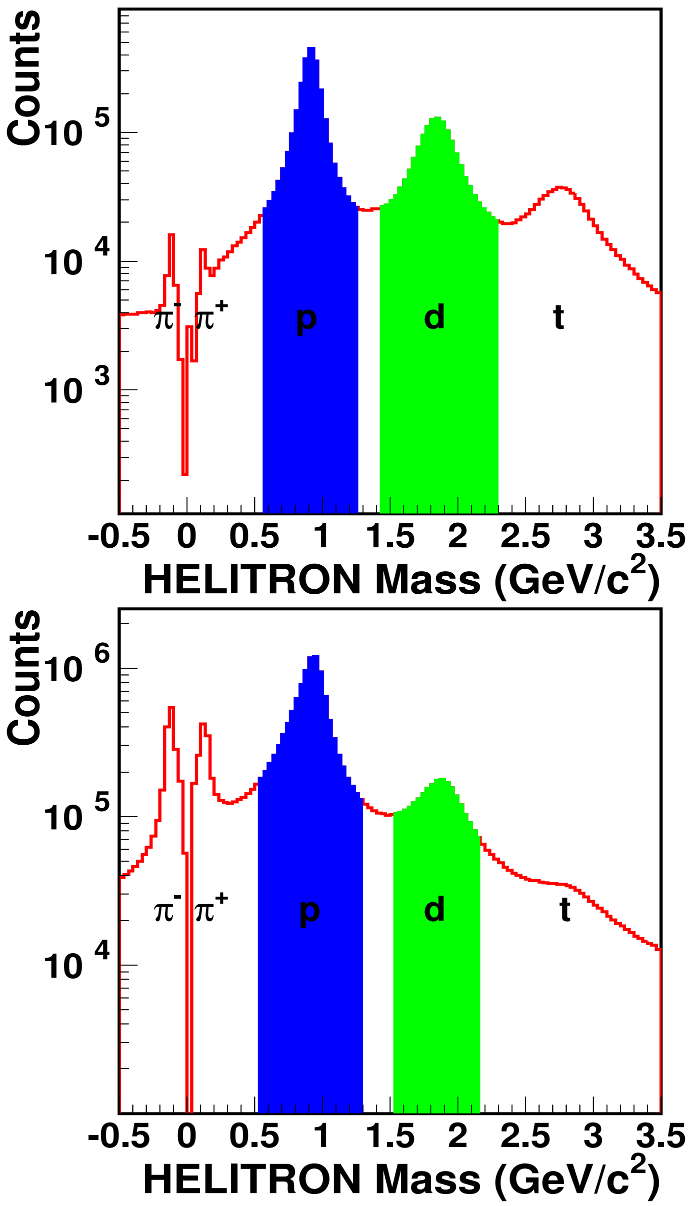

Figure 3.12: Helitron mass distributions in Ru + Ru collisions at $0.4A$(top) and $1.528A$(bottom) GeV. Shaded mass ranges correspond to the selected mass regions for this analysis.

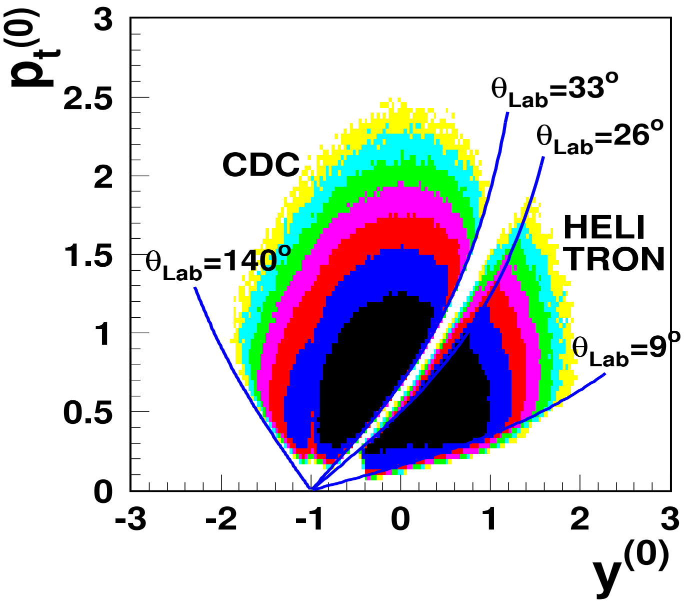

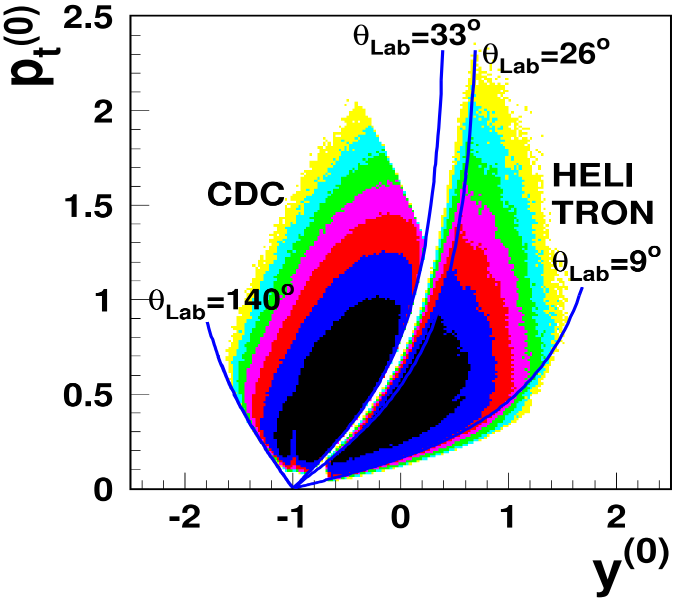

Figure 3.13: Phase space distributions of protons in Ru + Ru collisions at $0.4A$(top) and $1.528A$(bottom) GeV. Solid lines indicate various θ_{Lab} cuts on the CDC and the Helitron.

3.3 Efficiency Correction

In reality, there are always some deficiencies of the track reconstruction due to the finite detector resolution, and, background contamination, etc. In addition, various track quality cuts remove not only background tracks but also some of good tracks. Therefore, one has to take these effects into account to correct the raw spectra. In this section, the tracking efficiency in the CDC and matching efficiency between the Helitron and the PLAWA are discussed.

3.3.1 CDC Efficiency

In order to estimate the CDC tracking efficiency, a simulation has been extensively performed by using the GEANT package [65] with the IQMD as an event generator. The GEANT simulation package contains the CDC geometry and its materials, which enable to us to simulate the CDC response to particles passing through it. The IQMD model generates events with various particles, and these events are used as input to the GEANT. In the GEANT simulation, particles in the IQMD event are propagated to the CDC volume, and subsequently, they produce drift electrons along their trajectories. The drift electrons, then, generate signals on sense wires and such signals go through all read out hardware. The GEANT simulation provides various effects as real data. We can tune up various parameters for making the simulation data as close as real ones. After this adjustment, the simulated data are analyzed in the same way as real data by using the user analysis code as well as the same tracking algorithm. Input kinematical information as well as final output track information is saved on ZEBRA data banks which are used for the determination of the tracking efficiency of the CDC.

The tracking efficiencies of Z=1 baryon and proton as a function of momentum and transverse momentum for impact parameter $b \leq 1.5$ fm in Ru + Ru collisions at 1.528A GeV are given in figure 3.14. Figure 3.14 show the efficiencies of Z=1 baryon and proton have similar trend as they are higher at low (transverse) momentum and decrease with higher momentum. In particular, the effect of target due to the absorption is significant around the target rapidity region(-1.1 $\leq y^{(0)} \leq$ -0.9) so that we treat it separately. The efficiencies of Z=1 baryon and proton without applying user cut conditions are estimated about 94% out of the target rapidity region and about 80% around the target region. The ratio of the number of particles after to before applying user cuts is around 0.87 for both the IQMD simulation and experimental data. It tells that the user cut efficiency is around 87% and it is reliable for both simulated and experimental data. For the simulation at 0.4A GeV, all estimated efficiencies are slightly higher than them at 1.528A GeV as expected. For instance, the proton tracking efficiencies are about 90% with applying user cuts and almost 100% without the cuts, and the user cut efficiency is estimated about 90% for the simulation and this agree with the analysis results of real data.

Figure 3.15 shows the proton tracking efficiency as a function of rapidity in Ru + Ru collisions at 0.4A GeV. We find that the efficiency is changed from ~100% at forward rapidity to ~70% below the target rapidity region. For protons and deuterons in the CDC, each efficiency value in each rapidity window is applied for the correction of the single particle invariant spectra.

For 1.528A GeV, the tracking efficiencies of π^-, π^+, proton, deuteron, and Z=1 baryon are individually determined as a function of transverse momentum. For the most central collisions(E_{rat} A, $b \leq 1.5$ fm), the tracking efficiencies of $\pi^{\pm}$ as a function of transverse momentum at out of the target rapidity region are given in figure 3.16. The efficiencies are ~83% for π^- and ~70% for π^+ except very low P$_t$ region. The tracking efficiencies of Z=1 baryons and protons for the same centrality are shown in figure 3.17. Figure 3.17 show that the efficiency has strong dependence on transverse momentum. In order to minimize the statistical fluctuation, each efficiency profile in a given rapidity range is fitted by linear function within a certain transverse momentum range. The fit results are depicted over full transverse momentum range by solid lines in figure 3.17. In a given rapidity range, the tracking efficiencies of pions, proton, deuteron, and Z=1 baryon are estimated by using this fitting method for the corrected invariant single particle spectra of each particle species. In addition, the tracking efficiencies of protons and deuterons are determined for other centralities in Table 3.1. The dependence on transverse momentum becomes smaller as we go to peripheral collisions and the efficiency profile has the plateau distribution when the impact parameter is between 3.5 and 4.5 fm. The efficiencies in various centrality conditions do not change much: ~80 - 85% at the mid-rapidity and at out of the target

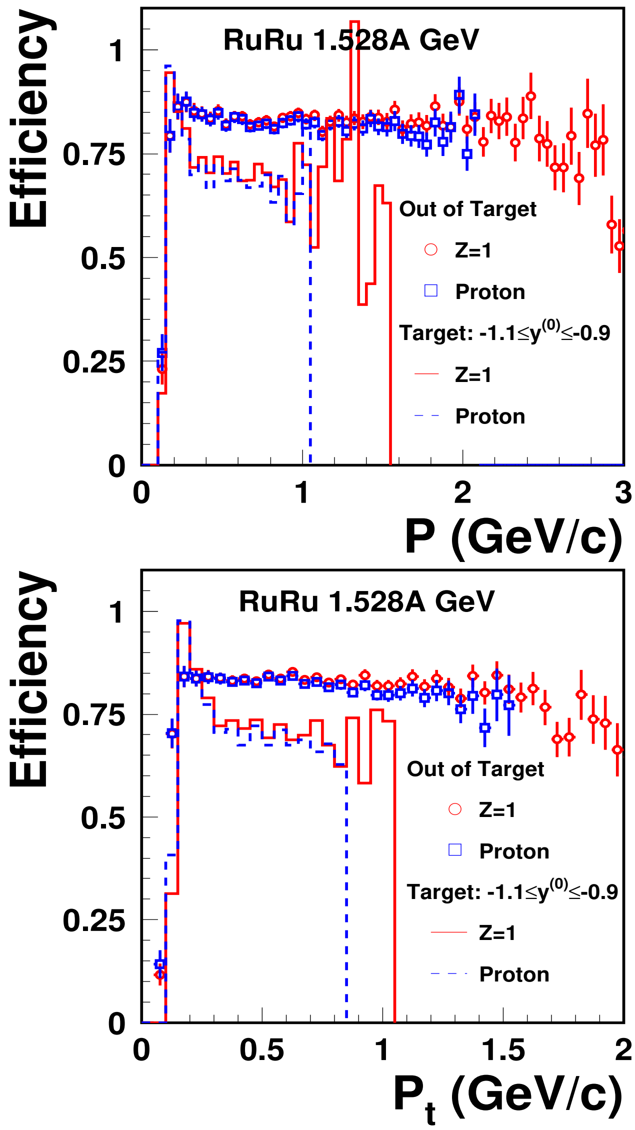

Figure 3.14: Track reconstruction efficiencies of Z=1 and proton as a function of momentum(top) and transverse momentum(bottom) in the CDC. The efficiency is estimated by the GEANT simulation in Ru + Ru collisions at 1.528A GeV. Efficiency around the target rapidity region is depicted by lines and that at the other rapidity region is shown by symbols.

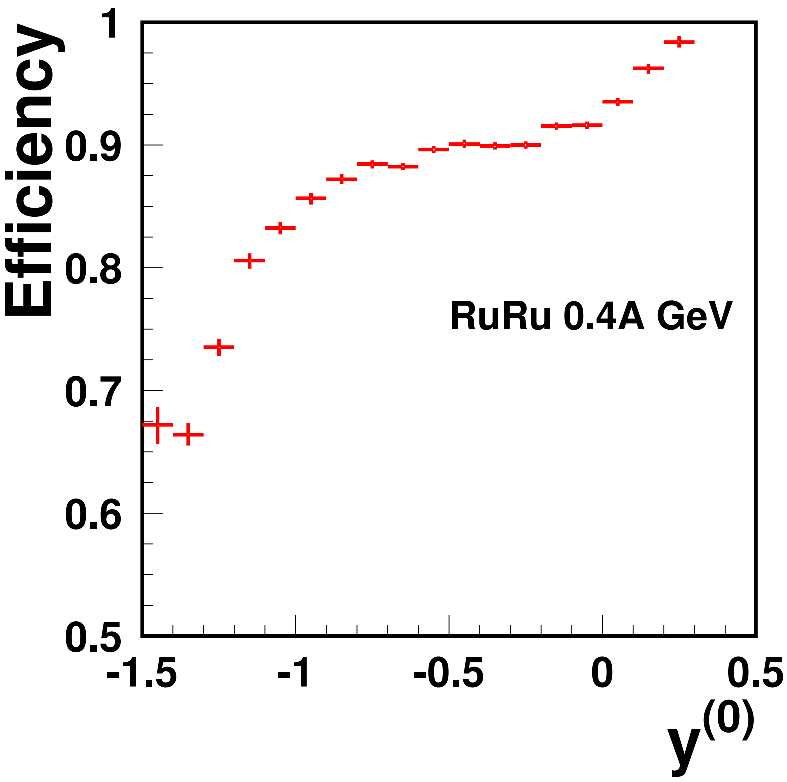

Figure 3.15: Efficiency of protons as a function of rapidity in the CDC. The efficiency is estimated by the GEANT simulation in Ru + Ru collisions at 0.4A GeV.

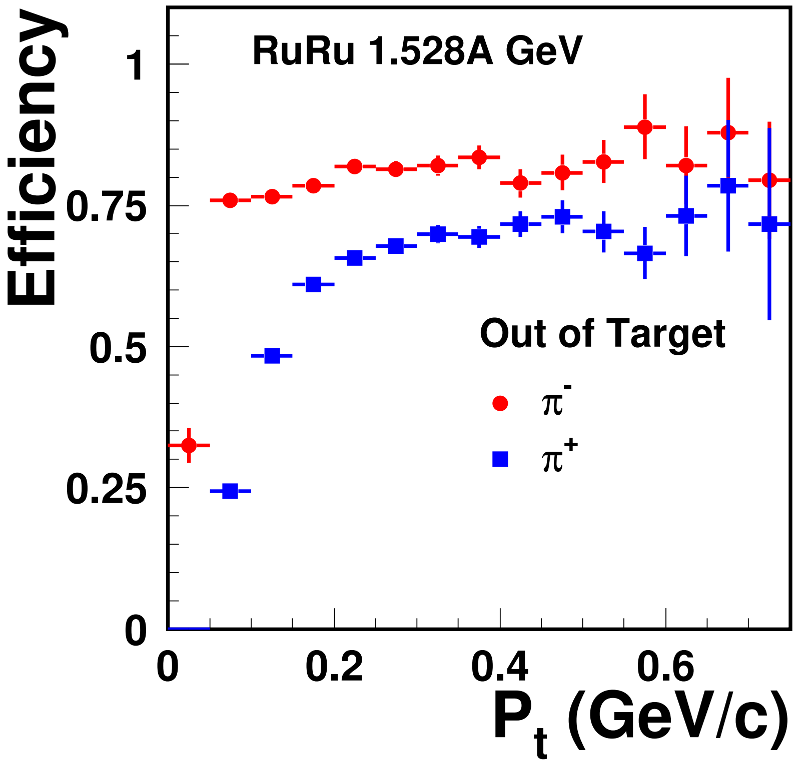

Figure 3.16: Efficiencies of π^- and π^+ as a function of transverse momentum at out of the target region in the CDC. The efficiency is estimated by the GEANT simulation in Ru + Ru collisions at 1.528A GeV.

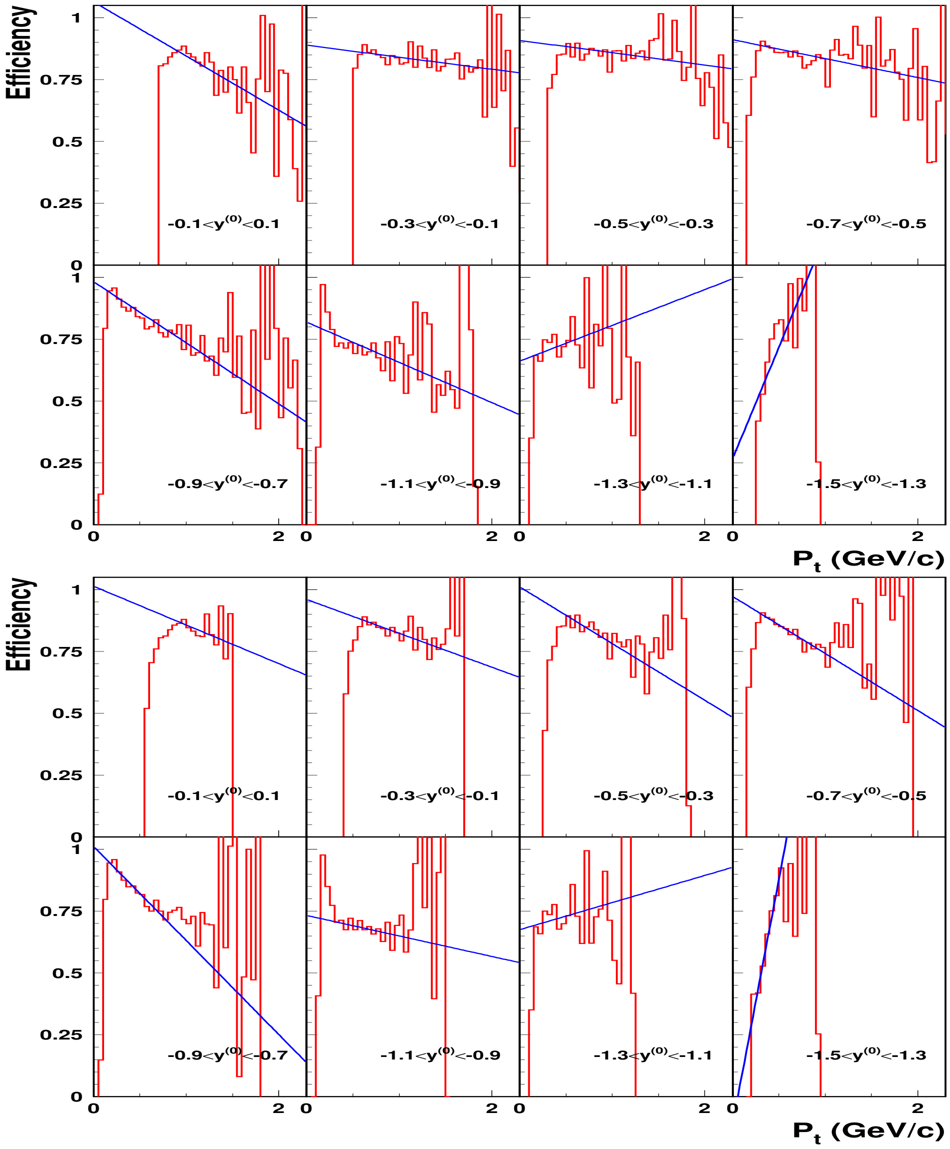

Figure 3.17: Efficiencies of Z=1 baryon(top) and proton(bottom) as a function of transverse momentum in a given rapidity range for events with impact parameter $\leq$ 1.5 fm. The lines are fit results. The efficiencies are estimated by the GEANT simulation in Ru + Ru collisions at 1.528A GeV.

region.

3.3.2 Helitron/PLAWA Matching Efficiency

The matching efficiency between the Helitron and the PLAWA is estimated by comparing the number of tracks in the Helitron with the number of hits in the PLAWA for θ_{Lab} from 9° to 26°. The limit of this method to evaluate the matching efficiency lies that the result is not for each particle species but for its charge. In addition, since pions in the Helitron have too much uncertainty, one has to reject the pion candidates at both detectors.

For 0.4A GeV, pions are rejected from both detectors by the cut on the Helitron mass although they are not major produced particles. The matching efficiency as a function of θ_{Lab} for Z=1 particles is shown in figure 3.18 which shows the efficiency increases from ~45% at 9° to ~85% at 26°. The efficiency profile is fitted by the fourth order polynomial function. The fit result is applied for the corrected proton and deuteron single particle invariant spectra in this analysis.

For 1.528A GeV, the matching efficiency of Z=1 particles is estimated as a function of $\beta_t\gamma$ for each 0.1 rapidity bins for $b_{geo} \leq 1.5$ fm. In order to reject the pion tracks in the Helitron, one use the cut on the Helitron mass, but it is more complicated for the PLAWA. In order to exclude pion candidates in the PLAWA, the following procedure has been done. First, the single particle spectra of π^- and π^+ for events with $b_{geo} \leq 1.5$ fm in the CDC are analyzed by the invariant form as a function of P_t at each 0.1 rapidity bins. These spectra are corrected by the tracking efficiencies as mentioned in the previous section. The invariant spectra of pions show two slope structure which is due to the resonance decay [39, 70]. The spectra are fitted by the sum of two exponential functions:

$$\frac{1}{2\pi P_t}\frac{d^2N}{dP_t dy^{(0)}} = C_1 \cdot \exp\left(-\frac{m_t}{T_1}\right) + C_2 \cdot \exp\left(-\frac{m_t}{T_2}\right) \tag{3.6}$$

where m_t=$\sqrt{P_t^2 + m_\pi^2}$ is the transverse mass, and C_1, C_2 are the normalization constants, and T_1, T_2 are the inverse slope parameters. The invariant spectra of π^- and π^+ with the fit results are given in figure 3.19. From the

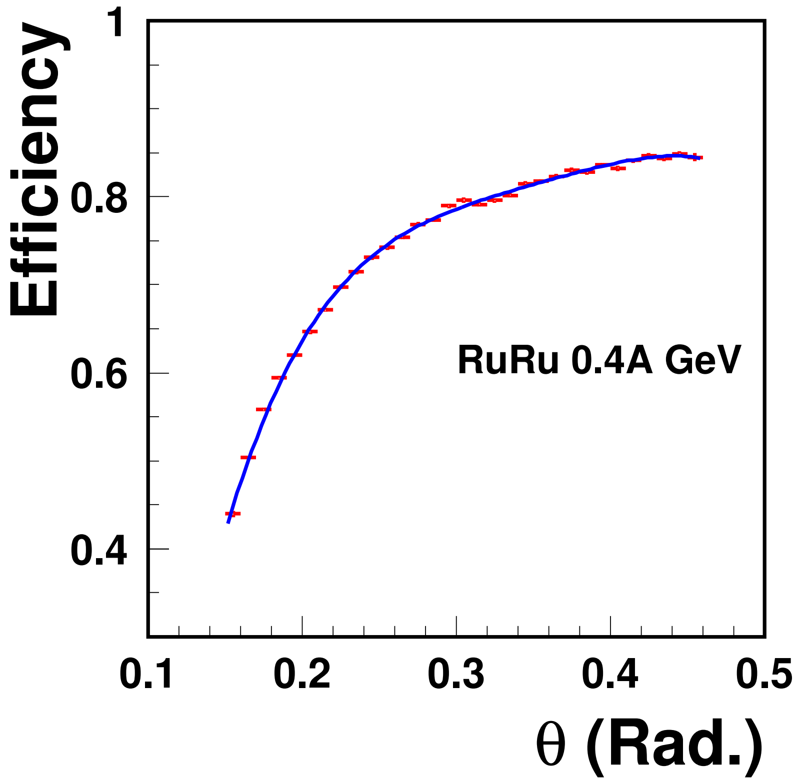

Figure 3.18: Matching efficiency of Z=1 particles between the Helitron and the PLAWA as a function of θ_{Lab} in Ru + Ru collisions at 0.4A GeV. Solid line is the fit result.

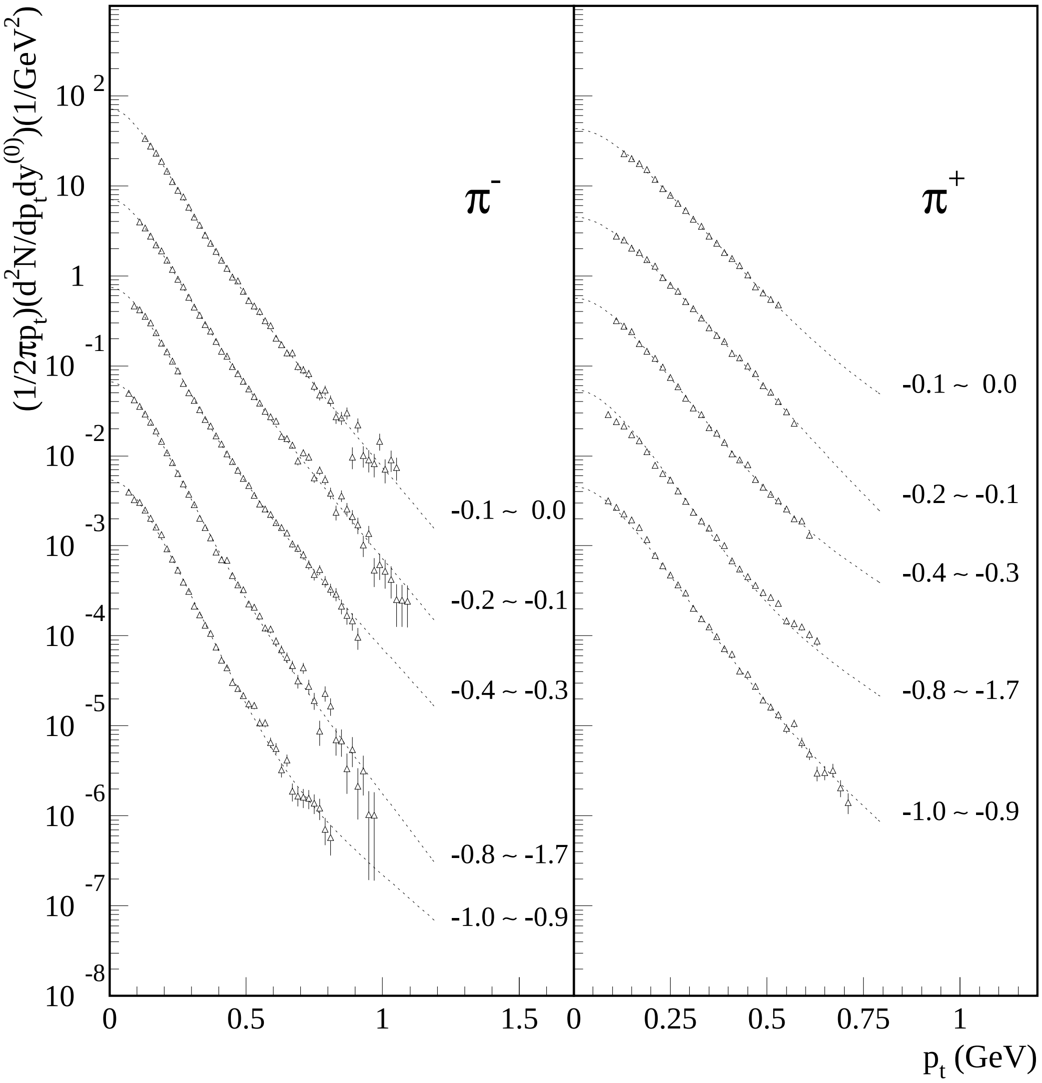

Figure 3.19: Invariant spectra of π^-(left) and π^+(right) as a function of transverse momentum in Ru + Ru collisions at $1.528A$ GeV for events with $b_{geo} \leq 1.5$ fm. The fit results of two exponential functions are depicted by dashed lines. Starting with the uppermost rapidity bin (-0.1 $\sim$ 0.0), each spectrum has been multiplied by a decreasing power of 10 for a clear display.

fit results, one can obtain the conjectured pion $\beta_t\gamma$ distribution in a given rapidity bin in the PLAWA acceptance. These spectra are subtracted from the $\beta_t\gamma$ distribution of Z=1 particles in the same rapidity bin at the PLAWA. Completing this question, we finally compare the $\beta_t\gamma$ distributions of Z=1 baryons between at the Helitron and the PLAWA in a given rapidity bin. The result of the matching efficiencies is shown in figure 3.20. In the beginning and end points of $\beta_t\gamma$, peaks are visible, which comes from the edges of the detector. However, we apply the fiducial cuts, the single particle invariant spectra at these $\beta_t\gamma$ regions are avoided. Figure 3.20 shows that the matching efficiencies between the Helitron and the PLAWA are estimated about 50 - 60% at the lower $\beta_t\gamma$ region and this increases to about 75 - 85% at the highest $\beta_t\gamma$ region. All efficiency distributions are fitted by the fourth order polynomial function and they are depicted by solid lines in figure 3.20. The fit results are used for the correction of the single particle invariant spectra of protons, deuterons, and Z=1 baryons in the Helitron.

The centrality dependence of the matching efficiency between the Helitron and the PLAWA has also been studied. It is known that the mean pion multiplicities are linearly increased by mean number of participants as the values of mean pion multiplicities divided by mean number of participants are constant in Au + Au collisions at 1A GeV [4, 69, 71, 72, 73, 74, 75]. By using the linear dependence of the pion productions on the number of participants, one can correct the fitted functions in the CDC for the most central events to events with different centrality ranges. The correction factor is determined by the ratio of the mean number of participants in the most central collisions to the mean number of participants in the corresponding centrality. Figure 3.21 shows the number of participants as a function of impact parameter which is based on the formula in reference [76]. By using the formula in reference [76], the mean number of participants can be calculated as:

$$< A_{part} >= 2A \cdot \frac{\int_a^b \left(\frac{3\sqrt{2}}{8} \left(2 - \frac{b}{R}\right)^2 - \frac{1}{8} \left(\frac{3\sqrt{2}}{2} - 1\right) \left(2 - \frac{b}{R}\right)^3 \right) \cdot 2\pi b db}{\int_a^b 2\pi b db}. \quad (3.7)$$

The summary of the mean number of participants and the correction factors in different centrality is given in Table 3.2. Similar to the most central collisions, the pion candidates in the PLAWA at different centrality can be rejected by using the corrected functions. The centrality dependence of the matching

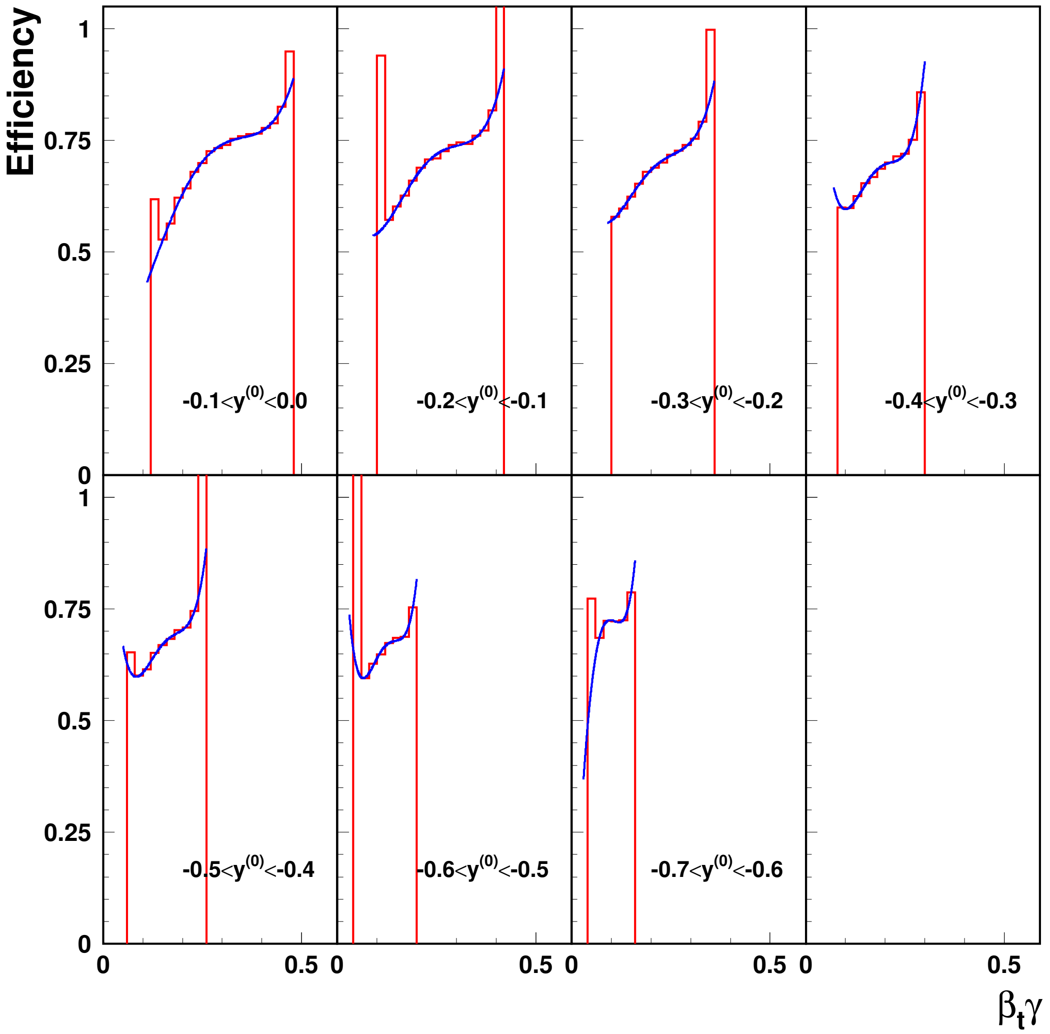

Figure 3.20: Matching efficiencies of Z=1 particles between the Helitron and the PLAWA as a function of $\beta_t\gamma$ in the given rapidity bins for events with b_{geo} $\leq$ 1.5 fm in Ru + Ru collisions at 1.528A GeV. Solid lines are the fit results.

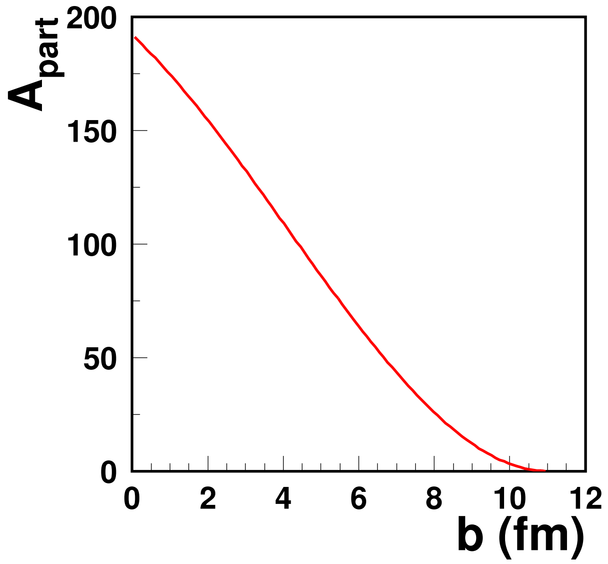

Figure 3.21: Calculated number of participants as a function of impact parameter for Ru + Ru collisions: Details are in the text.

efficiency between the Helitron and the PLAWA is not significant. It is almost the same as the most central collisions. Similar to the most central collisions, all efficiencies are estimated by fitting, and they are applied to the single particle spectra in the Helitron.

E_{rat}	b_{geo} (fm)	$< A_{part} >$	Correction Factor
A	≤ 1.5	175	1
B	1.5 - 2.5	154	0.88
C	2.5 - 3.5	132	0.76
D	3.5 - 4.5	109	0.62

Table 3.2: Mean number of participants and correction factors on the invariant spectra of pions for different centralities in Ru + Ru collisions at 1.528A GeV.

Chapter 4

Results and Discussions

In this chapter, the results of the data analysis at $0.4A$ and 1.528 A GeV are discussed in detail. In addition, the physics discussions based on the comparison with the IQMD model are given.

4.1 Particle Spectra and Rapidity Distributions

For the symmetric collision system of Ru + Ru at $0.4A$ and $1.528A$ GeV, the invariant spectra of particles and its rapidity distributions are discussed. The results of the mean rapidity shift as a function of centrality are also presented. The comparison between the data and the IQMD model for the most central collisions at both energies are presented in the end.

4.1.1 Particle Spectra

The invariant spectra of protons and deuterons in Ru + Ru collisions at $0.4A$ and $1.528A$ GeV at four centrality conditions are analyzed. In addition, the invariant spectra of π^-, π^+, and Z=1 baryons are also analyzed for the most central collisions(E_{rat} A, $b_{geo} \leq 1.5$ fm) in Ru + Ru collisions at $1.528A$ GeV. All invariant spectra in the CDC and the Helitron are corrected as discussed in section 3.3. The resultant spectra are fitted by the simple thermal blast formula, which was proposed by Siemens and Rasmussen(equation 4.1) [77], in order to get missing P_t ranges due to the detector acceptance and their rapidity distributions except pions at 1.528A GeV(for the exception, see section 3.3.2).

$$\frac{1}{2\pi P_t}\frac{d^2N}{dP_t dy^{(0)}} \propto E\exp\left(-\gamma_r E/T\right)\cdot\left[\left(\gamma_r+\frac{T}{E}\right)\frac{\sinh\alpha}{\alpha}-\frac{T}{E}\cosh\alpha\right] \quad (4.1)$$

where E and P are the total energy and momentum of the particle in the center-of-mass frame. Here, $\gamma_r = 1/\sqrt{1-\beta_r^2}$ and $\alpha = (\gamma_r \cdot \beta_r \cdot P)/T$. In equation 4.1, the radial flow velocity β_r and the thermal freeze-out temperature T are free fitting parameters. Figures 4.1 and 4.2 show the invariant spectra of protons and deuterons for the most central collisions with the fit results depicted by the dotted lines at both energies.

In figure 4.1, the invariant spectra at 0.4A GeV show a rather good matching between the CDC and the Helitron. A good matching is also observed between the forward and backward center-of-mass hemispheres. In principle, these spectra should be same in symmetric collision systems such as Ru + Ru. If one compares these spectra in detail, the spectra are differed in 10% for protons and in about 20% for deuterons between the CDC and the Helitron for the most central collision case. Note that, the invariant spectra at 1.528A GeV are only available in the backward center-of-mass hemisphere. One of reasons for using only backward hemisphere at higher energy is the limitations of the acceptance and the particle identification in the CDC. For example, one can see it clearly in the deuteron invariant spectrum in the rapidity bin -0.1 $\sim$ 0.0 in figure 4.2. Another reason is a large discrepancy between spectra in the backward center-of-mass hemisphere by the CDC and the forward center-of-mass hemisphere by the Helitron. This problem comes from the bad performance of the Helitron with the momentum above 1 GeV/c [66].

The invariant spectra of protons and deuterons at 0.4A GeV have been fitted simultaneously by using the reflection symmetry of the collision system. The fitting quality is estimated by the χ^2 per degree of freedom, which ranges from 0.8 to 1.5 for all rapidity bins independent of the centrality selections. For 1.528A GeV, the χ^2 per degree of freedom of the invariant spectra of

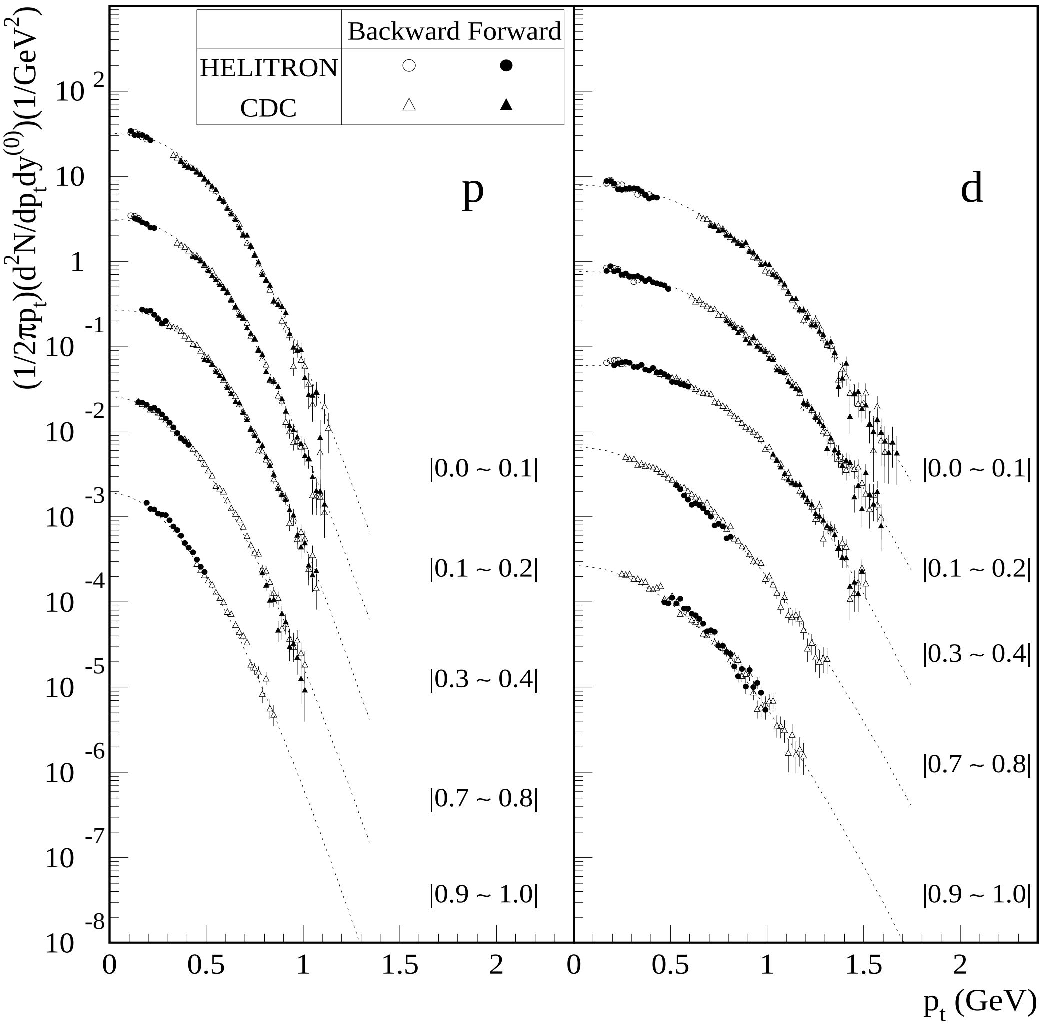

Figure 4.1: Invariant spectra of protons and deuterons in Ru + Ru collisions at 0.4A GeV in various rapidity bins for the most central collisions(E_{rat} A). Spectra are fitted by a simple thermal blast model and the results are depicted by dotted lines. Starting with the uppermost rapidity bin($|0.1 \sim 0.2|$), each spectrum is multiplied by a decreasing order of 10 for a clear display. Triangle and circle symbols denote data from the CDC and the Helitron, respectively. Open and closed symbols represent the spectra in backward and forward hemispheres in the center-of-mass, respectively.

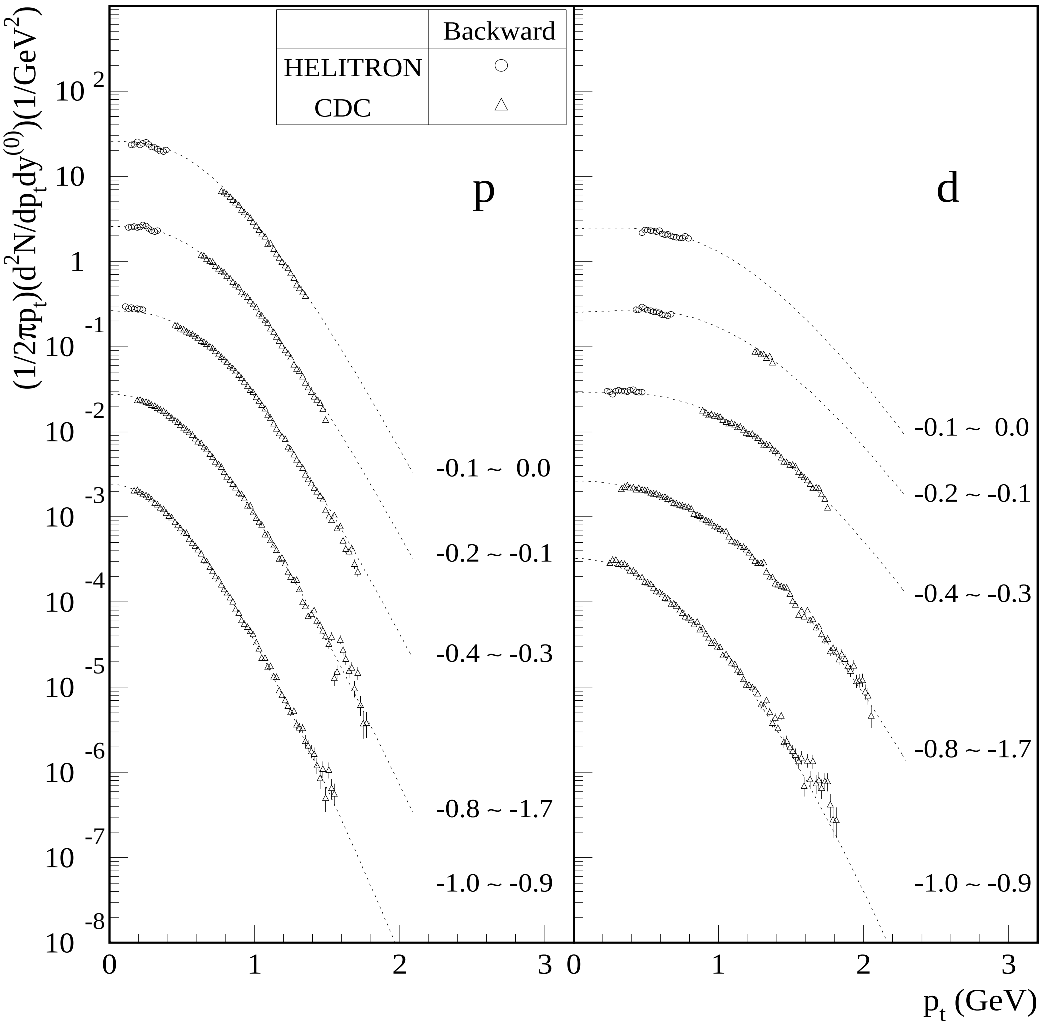

Figure 4.2: Invariant spectra of protons and deuterons in Ru + Ru collisions at 1.528A GeV in various rapidity bins for the most central collisions(E_{rat} A). Spectra are fitted by a simple thermal blast model and the results are depicted by dotted lines. Starting with the uppermost rapidity bin(-0.1 $\sim$ -0.2), each spectrum is multiplied by a decreasing order of 10 for a clear display. Triangle and circle symbols denote data from the CDC and the Helitron in backward hemispheres in the center-of-mass, respectively.

E_{beam} (A GeV)	Particle Type	Centrality	T ($\lvert y^{(0)}\rvert \leq 0.1$) (MeV)	β_γ ($\lvert y^{(0)}\rvert \leq 0.1$)
0.4	Proton	E_{rat} A	38.4	0.32
		E_{rat} B	39.8	0.32
		E_{rat} C	39.7	0.30
		E_{rat} D	39.2	0.29
	Deuteron	E_{rat} A	49.1	0.26
		E_{rat} B	50.1	0.25
		E_{rat} C	48.7	0.24
		E_{rat} D	49.4	0.22
1.528	Proton	E_{rat} A	74.1	0.46
		E_{rat} B	81.0	0.43
		E_{rat} C	82.4	0.41
		E_{rat} D	84.0	0.36

Table 4.1: Fitting parameters of P_t spectra at the mid-rapidity for protons at both energies and deuteron at 0.4A GeV for different centrality selections. See the details in the text.

protons, deuterons, and Z=1(only for the most central case) ranges from 0.6 to 2.7. Based on the assumption to the isotropic source shape in the center-of-mass frame in the symmetric collision systems, the fitting parameters are meaningful only at the mid-rapidity($|y^{(0)}| \leq 0.1$). The fit parameters are summarized in Table 4.1 for protons at both energies and deuterons at 0.4A GeV(due to the limited acceptance of the CDC; deuterons at 1.528A GeV can not be measured properly). The fitting errors are less than 1% for both parameters for protons at both energies and deuterons at 0.4A GeV. For 0.4A GeV, the fitting values of T are independent of the collision centrality, but β_γ decreases systematically for peripheral collisions. For 1.528A GeV, T values increase, but β_γ decreases systematically for peripheral collisions. In contrast, both fitting values are much larger at 1.528A GeV than at 0.4A GeV. A similar finding is also available by already existing experimental data [39]. One can compare the present data with existing data. We observe that both T and β_γ values at 0.4A GeV are compatible with Au + Au collisions [44, 78] and that T at 1.528A GeV is close to that in Ni + Ni at 1.45A GeV [39]. However, β_γ

at 1.528A GeV is somewhat larger than existing data.

4.1.2 Rapidity Distributions

In order to construct the rapidity distributions($dN/dy^{(0)}$), the fit functions, which are equation 3.6 for $\pi^{\pm}$ at 1.528A GeV and equation 4.1 for others, of the invariant spectra of particles are integrated from 0 to ∞ in P_t to make up the missing P_t region. Figure 4.3 shows the rapidity distributions of protons and deuterons for four different centrality conditions in Ru + Ru collisions at 0.4A and 1.528 A GeV. One has to note that the mid-rapidity value of the $dN/dy^{(0)}$ distributions for deuterons at 1.528A GeV are not able to be measured due to the acceptance limit of the CDC, thus, we try to estimate them by extrapolation from neighboring points. These extrapolations with the second order polynomial function are indicated by solid lines in lower right panel of figure 4.3. In addition, the rapidity distributions of pions, protons, deuterons, and Z=1 baryons at 1.528A GeV for the most central collisions are compared in figure 4.4. The yields of particles at both energies are summarized in Table 4.2 at the end of this chapter.

The estimate of the systematic error affecting the overall normalization of the P_t integrated yields of the $dN/dy^{(0)}$ values of particles at both energies includes the following considerations:

(i) track quality cut including the particle identifications,

(ii) strategy for the Helitron momentum reconstruction (with and without including the event vertex),

(iii) the choice of the fit function by comparing the results obtained by equation 4.1 and a purely thermal Boltzmann function for baryon at both energies and by equation 3.6 and Boltzmann representations for pions at 1.528A GeV,

(iv) discrepancy between the CDC and the Helitron spectra in the overlapped phase-space region, and

(v) uncertainty in track reconstruction efficiency. The results of the systematic error estimation are summarized in Table 4.3 at the end of this

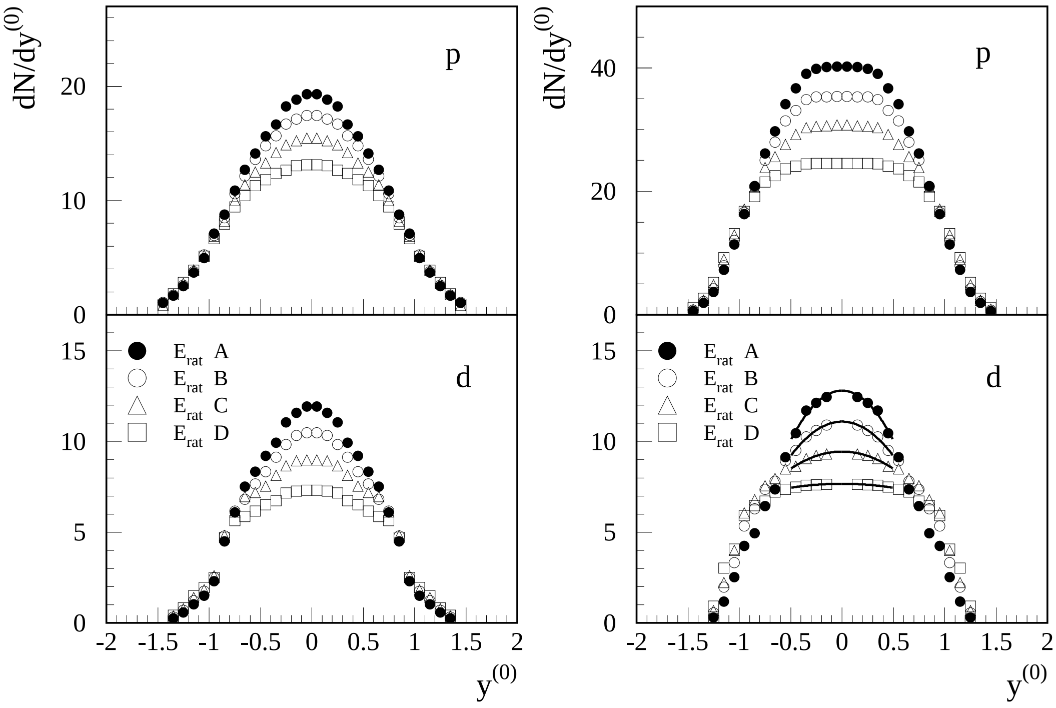

Figure 4.3: Centrality dependence of the proton and deuteron rapidity distributions for various centrality selections in Ru + Ru collisions at $0.4A$(left) and $1.528A$(right) GeV. Data points at backward hemisphere in the center-of-mass frame are measured while data points at forward hemisphere are reflected by the symmetry of the collision system.

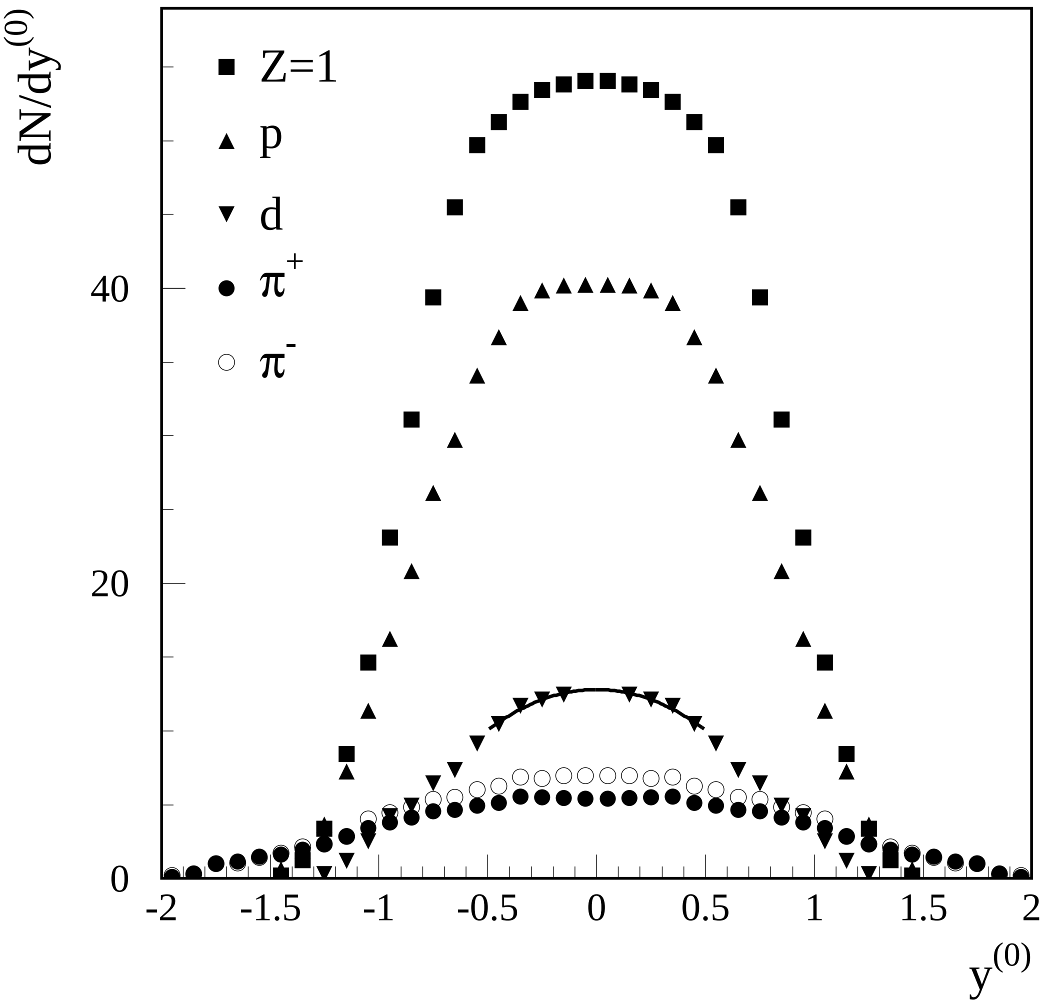

Figure 4.4: Rapidity distributions of various hadrons in Ru + Ru collisions at 1.528A GeV for the most central collisions.

chapter.

Since the fit function equation 4.1 and 3.6 do not account for possible low P_t spectator components near rapidity $y^{(0)}=\pm 1$, one can expect the tails of the rapidity distributions for noncentral collisions to be representative only for participant matter. As one can see in the acceptance plot of figure 2.15 and figure 3.13, low P_t parts of the the spectra near target/projectile rapidity, which is most likely to be populated by spectator fragments, are not covered in the isotope separated distributions. With use of the information from the PLAWA and the ZDD which allow only charge, but not isotope separation of fragments down to θ_{Lab}=1.2°, one can check that the fitting procedure is fully adequate for central collisions, and that the data in the range $|y^{(0)}| \leq 0.7$ are unaffected also for more peripheral collisions. To further confirm that the estimation by the extrapolation procedure over the full phase space is reasonable, the total charge of all the reaction products as checked to agree with the initial charge in the system(88 in Ru + Ru collisions) within 5% at 0.4A GeV [79] and slightly more than 7% at 1.528A GeV(Table 4.2) for central collisions.

The rapidity distributions in figure 4.3 show that protons and deuterons are concentrated more at the mid-rapidity for more central collisions. The ratio of deuteron and proton yields is about 54% at 0.4A GeV and 30% at 1.528A GeV in Ru + Ru collisions independent of centrality. The ratio of deuteron and proton yields at 0.4A GeV should be compared with about 72% estimated in Au + Au collisions at the same beam energy [44].

In experiments, the corona effect, which is caused by the surface nucleons of colliding nuclei passing through each other even in collisions with perfect geometrical overlap, can not be eliminated. This effect leads to some degree of transparency and it becomes important not at the mid-rapidity region but at the target and projectile rapidity regions [47]. We can measure a larger isolated spectator matter for more peripheral collisions. As a result, we can observe narrow peaks near projectile(or target) rapidity region in rapidity distributions for intermediate mass fragments(IMF) from spectator [80]. However, in this thesis, the spectator components in the rapidity distributions are not able to be separated in highly central collisions and partly due to the detector acceptance. In figure 4.3, more populations of protons and deuterons are found at $|y^{(0)}| > 0.7$ for more peripheral collisions and it is more pronounced at higher beam energy. It is not solved yet if this is due to the remnant of the spectator matter [81], or partial transparency [67], or simultaneous contribution by both of them.

For the most central collisions in Ru + Ru at 1.528A GeV, the rapidity distributions of different particles are compared (figure 4.4). The slightly different results are reported from different analysis, and this discrepancy is traced back to different efficiency estimation procedure [70] for pions and different biquadratic fitting for interpolations and extrapolations to fill complete 4π phase-space of charged particles [82]. However, all rapidity distributions and total yields are agree within at most about 10% uncertainty for pions and about 5% for other particles.

4.1.3 IQMD Comparison

For the most central collisions(E_{rat}) in Ru + Ru, the experimental measurements of the proton and deuteron rapidity distributions at 0.4A GeV and the proton and Z=1 baryon rapidity distributions at 1.528A GeV are compared with the results from the IQMD calculations as shown in figure 4.5. For 0.4A GeV, the IQMD calculations are for $b_{\mathrm{IQMD}} \leq 1$ fm with Hard Equation-of-State(H) including momentum dependence of the nucleon interaction(M). The total nucleon-nucleon(NN) cross section σ_{NN} are varied from $0.5\sigma_{NN}^{free}$ to $5\sigma_{NN}^{free}$ where σ_{NN}^{free} represents the total NN cross section in free space. The results are plotted in the left side of figure 4.5. For 1.528A GeV, the range of the impact parameter in the IQMD is $b_{\mathrm{IQMD}} \leq 2$ fm with both HM and SM options. Two values of σ_{NN}^{free} at 0.75 σ_{NN}^{free} and σ_{NN}^{free} are presented in the right side of figure 4.5.

In the IQMD transport approach, composite particles are produced by a coordinate space cluster algorithm. With default parameters, the algorithm starts to produce composite particles after 200 fm/c, and it is well known that too few composites are produced in the standard IQMD [44]. This problem in the IQMD is more pronounced at higher energy and more central collisions. Therefore, the comparison was performed only for the spectral shapes of protons, deuterons, and Z=1 baryons, but not the absolute yields of particles in the IQMD. All model calculations are normalized in such a way that the integration of the rapidity distributions is the same as in the data.

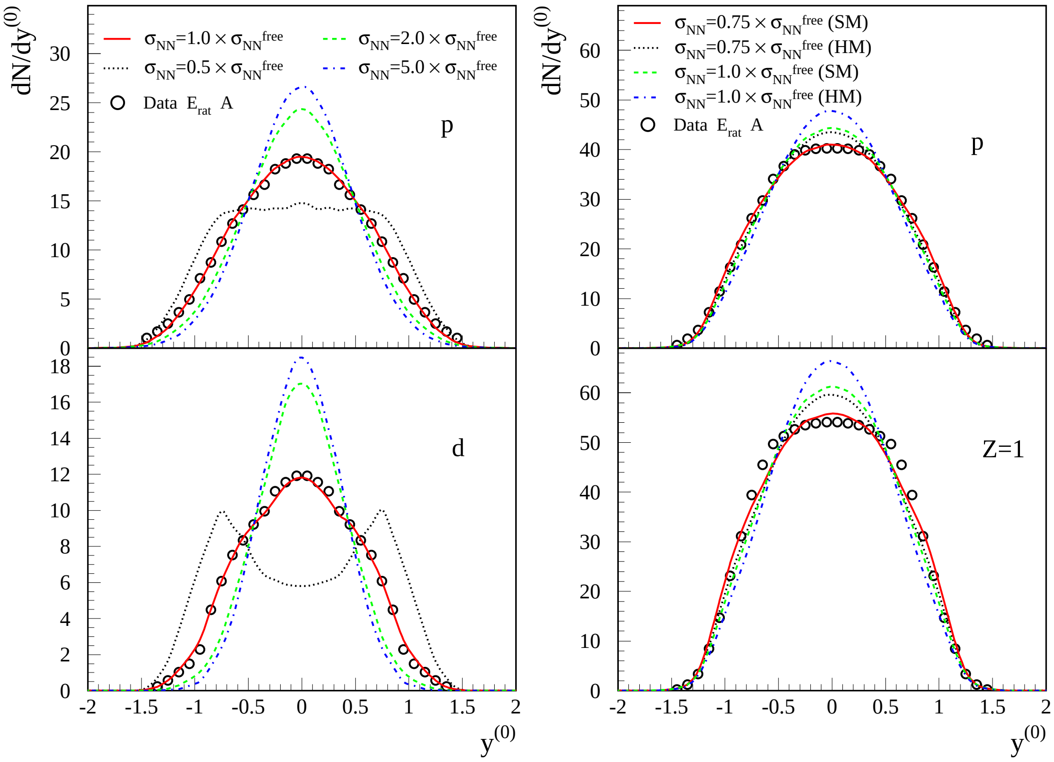

Figure 4.5: Comparison of the proton and deuteron rapidity distributions in Ru + Ru collisions at $0.4A$ GeV(left) and the proton and Z=1 baryon rapidity distributions in Ru + Ru collisions at $1.528A$ GeV(right) with the results from the IQMD calculations. Data are for E_{rat} A condition(open circles). The model calculations are for $b_{IQMD} \leq 1(2)$ fm at $0.4(1.528)A$ GeV. Only IQMD HM calculations with different values of σ_{NN} between $0.5\sigma_{NN}^{free}$ and $5\sigma_{NN}^{free}$ at $0.4A$ GeV are depicted by various lines. For $1.528A$ GeV, both IQMD HM and SM calculations combined with σ_{NN}=$0.75\sigma_{NN}^{free}$ and σ_{NN}^{free} are shown by various lines. See the text for more details.

At 0.4A GeV, the experimental proton and deuteron rapidity distributions agree well with the σ_{NN}=σ_{NN}^{free} assumption. Other σ_{NN}(s) which deviate more than 20% from σ_{NN}^{free} can be excluded. In hydrodynamics in nucleus-nucleus collisions, it is governed by the shock waves propagating in the beam direction [83]. Shock waves can be generated when the border of the stopped matter moves faster than the speed of sound in nuclear matter. In the prediction of an ideal hydrodynamics, shock waves would be generated in the early time of collisions, and the transverse expansion that the nuclear matter is pushed outwards perpendicular to the beam direction is expected. In the IQMD calculation, one can imitate ideal hydrodynamics by significantly increased σ_{NN} in the medium. In addition, transparency can be simulated by using a very small σ_{NN}. In left plot of figure 4.5, the most longitudinally elongated rapidity spectrum is generated for σ_{NN}=0.5 σ_{NN}^{free} whereas highly concentrated at the mid-rapidity spectrum due to transverse expansion is generated for σ_{NN}=5 σ_{NN}^{free}. In the later case, nuclear matter rebounds after instant equilibration mimicking the effects by the shock wave in hydrodynamics. These two extremes can be excluded by the comparison of the data with the IQMD calculations. For the model calculation with soft Equation-of-State, very similar proton rapidity distributions as that with HM option can be obtained.

At 1.528A GeV, the model calculations from both types(HM and SM) of Equation-of-State with σ_{NN}=σ_{NN}^{free} fail to describe experimental rapidity distributions of protons and Z=1 baryons, especially, at the mid-rapidity. By using σ_{NN}=0.75 σ_{NN}^{free} and SM, the model can reproduce data. But there is yet small difference between the data and model, especially for Z=1 baryons. The reasons why we look at Z=1 baryons instead of deuterons are (1) deuteron rapidity point at -0.1 $\leq$ y$^{(0)}$ $\leq$ 0.0 can only be extracted by extrapolation and (2) the problem of the cluster algorithm in the IQMD becomes larger at higher energy. Comparison between 0.4A and 1.528A GeV gives two important results: (1) soft Equation-of-State with momentum dependence of the nucleon interaction favors to describe the experimental data at 1.528A GeV and (2) a little bit reduced σ_{NN} is required to describe the data. As already mentioned in chapter 1, the IQMD predicts that transparency becomes more pronounced at higher beam energies [46], but the CBUU claims more stopping at higher beam energies up to 2A GeV [47]. The model comparison with the data at 0.4A and 1.528A gives that more transparency exists where beam energies become higher based on the framework of the IQMD and CBUU predictions. The change of the Equation-of-State with beam energies at the AGS energy regime was reported in Au + Au collisions [84], in which the BUU model calculations with hard Equation-of-State describe experimental data at low energies($E_{beam} \leq$ 2A GeV) and the model prefers to soft Equation-of-State at higher energies($E_{beam} \geq$ 4A GeV). The determination of the Equation-of-State in the nuclear matter at the SIS energy regime is still under debate and recent publications indicate that the model calculations with soft Equation-of-State can describe experimental data well [21, 85, 86, 87], which is along the same line as this analysis. However, all model calculations are sensitive on physics observables(*e.g.* flow and yield of kaons, etc.) and the choice of various model parameters(*e.g.* MDI, σ_{NN}, and the compressibility, etc.).

4.1.4 Mean Rapidity Shift

The mean rapidity shift (in some articles, called as the mean rapidity loss) has been used for quantification of the widths of the rapidity distributions in wide beam range from SIS to RHIC [39, 88, 89, 90]. It is defined by

$$\delta y_p \equiv \frac{\int_{-\infty(0)}^{0(\infty)} \mid y^{(0)} - y_{t(b)} \mid \left(dN/dy^{(0)}\right) dy^{(0)}}{\int_{-\infty(0)}^{0(\infty)} (dN/dy^{(0)})\, dy^{(0)}}, \tag{4.2}$$

where y_t and y_b represent target and beam rapidities, and $dN/dy^{(0)}$ is the proton rapidity distribution. In order to facilitate a detailed comparison between the measured rapidity shapes and those of model calculations, δy_p is used. The quantity δy_p reflects the inverse width of the rapidity distribution, thus, δy_p becomes larger for narrower rapidity distributions.

The experimental values of $\delta y_p/y_b$, which is the δy_p variable normalized by the beam rapidity, within four different centrality selections are summarized in Table 4.4 at the end of this chapter. Quantitatively, $\delta y_p/y_b$ decreases by about 2% and 4% for proton and deuteron at 0.4A GeV, respectively, by removing the autocorrelation effect. As expected in a transparency scenario, $\delta y_p/y_b$ is larger for more central collisions at both energies.

In Table 4.5 at the end of this chapter, the mean rapidity shifts of protons and deuterons normalized by the beam rapidity from the IQMD calculation are presented. The impact parameter ranges are selected by $b_{IQMD} \leq 1$ fm for 0.4A GeV and $b_{IQMD} \leq 2$ fm for 1.528A GeV, respectively. In addition, HM with various σ_{NN} assumption are only calculated for 0.4A GeV, and the calculations are performed with σ_{NN}=0.75σ_{NN}^{free} and σ_{NN}^{free} of both HM and SM options at 1.528A GeV. For both data and the IQMD calculations, larger value of $\delta y_p/y_b$ for deuterons than that for protons in a given centrality bin is obtained at 0.4A GeV (it is almost the same for 1.528A GeV, if deuteron $dN/dy^{(0)}$ at the mid-rapidity is included.).

Figure 4.6 and 4.7 are the illustration of the results of mean rapidity shifts. Data for 0.4A GeV shown in figure 4.6 are the weighted mean of the corresponding proton and deuteron $\delta y_p/y_b$ values, but those at 1.528A GeV shown in figure 4.7 are only for protons. For the most central collisions, the IQMD calculations with four different σ_{NN} values with HM mode at 0.4A GeV are given, and σ_{NN}=0.75σ_{NN}^{free} and σ_{NN}=σ_{NN}^{free} with both SM and HM modes are calculated at 1.528A GeV. In addition, the IQMD calculation with σ_{NN}=σ_{NN}^{free} is given in figure 4.6 at 0.4A GeV as a function of the centrality. For the most central collisions, the experimental data are reproduced by the assumption of the total nucleon-nucleon cross section in a dense and hot environment with σ_{NN}^{free} and HM mode at 0.4A GeV and with 0.75σ_{NN}^{free} and SM mode at 1.528A GeV. For 0.4A GeV results, there is a discrepancy in the centrality dependence of $\delta y_p/y_b$: as the impact parameter increases the IQMD calculations show a much faster drop of $\delta y_p/y_b$ than the data. If all $\delta y_p/y_b$ values for protons and deuterons at 1.528A GeV are treated by the same way as treated at 0.4A GeV, $\delta y_p/y_b$ in the corresponding centrality bin is almost the same as the result at 0.4A GeV.

In a reference [39], the systematics of the baryon rapidity losses(mean rapidity shifts) for central nucleus-nucleus collisions in beam energy from 1A to 200A GeV has been discussed. The important conclusion was that the mean rapidity shift δy_p of protons scaled with the beam rapidity y_b from 1A to 200A GeV. The weighted mean values of $\delta y_p/y_b$ for both protons and deuterons in Ru + Ru collisions are 0.267±0.011 at 0.4A and 0.264±0.011 at 1.528A GeV within E_{rat} A condition. These values are reasonably agreed with the average $\delta y_p/y_b$ value(0.28) of relatively small collision systems($A \leq 58$) from 1A to 200A GeV and it is about 15% smaller than that of Au + Au collisions at 11A GeV. From this comparison, one can conclude that

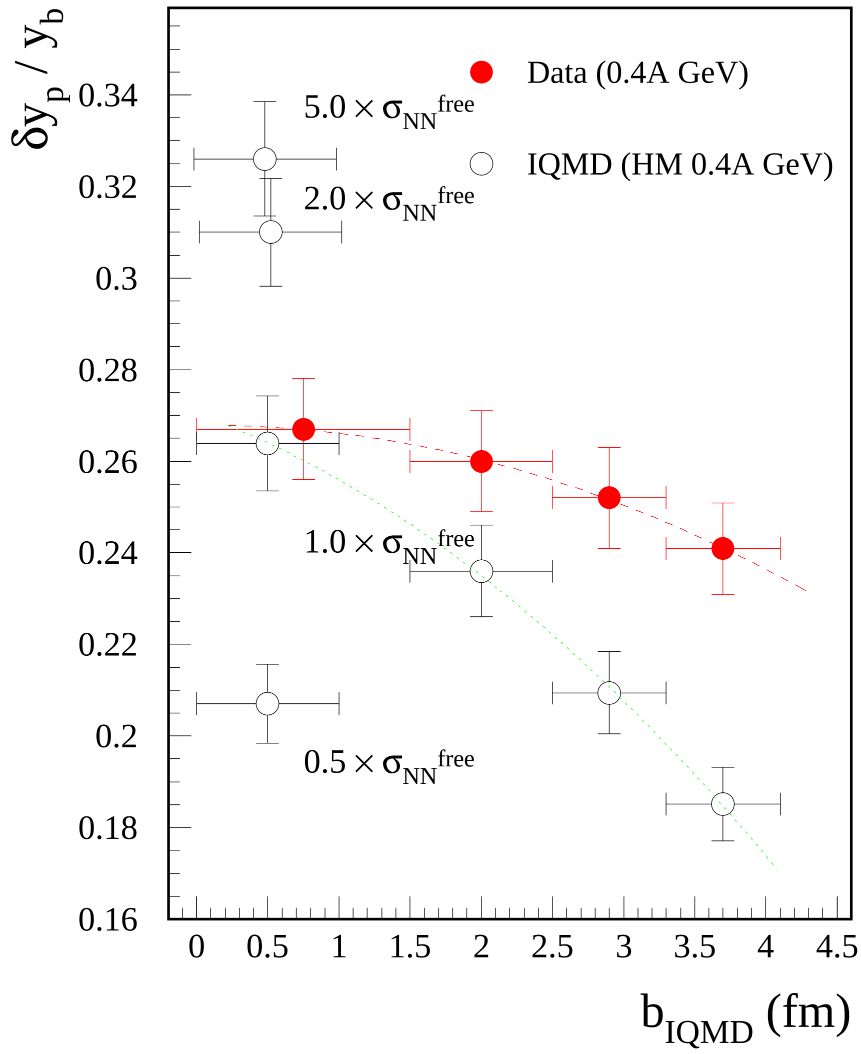

Figure 4.6: Mean rapidity shifts of protons normalized by the beam rapidity as a function of the impact parameter in Ru + Ru collisions at 0.4A GeV. For the experimental data, the values of $\delta y_p/y_b$ for various centrality selections are shown by closed circles. Each data point is the weighted mean of the corresponding proton and deuteron $\delta y_p/y_b$ values. The IQMD results are obtained by the HM with various assumptions on σ_{NN}. The lines are fitted by the second order polynomial function.

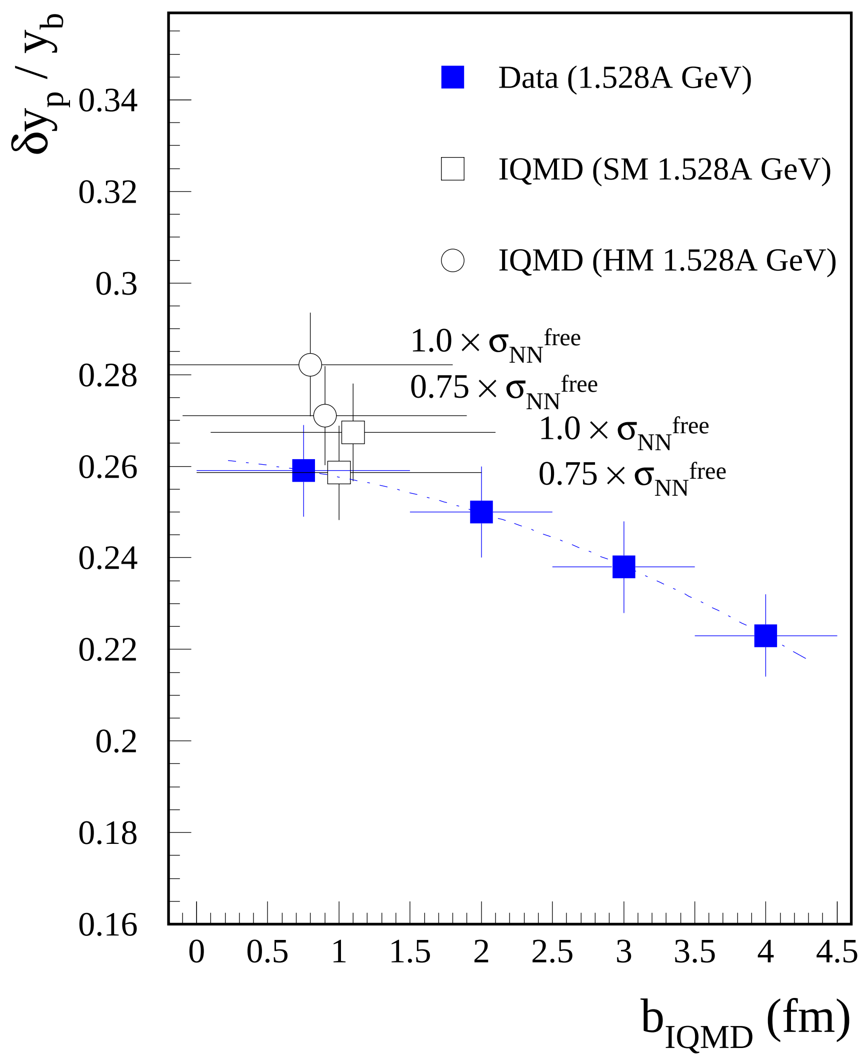

Figure 4.7: Mean rapidity shifts of protons normalized by the beam rapidity as a function of the impact parameter in Ru + Ru collisions at 1.528A GeV. For the experimental data, the values of $\delta y_p/y_b$ for various centrality selections are shown by closed squares. Each data point is proton $\delta y_p/y_b$ values only. The IQMD results are obtained by both HM and SM with assumptions on σ_{NN}=0.75σ_{NN}^{free} and σ_{NN}^{free} for the most central collisions. The line is fitted by the second order polynomial function.

the scaling law holds from $0.4A$ to $200A$ GeV and there is the system size dependence. The larger collision system shows a larger value of $\delta y_p/y_b$, which implies that more proton concentration of protons at the mid-rapidity can be expected for heavier system.

4.2 Analysis with Isospin Tracer Method

In previous section, the experimental data are presented in comparison with transport calculations, which evidences incomplete stopping in heavy-ion collisions at SIS energies. However, this physics interpretation is model dependent. In this section, two isospin tracer methods, which require only experimental data for nuclear stopping in heavy-ion collisions, are presented. In addition, the comparison of the data with the IQMD calculations is also given.

4.2.1 Isospin Tracer Method

The isospin tracer method is designed for extracting the direct experimental information on nonequilibrium in heavy-ion collisions without any model comparisons. It is, basically, using nuclei of the same mass but a different neutron-to-proton ratio, N/Z, as a tracer in order to attribute the measured nucleons either to the target or to the projectile components. Therefore, it is possible to extract separated rapidity distributions for target and projectile nucleons. Similar isospin(N/Z) equilibration study has been investigated at low energies [12, 13, 14, 91]. In the isospin experiment, two symmetric collision systems (Ru + Ru and Zr + Zr; one has to note that Ru has 10% more number of protons than Zr) can be used for the calibration reference. If one measures the yield of protons in a given momentum bin, higher proton yield in Ru + Ru than that in Zr + Zr collisions can be expected. Such measurements using identical target and projectile deliver calibration values of the yield of protons for Ru + Ru and Zr + Zr collisions in each observed rapidity bin. In case of a mixed reaction(Ru + Zr and Zr + Ru), the measured proton yield takes intermediate values between the calibration limits of Ru + Ru and Zr + Zr reactions. If the yield of protons in Ru + Zr collision is close to the value of Ru + Ru(Zr + Zr) collisions, it means that the given rapidity bin is populated predominantly from nucleons of the Ru projectile(or Zr target). In such a way, it is possible to trace back the relative abundance of target to projectile nucleons contributing to a given momentum or rapidity bin. It is also possible to use only isospin asymmetric systems without the calibration references. In this way, although the relative abundance of the projectile to the target nucleons can not be derived, the transparency or rebound effect can be obtained without invoking any model calculations with a smaller error.

The isospin tracer method gives several advantages.

(1) The ratios are insensitive to systematic uncertainties due to the apparatus, because all experiments have been done under identical conditions. The errors are essentially of statistical nature and profit from the high yield in the considered bin.

(2) The mixed reaction Zr + Ru is the same as Ru + Zr except that target and projectile are inverted. This allows forward-backward cross-check of the apparatus which in addition, can also be obtained from two symmetric collision systems.

(3) Using four reactions, the necessary full information can be obtained by measuring only backward or forward hemisphere in the center-of-mass frame.

Figure 4.8 is the summary of the expected results from the isospin tracer method, which will be explained details in the following sections, corresponding to three possible nuclear stopping scenarios. Nuclear stopping can be categorized into three classes which are rebound, full mixing, and transparency. If one measures the proton rapidity distributions for the mixed systems, the corresponding rapidity distributions to each class are expected at the third and fourth rows from the top in figure 4.8.

4.2.2 R_p

R_p is the ratio of rapidity distributions of two mixed systems (Ru + Zr and Zr + Ru) defined by the following formula:

$$R_p = \frac{dN/dy^{(0)}_{\mathrm{RuZr}}}{dN/dy^{(0)}_{\mathrm{ZrRu}}}. \tag{4.3}$$

It gives a clean signal about the nuclear stopping phenomenon via the sign of the slope near mid-rapidity. The ratio R_p will show different behavior as

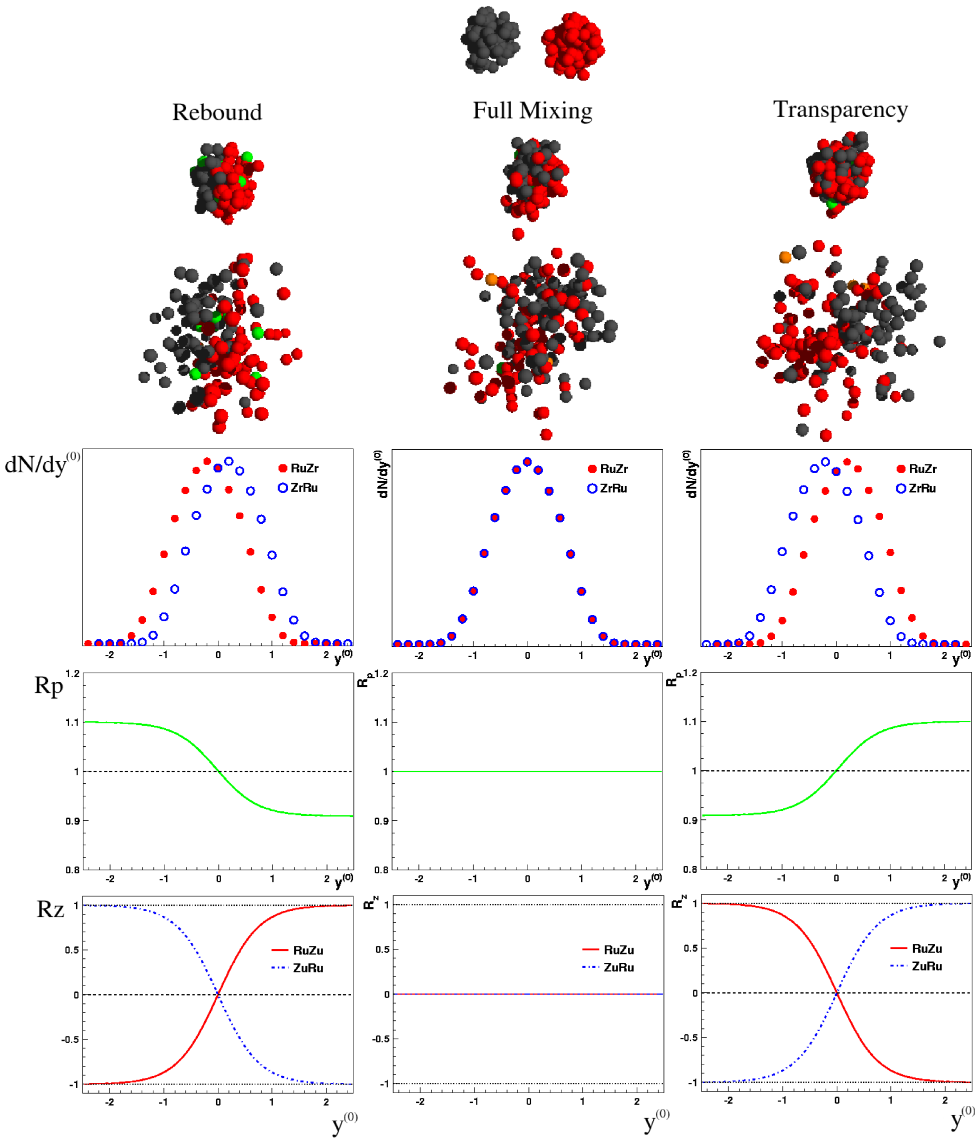

Figure 4.8: Three possible nuclear stopping scenarios. Each column shows different nuclear stopping scenario and the respective results of $dN/dy^{(0)}$ distributions of the projectile and target, R_p, and R_z. From the first to the third row are time span views in the center-of-mass frame before, the colliding moment, and after the collision. See the text for the details.

a function of rapidity for different nuclear stopping scenarios: R_p increases as a function of rapidity(positive slope) for transparency and decreases(negative slope) for rebound. If full mixing of isospin has been achieved in the collision, R_p as a function of rapidity is expected to be flat. These expected results can be seen at the fifth row in figure 4.8. In addition, R_p should be unity at the mid-rapidity($y^{(0)}$=0) due to the mass symmetry of the collision systems. It means that target and projectile nucleons should be admixed equal amounts in the center-of-mass.

Figure 4.9 shows the experimental results of R_p as a function of rapidity for protons in the CDC at 0.4A and 1.528A GeV for the most central collisions(E_{rat} A). Data points at the mid-rapidity at both energies are crossing unity, which satisfies the criterion mentioned above. R_p spectra at both energies show the positive slope, which confirms the transparency scenario. It is also consistent with the previous conclusion obtained from the comparisons of rapidity distributions between the data and the IQMD calculations. We find a stiffer R_p distribution at 1.528A GeV, which can be another evidence of more transparency effect at higher energies. Therefore, these positive slopes of R_p near the mid-rapidity at both energies give the conclusion about a partial bulk transparency of the target and projectile nuclei.

The ratio R_p is less prone to systematic errors than the rapidity distributions themselves because the ratio eliminates many systematic uncertainties due to an imperfect apparatus response. For 1.528A GeV, all systematic errors are estimated by varying cuts on the centrality selection range on E_{rat}, low momentum limit, and the mass window for the particle identification. Upper and lower limits of the systematic error for each data point are depicted by two horizontal lines around the data point. For 0.4A GeV, systematic errors are estimated similarly to the 1.528A GeV data, which are about 10% for all rapidity ranges.

In figure 4.10, the result for protons only and the result for the sum of protons and deuterons at 0.4A GeV are presented together [67]. Both results agree well each other, which tells that R_p is the robust observable to changes in the analysis. In addition, the agreement between the result for the sum of protons and deuterons and the result only for protons implies that the ratio R_p of both particles is very similar. The possible bias due to the pion production at this energy was investigated by the pion ratios for both

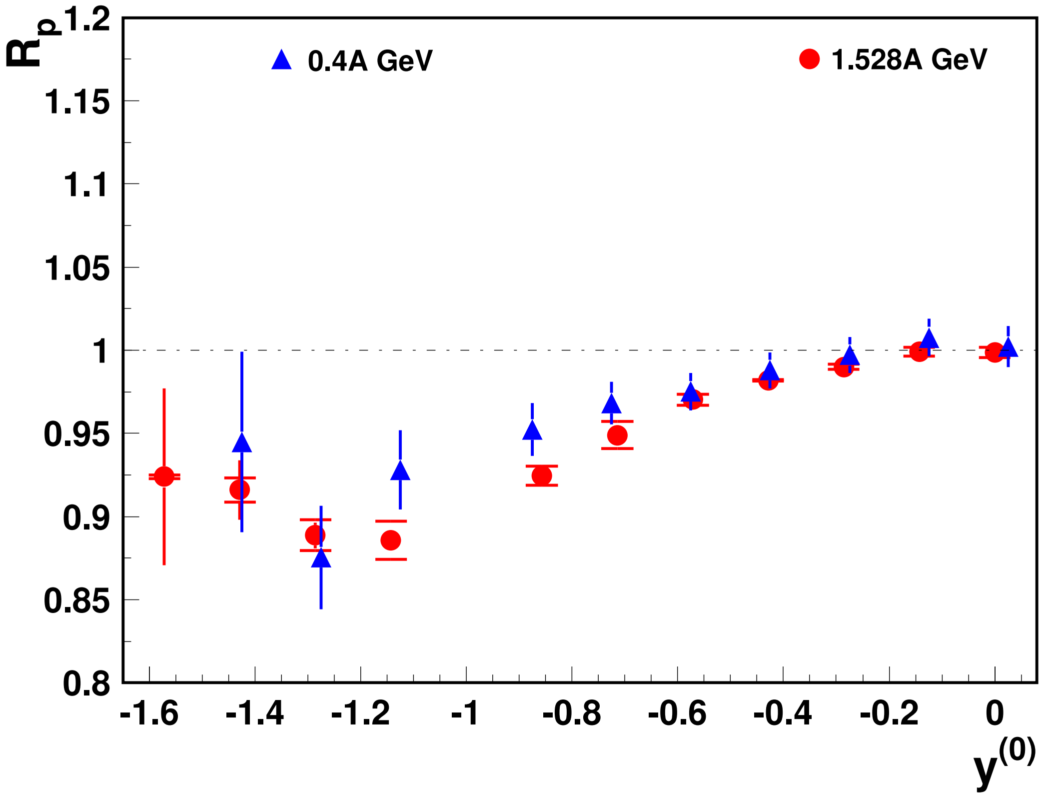

Figure 4.9: Experimental results of R_p as a function of rapidity for protons from the CDC at $0.4A$ (closed triangles) and at $1.528A$ (closed circles) GeV for the most central collisions(E_{rat} A). Error bars at $0.4A$ GeV contains both statistical and systematic(∼10%) errors. At $1.528A$ GeV, vertical line at each data point indicates the statistical error, where horizontal lines at each data point displays estimated upper and lower limits of the systematic error. See the text for more details.

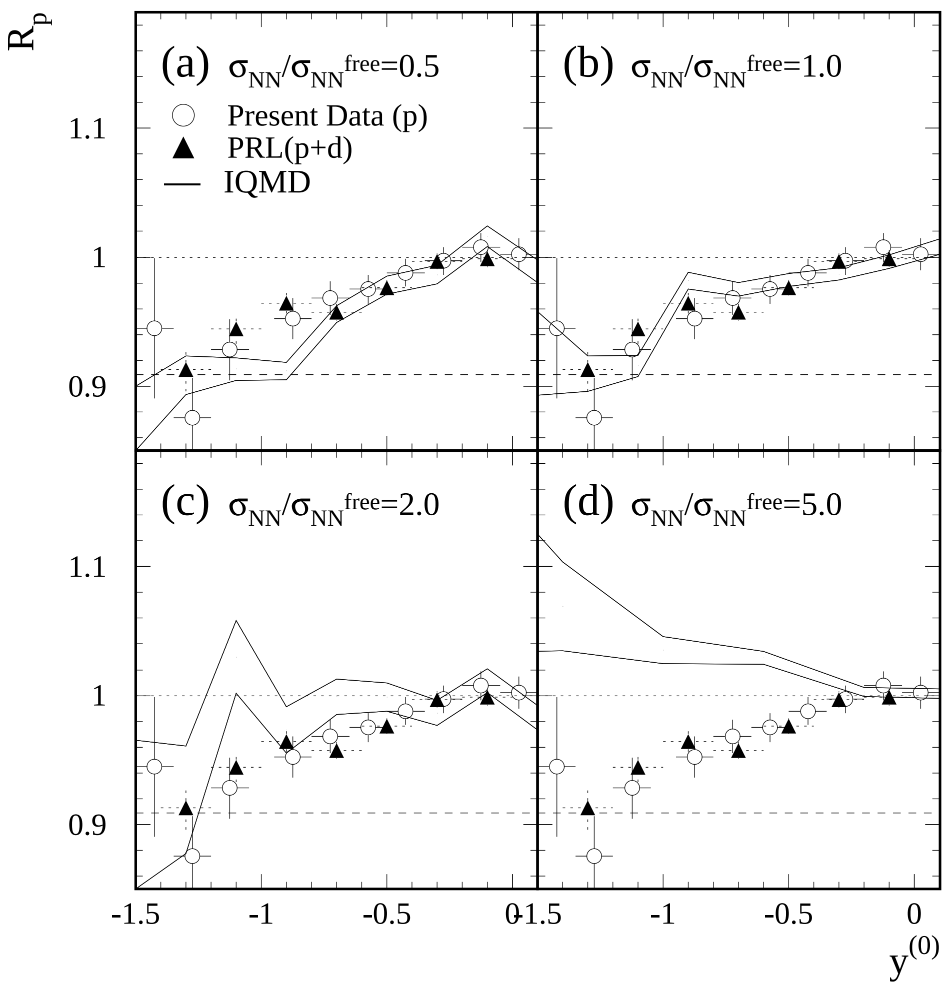

Figure 4.10: Comparison of R_p between the data and the IQMD calculations with various σ_{NN} assumptions in HM mode at $0.4A$ GeV. Experimental data points are from the CDC under E_{rat} A criterion. Open circles are for the present experimental data and solid triangles are for proton like particles(p+d) from reference [67]. For the IQMD calculations, the nucleon-nucleon cross section σ_{NN} was assumed to be 0.5(a), 1.0(b), 2.0(c), and 5.0(d) times σ_{NN}^{free}. The results of the model calculations are depicted by solid line. The dashed line represents the lower limit of R_p determined by the N/Z ratio of projectile and target nuclei, if R_p were to include all protons, bound or not.

charges. Within the statistical errors, the R_p ratio of π^-/π^+ is unity and no signature of finite slope is found. The IQMD calculations have been done for the most central collisions ($b_{IQMD} \leq 1$ fm). For these model calculations, the geometrical detector filtering has been applied. However, this filtering has almost negligible effect since the analysis relies on a relative quantity. The comparison of the experimental R_p result with the IQMD calculations in figure 4.10 shows that the results of the IQMD calculations with σ_{NN}=0.5 σ_{NN}^{free} and σ_{NN}=σ_{NN}^{free} agree well with the data near mid-rapidity($|y^{(0)}| \leq 0.5$) which is the most interesting region for the nuclear stopping phenomenon. However, one can exclude the possibility of σ_{NN}=0.5σ_{NN}^{free} because it could not reproduce the experimental proton and deuteron rapidity distributions as explained in the previous section. The model calculation predicts that the isospin equilibrium can be achieved, if σ_{NN} becomes close to $2\sigma_{NN}^{free}$. There will be a rebound effect for σ_{NN}=5 σ_{NN}^{free} as the finite slope of R_p shows negative values at 0.4A GeV.

The comparison of the data with the IQMD calculations at 1.528A GeV is given in figure 4.11. All model calculations have been obtained with $b_{IQMD} \leq 2$ fm in 4π phase-space. We use the full phase-space yield without filtering by the detector geometry since such a process has negligible effect. We have increased the statistics of the simulation data by the reflection of the backward and forward hemispheres in the center-of-mass for Ru + Ru and Zr + Zr collisions. Similarly, the inversion of the target and projectile nucleons relative to the center-of-mass for Ru + Zr and Zr + Ru collisions were performed. In figure 4.11, two different σ_{NN} assumptions, which are σ_{NN}=σ_{NN}^{free} and σ_{NN}=0.75 σ_{NN}^{free}, with both HM and SM modes have been used for the model calculations. This comparison shows that its overall slopes of the IQMD calculations in the backward hemisphere rapidity range agree with the data for σ_{NN}=0.75 σ_{NN}^{free} for both HM and SM modes. Here, one has to note that the comparison to the experimental proton rapidity distribution in the previous section has the sensitivity of the Equation-of-State only near the mid-rapidity region(figure 4.5). Therefore, one can not exclude either HM or SM mode from this R_p comparison because it is almost the same for both HM and SM modes near the mid-rapidity in the IQMD calculations.

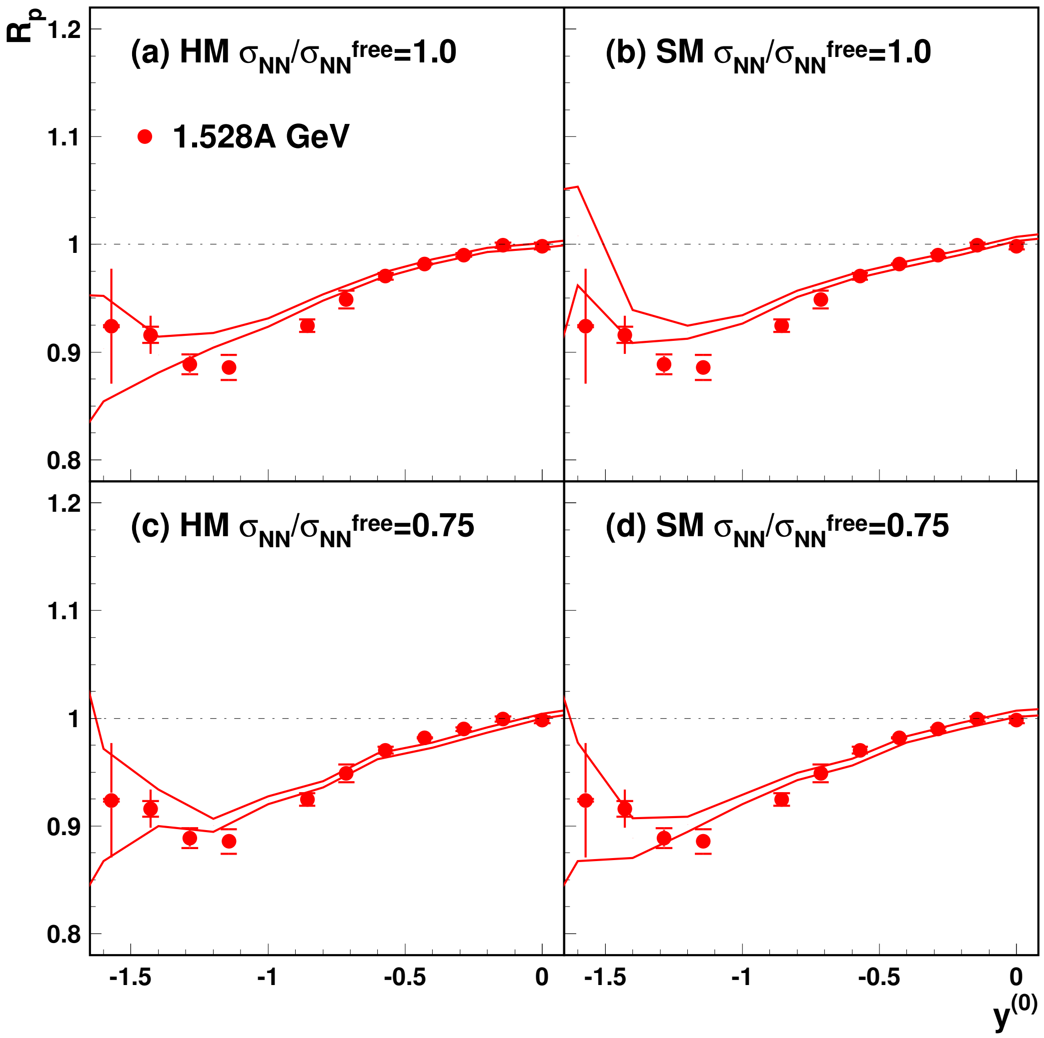

Figure 4.11: Comparison of R_p between the data and the IQMD calculations at 1.528A GeV. Experimental data points are for protons only from the CDC under E_{rat} A criterion. For the IQMD calculations, the nucleon-nucleon cross section σ_{NN} was assumed to be 1.0 with the HM(a) and the SM(b) options and 0.75 times σ_{NN}^{free} with the HM(c) and the SM(d) options. The results of the model calculations are depicted by solid line.

4.2.3 R_z

The ratio R_z is based on the combination of four systems(two symmetry Ru + Ru and Zr + Zr collisions, and two mixed Ru + Zr and Zr + Ru collisions). It is defined by the following formula:

$$R_z = \frac{2 \cdot dN/dy^{(0)}_{mix} - dN/dy^{(0)}_{ZrZr} - dN/dy^{(0)}_{RuRu}}{dN/dy^{(0)}_{ZrZr} - dN/dy^{(0)}_{RuRu}}, \tag{4.4}$$

where *mix* can be either RuZr or ZrRu collision system. In order to estimate the degree of nonequilibrium(or nuclear transparency) by the ratio R_z, both symmetric systems are used for calibrating level arms. For example, the ratio R_z becomes +1 for Zr + Zr and -1 for Ru + Ru collisions. If the nuclear stopping is incomplete, the value of R_z will be intermediate between -1 and +1 for the mixed system. In addition, it will be equal to 0 in case of full isospin equilibrium in a mixed system.

The experimental R_z results as a function of rapidity for protons at $0.4A$ and $1.528A$ GeV for the most central collisions(E_{rat} A) are shown in figure 4.12. One can see that the result of R_z is consistent with the transparency in figure 4.8. One has to point out that all data points at the mid-rapidity($y^{(0)}$=0) is 0 which is a very important consistency check. In figure 4.11, for a given rapidity bin, the signs of the R_z values are opposite in isospin asymmetric Ru + Zr and Zr + Ru collisions. The magnitudes of the R_z for Ru + Zr and Zr + Ru collisions agree each other within the quoted errors for the same energy. The data points below the target rapidity region at $1.528A$ GeV has been omitted because of huge systematic fluctuations and large statistical errors. The R_z values below $y^{(0)}$ = -0.5 dramatically increases at $1.528A$ GeV, and the absolute magnitudes are much larger than the values at $0.4A$ GeV. This large deviation can be caused by the larger transparency effect expected at higher energy. In reference [67], the centrality dependence of R_z for proton was investigated at $0.4A$ GeV. In this analysis, nonequilibrium of isospin was conjectured for the most central collisions, even b_{geo} approaches to 0 and nonequilibrium effect becomes more pronounce for peripheral than for central collisions.

The model comparison with the data is shown in figure 4.13 and all IQMD calculations are under the same conditions for σ_{NN} and the nuclear

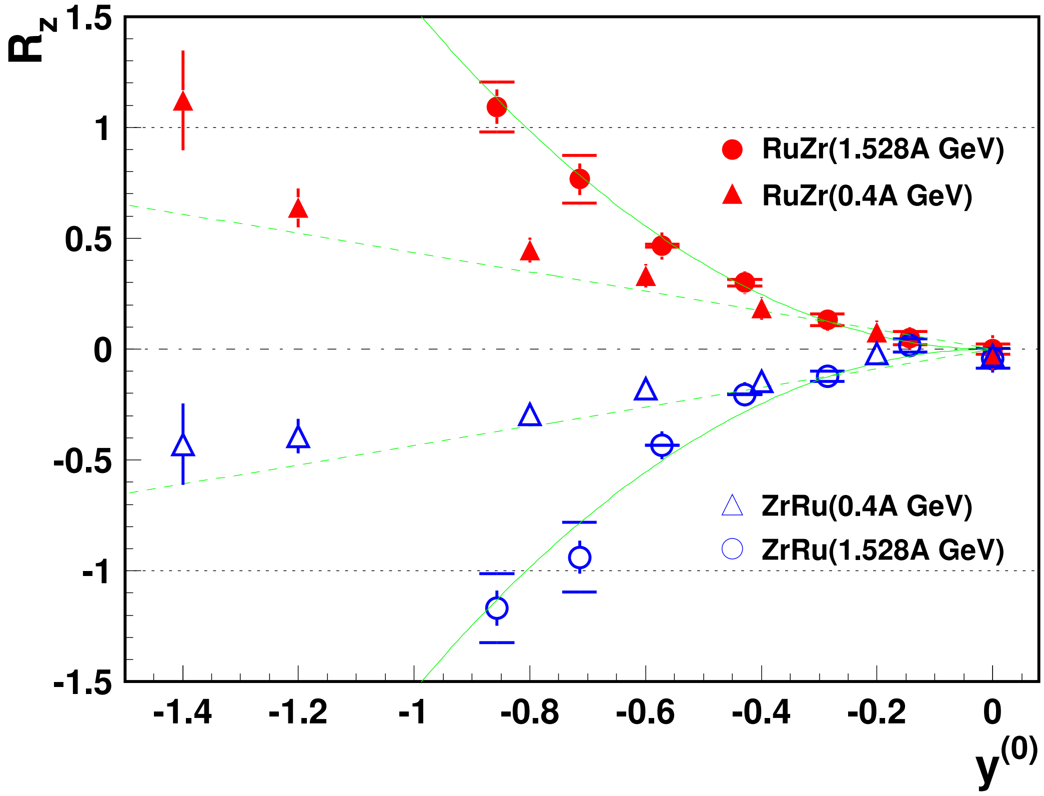

Figure 4.12: Experimental results of R_z as a function of rapidity for protons from the CDC at $0.4A$(triangles) and $1.528A$(circles) GeV for the most central collisions (E_{rat} A). The results for Ru + Zr (Zr + Ru) collisions are depicted by closed (open) symbols. Error bars at $0.4A$ GeV contain both statistical and systematic($\sim$10%) errors. At $1.528A$ GeV, vertical line at each data point indicates statistical error, and the horizontal lines at each data point display the estimated upper and, respective, lower limits of the systematic error. The solid (for $1.528A$ GeV) and dashed (for $0.4A$ GeV) lines are the fit results for deconvoluting the overall measured proton rapidity distributions into projectile and target components in Ru + Ru collisions. See the text for more details.

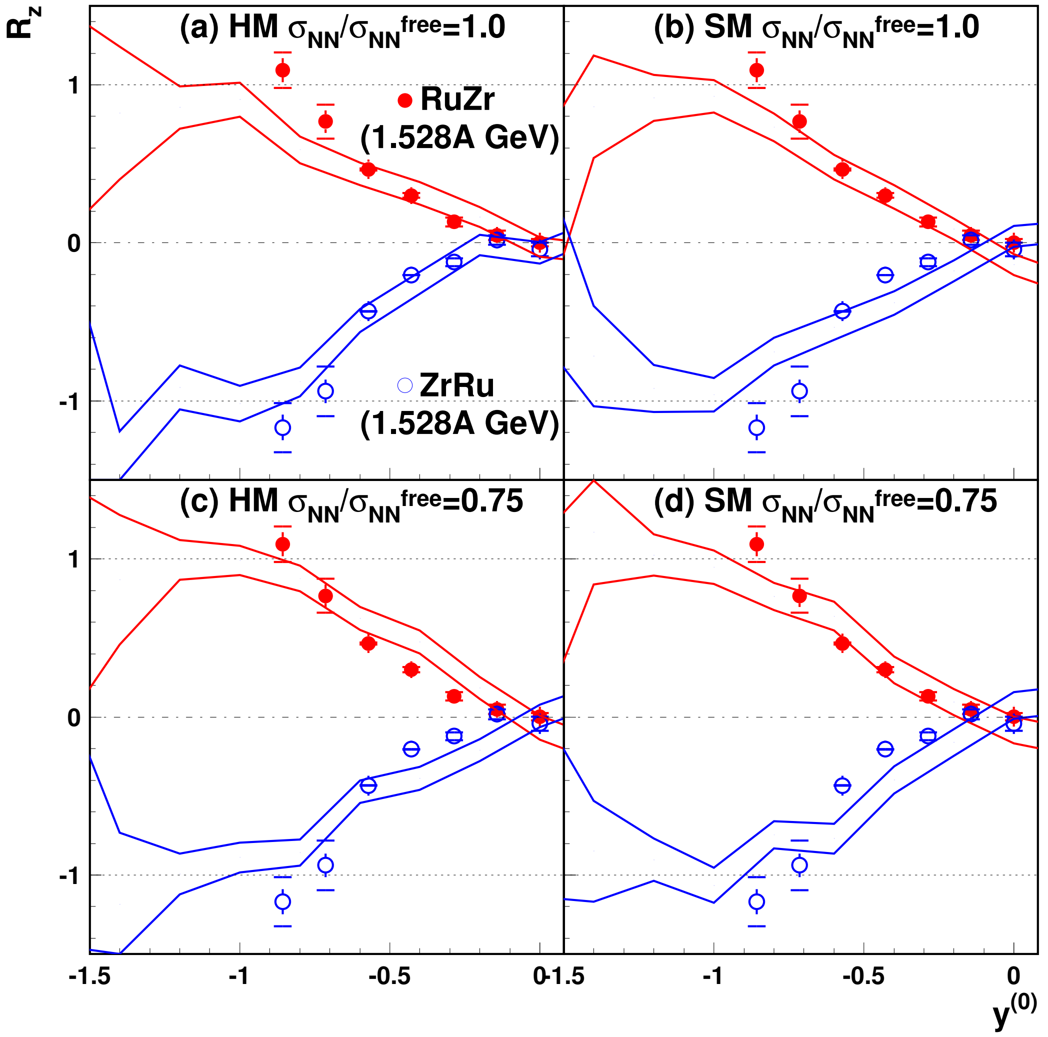

Figure 4.13: Comparison of the measured R_z with the IQMD calculations at 1.528A GeV. Experimental data points for protons are from the CDC under E_{rat} A criterion. For the IQMD calculations, the nucleon-nucleon cross section σ_{NN} was assumed to be 1.0 with the HM(a) and the SM(b) Equation-of-State, and 0.75 times σ_{NN}^{free} with HM(c) and SM(d) Equation-of-State. The result of the model calculations is depicted by solid lines.

Equation-of-State as a R_p case. For the results from Ru + Zr collisions, the model calculations of SM mode with both σ_{NN} assumptions agree well with the data. However, the comparison between the data and the IQMD calculation for Zr + Ru collisions only agree well with σ_{NN}=σ_{NN}^{free} under HM mode case. Here, recall that the results from the comparison to the experimental proton rapidity distributions in previous section. The determination of Equation-of-State has the sensitivity only near the mid-rapidity and the model calculation with SM and σ_{NN}=0.75σ_{NN}^{free} agree with data. In R_p, results from the model calculations do not have the sensitivity near the mid-rapidity, but show some difference below target rapidity region at 1.528A GeV. The comparison of R_z looks similar to the R_p case. If one considers only the mid-rapidity region, all model calculations are within the errors. Therefore, one can not make any conclusion from the comparison of R_z between the data and the model calculations.

Various theoretical models for isospin mixing predict contradictory nuclear stopping phenomena. For example, the IQMD model which considers isospin degrees of freedom into σ_{NN} as well as Coulomb interactions predicts transparency in ^{50}Cr on ^{48}Ca collisions from 0.15A to 1.5A GeV. This model also predicts that the transparency becomes more pronounced at higher beam energies, and that the degree of nuclear stopping(or isospin equilibrium) depends on σ_{NN} to a large extent. The sensitivity of the isospin asymmetry on σ_{NN} has been demonstrated by showing a transition from transparency to rebound as σ_{NN} increases by a factor of 5 in the IQMD [46]. On the other hand, Hombach *et al.* [47] claimed that there is more stopping at higher beam energies up to 2A GeV within the framework of the coupled-channel Boltzmann-Uehling-Uhlenbeck(CBUU) model. In this model, they predicted the result of the isospin experiment at FOPI, and claiming that the degree of nuclear stopping is more sensitive to the compressibility of the Equation-of-State than to σ_{NN} at 0.4A GeV. However, for 1.528A GeV, the situation is just reverse, which means that the degree of nuclear stopping is more sensitive to σ_{NN} than to the compressibility of the Equation-of-State. In addition, they pointed out that one has to take into account the shift of the total baryonic isospin due to the charged pion production at 1.5A GeV. Therefore, in this thesis, in order to estimate the effect of shift in total baryonic isospin due to the charged pion production, total charge of Ru + Ru system has been estimated(see section 4.1.2) and the measured total charge in Ru + Ru system at 1.528A GeV agrees with the initial charge in the system within 7 - 12 %.

In the reference [67], the ratio of t/^{3}He at 0.4A GeV was investigated by the isospin tracer method. At 1.528A GeV, yields of tritium and ^{3}He are very low and the isospin tracer method can not apply to the ratio of t/^{3}He. However, it is well known that the ratio of π^-/π^+ in heavy-ion collisions depends strongly on the isospin asymmetry of the reaction system [1, 18, 71, 92, 93]. Therefore, the ratio of π^-/π^+ was investigated at 1.528A GeV by using the isospin tracer method in order to study of the effect of the shift in total baryonic isospin due to the pion production as well as pion propagation in the nuclear medium. The results of R_p and R_z for π^-/π^+ ratio in the CDC acceptance by the IQMD calculations are shown in figure 4.14 and 4.15, respectively. The centrality selection in figure 4.14 and 4.15 is 10% of total geometrical cross section($\sigma_{geo} \sim 380$ mb) for the data and the IQMD calculations($b_{IQMD} \leq 2$ fm). The systematic errors are estimated by varying cut conditions on the centrality selection range, low and high momentum limits, and the mass range of the particle identification. In addition to the systematic error estimation, the deviation of π^-/π^+ ratios from the raw and the constructed rapidity distributions(see section 4.1.2 for the details of the method) for π^- and π^+ in Ru + Ru collisions are investigated. The lower and upper limits of the estimated systematic error in the corresponding rapidity bin are depicted by horizontal lines at each data point.

The slope of R_p for π^-/π^+ ratio in figure 4.14 shows opposite sign to the proton one, which is understandable as the π^-/π^+ ratio is the charge inversed reaction. The finite slope of R_p for π^-/π^+ ratio can be an evidence of transparency in nuclear stopping phenomenon but the magnitude is much smaller than the proton case. The comparison with the model calculations shows that all four different model assumptions can explain the data within their errors. The result of R_z for the π^-/π^+ ratio in figure 4.15 shows a similar trend as the proton case, which can also be an evidence of the transparency scenario. But the signal of R_z is much weaker than the proton result. All IQMD calculations agree with data points, which enable us to conclude that there is no sensitivity to distinguish different Equation-of-State and σ_{NN} values with R_p and R_z by using the π^-/π^+ ratio. The small finite slopes of R_p and R_z for the π^-/π^+ ratio is generated by the decay of the Δ baryonic resonance, which is the main source of the pion production at this energy [94]. Note that the

Δ baryons are propagating as protons in the nuclear medium and this effect partially transfers into their daughter particles(pions). Therefore, the π^-/π^+ ratio can reflect the transparency of the Δ baryons. We can conclude that R_p and R_z for the π^-/π^+ ratio prove the transparency scenario of the nuclear stopping phenomena.

4.2.4 Decomposition of Rapidity Distribution

In figure 4.12, the solid and dashed lines describe an average of measured R_z from the simultaneous fitting of both isospin asymmetric systems with inverted overall sign at 0.4A and 1.528A GeV, respectively. The fit functions are $|R_z|$=0.435$\cdot y^{(0)}$(solid lines at 0.4A GeV) and $|R_z|$=1.538$\cdot y^{(0)2}$(dashed lines at 1.528A GeV), where R_z has positive slope for Zr + Ru collisions and vice versa for Ru + Zr collisions. These fit functions can be used to deconvolute the overall measured rapidity distributions of protons in Ru + Ru collisions into the target and projectile nucleon components. For each rapidity bin, the numbers of projectile and target nucleons can be obtained by

$$\frac{dN}{dy^{(0)}}\,|_{\mathrm{projectile(target)}}=\frac{1}{2}\left[1\pm\mid R_z(y^{(0)})\mid\right]\cdot\frac{dN}{dy^{(0)}}, \tag{4.5}$$

where "+" is for projectile and "-" is for target components. By the definition, R_z can not be larger(or smaller) than +1(-1). However, sometimes, especially at large rapidity region, the mean value of $|R_z|$ can be larger than 1 due to small statistics and large systematic errors. In this case, the R_z value is set to be +1(-1) for the decomposition of $dN/dy^{(0)}$.

The results of the decomposition of the proton rapidity distributions at 0.4A and 1.528A GeV are shown in figure 4.16. After deconvolution a shift between two deduced rapidity distributions emerge, clearly demonstrating that a memory of the initial target/projectile motion survives in the course of central collisions. This incomplete mixing of nucleons is more pronounced at 1.528A GeV.

The separated projectile(or target) rapidity distribution can be readily parameterized into the nuclear mixing parameter M_{pr} defined by

$$M_{pr}=\frac{(N_f-N_b)}{(N_f+N_b)}, \tag{4.6}$$

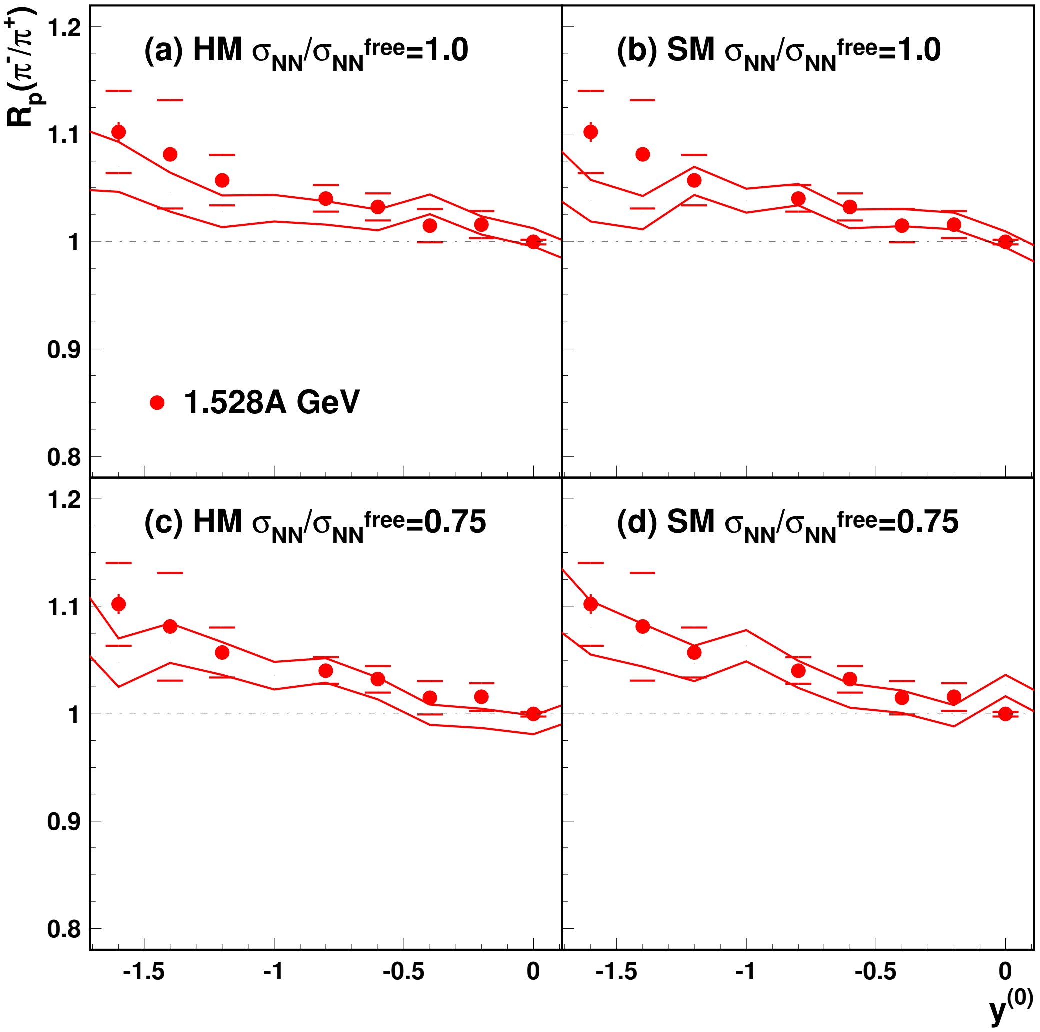

Figure 4.14: Comparison of the experimental R_p of π^-/π^+ with the IQMD calculations at 1.528A GeV. Experimental data points are from the CDC for the 10% most central centrality. For the IQMD calculations, the nucleon-nucleon cross section σ_{NN} was assumed to be 1.0 with the HM(a) and the SM(b) Equation-of-State, and 0.75 times σ_{NN}^{free} with the HM(c) and the SM(d) Equation-of-State. The results of the model calculations are depicted by solid lines.

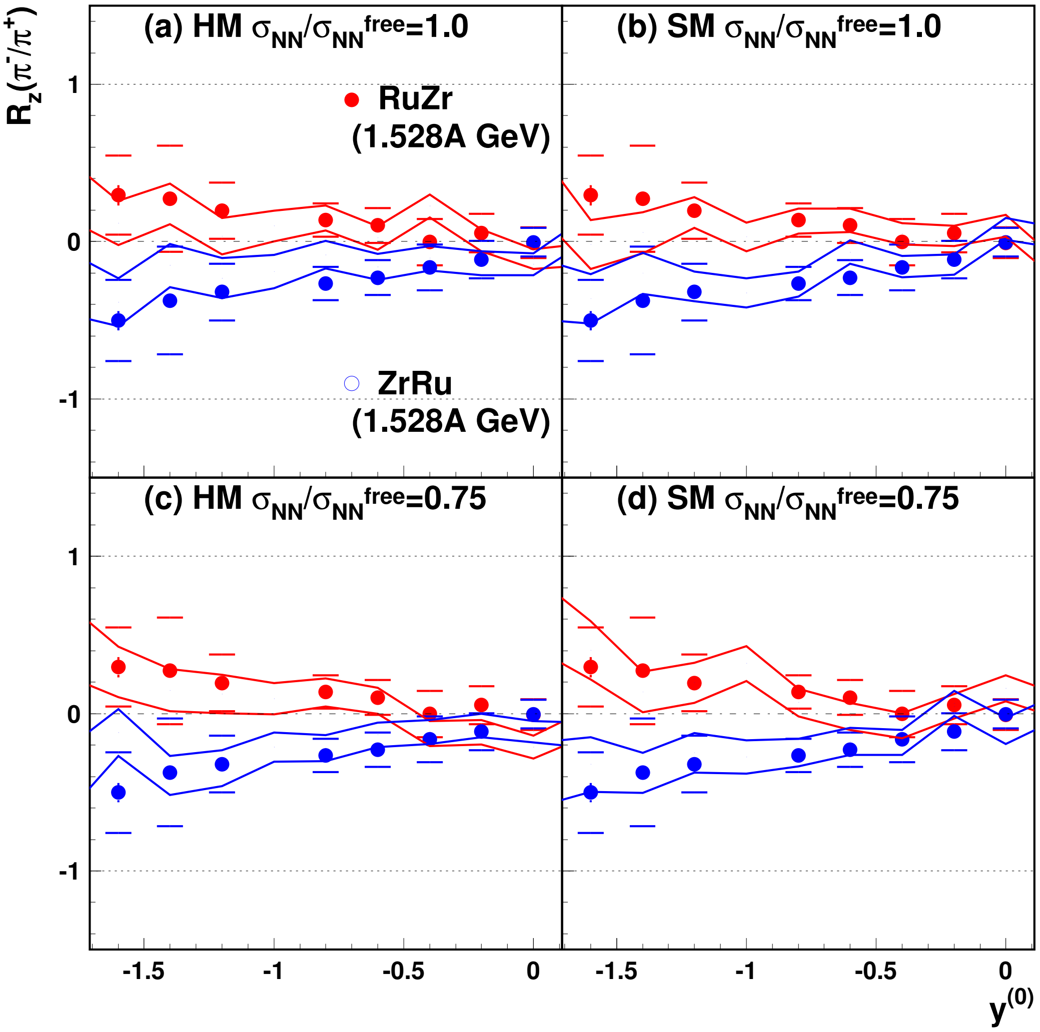

Figure 4.15: Comparison of the experimental R_z of π^-/π^+ with the IQMD calculations at 1.528A GeV. Experimental data points are from the CDC for the 10% most central centrality. For the IQMD calculations, the nucleon-nucleon cross section σ_{NN} was assumed to be 1.0 with the HM(a) and the SM(b) Equation-of-State, and 0.75 times σ_{NN}^{free} with the HM(c) and the SM(d) Equation-of-State. The results of the model calculations are depicted by solid lines.

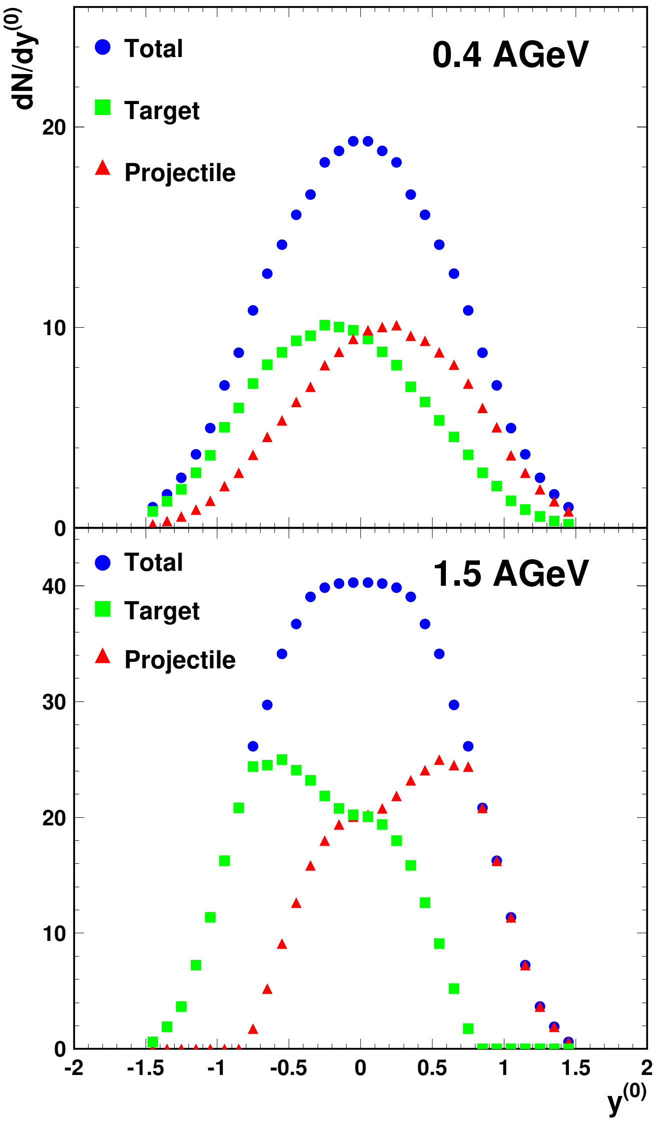

Figure 4.16: Decomposed proton rapidity distributions at $0.4A$(top) and $1.528A$(bottom) GeV. The measured overall proton rapidity distributions for the most central collisions(E_{rat} A) are depicted by closed circles. The target(squares) and projectile(triangles) components of protons are determined by the unfolding procedure described in the text.

where N_f is the number of projectile nucleons emitted in forward and N_b is that in backward hemisphere in the center-of-mass. M_{pr} is a measure of noneqilibrium effect and should be larger if nuclei are more transparent. The values of $\delta y_p/y_b$, N_f, N_b, and M_{pr} are summarized in Table 4.6 at the end of this chapter. The value of $\delta y_p/y_b$ for protons is larger at 1.528A GeV than at 0.4A GeV but agrees within the quoted errors. M_{pr} from the present analysis can be compared with the value in reference [67]. The present value is somewhat larger than the value in reference [67], and the difference can be deduced from the fact that the present result is for protons only while the result in reference [67] is for protons and deuterons. The comparison of the data with the IQMD calculations in reference [67] conforms the previous conclusion in this thesis, that hard Equation-of-State with $\sigma_{NN}=\sigma_{NN}^{free}$ can be reproduced by the present analysis at 0.4A GeV. M_{pr} at 1.528A GeV is about a factor of two larger than that at 0.4A GeV. Therefore, one can conclude that the degree of nuclear transparency at 1.528A GeV is order of two higher than that at 0.4A GeV.

E_{beam} (A GeV)	Particle Type	Centrality	Total yield
0.4	Proton	E_{rat} A	31.2
		E_{rat} B	29.6
		E_{rat} C	27.2
		E_{rat} D	24.6
	Deuteron	E_{rat} A	17.2
		E_{rat} B	16.0
		E_{rat} C	14.8
		E_{rat} D	13.0
1.528	Proton	E_{rat} A	69.6
		E_{rat} B	64.6
		E_{rat} C	59.2
		E_{rat} D	51.4
	Deuteron	E_{rat} A	19.2
		E_{rat} B	18.8
		E_{rat} C	17.8
		E_{rat} D	16.0
	Z=1 Baryon	E_{rat} A	96.4
	π^+	E_{rat} A	13.0
	π^-	E_{rat} A	15.4

Table 4.2: Total yields of particles in Ru + Ru collisions at $0.4A$ and $1.528A$ GeV. Yields of protons and deuterons are estimated in various centrality selections at both energies. Yields of pions and Z=1 baryons are estimated only for the most central collisions at $1.528A$ GeV. Estimated $dN/dy^{(0)}$ values for deuterons at $1.528A$ GeV are obtained by an extrapolation of the second order polynomial fit functions.

	0.4A GeV		1.528A GeV			
Particle	p	d	p	d	Z=1	$\pi^{\pm}$
(i)	3%	3%	3%	3%	3%	3%
(ii)	2%	2%	2%	2%	2%	
(iii)	3%	3%	3%	3%	3%	3%
(iv)	5%	5%				
(v)	5%	9%	7%	11%	7%	10%
total	9%	11%	8%	12%	8%	11%

Table 4.3: Estimated systematic errors of the overall normalization of the P_t integrated yields of the $dN/dy^{(0)}$ values of particles in Ru + Ru collisions at 0.4A and 1.528A GeV. The considerations of the errors((i) $\sim$ (v)) are described in the section 4.1.2. Total systematic errors are calculated by the quadratic sum of all errors. Pions in the Helitron can not be resolved by the detector limit(see section 3.2.2 for more details). There is no overlap between the CDC and the Helitron at higher energy(see section 4.1.1 for more details).

E_{beam} (A GeV)	Particle Type	Centrality	$\delta y_p/y_b$
0.4	Proton	E_{rat} A	0.256±0.011
		E_{rat} B	0.250±0.011
		E_{rat} C	0.244±0.010
		E_{rat} D	0.234±0.010
	Deuteron	E_{rat} A	0.287±0.012
		E_{rat} B	0.277±0.011
		E_{rat} C	0.266±0.011
		E_{rat} D	0.254±0.010
1.528	Proton	E_{rat} A	0.259±0.010
		E_{rat} B	0.250±0.010
		E_{rat} C	0.238±0.010
		E_{rat} D	0.223±0.009

Table 4.4: Experimental results on the mean rapidity shifts of protons and deuterons normalized by the beam rapidity for various centrality selections in Ru + Ru collisions.

E$_{beam}$ (A GeV)	Particle Type	$\sigma_{NN}/\sigma_{NN}^{free}$ (EoS Type)	$\delta y_p/y_b$
0.4	Proton	5.0 (HM)	0.312±0.013
		2.0 (HM)	0.295±0.012
		1.0 (HM)	0.261±0.010
		0.5 (HM)	0.215±0.009
	Deuteron	5.0 (HM)	0.352±0.014
		2.0 (HM)	0.338±0.014
		1.0 (HM)	0.282±0.011
		0.5 (HM)	0.192±0.008
1.528	Proton	1.0 (HM)	0.282±0.011
		0.75 (HM)	0.267±0.011
		1.0 (SM)	0.271±0.011
		0.75 (SM)	0.259±0.010

Table 4.5: Mean rapidity shifts of protons and deuterons normalized by the beam rapidity from the IQMD calculations in Ru + Ru collisions. The impact parameter range is $b_{IQMD} \leq 1(2)$ fm for $0.4(1.528)A$ GeV.

E$_{beam}$ (A GeV)	$\delta y_p/y_b$	N_f	N_b	M_{pr}
0.4	0.256±0.011	9.45	6.14	0.21
1.528	0.259±0.010	24.59	10.20	0.41

Table 4.6: Mean rapidity shift of proton normalized by beam rapidity and the mixing parameter M_{pr}. $N_f(N_b)$ represents the number of projectile(target) nucleon in forward(backward) hemisphere. Results are for protons only in Ru + Ru collisions at $0.4A$ and $1.528A$ GeV for the most central collisions(E_{rat} A).

Chapter 5

Conclusions

In this thesis, the nuclear stopping phenomenon in ${}^{96}_{44}$Ru (${}^{96}_{40}$Zr) + ${}^{96}_{44}$Ru (${}^{96}_{40}$Zr) collisions are investigated at $0.4A$ and $1.528A$ GeV in details. The centrality dependence of the proton and deuteron rapidity distributions in Ru + Ru collisions at both energies show that more particles are concentrated at the mid-rapidity and the shape of the rapidity distributions are narrower for more central collisions. This finding is consistent with the partial transparency so we conclude that more stopping can be achieved in more central collisions. The mean rapidity shift normalized to the beam rapidity gives quantitative information about the shape of the rapidity distributions. The results of the mean rapidity shift normalized to the beam rapidity provide the same conclusion as the centrality dependence of the baryon rapidity distributions. From the comparison of the data with the IQMD calculations, the IQMD model can reproduce the experimental rapidity distributions for the most central collisions by using hard Equation-of-State with $\sigma_{NN} = \sigma_{NN}^{free}$ at $0.4A$ GeV. However, the higher energy data at $1.528A$ GeV require the soft Equation-of-State with $\sigma_{NN} = 0.75\ \sigma_{NN}^{free}$. This comparison indicates a possible change of the nuclear Equation-of-State and σ_{NN} between $0.4A$ and $1.528A$ GeV. The experimental data and the IQMD calculation with respective condition on the mean rapidity shift normalized by the beam rapidity agree well at both energies. From this model comparison, we find that the global equilibrium is not achieved even in the most central collisions at $0.4A$ and $1.528A$ GeV.

By using two isospin tracer methods, the information of nuclear stopping has been extracted without invoking any nuclear models. For the most central collisions that we can achieve in the experiment, the parameter R_p and R_z show partial transparency and incomplete mixing of the projectile and target nuclei at both energies. R_p increases faster at $1.528A$ GeV than at $0.4A$ GeV as a function of rapidity. R_z shows a larger opening angle at $1.528A$ than at $0.4A$ GeV. Both results confirm that the partial transparency and incomplete mixing effect in heavy-ion collisions are more pronounced at higher energies. This conclusion is consistent with the results from completely different analysis by the estimation of the ratio of the variances of the transverse to longitudinal particle rapidity distributions($vartl$) in symmetric collision systems at bombarding energies from $0.09A$ to $1.93A$ GeV [79] and by the comparison of the particle rapidity distributions between two asymmetry collision systems(Ca + Au and Au + Ca) at $1.5A$ GeV [95]. The experimental results on R_p and R_z agree well with the IQMD model calculations with hard Equation-of-State and $\sigma_{NN} \leq \sigma_{NN}^{free}$ at $0.4A$ GeV. However, R_p and R_z are not sensitive to the nuclear Equation-of-State and σ_{NN}, if it ranges between 0.75 σ_{NN}^{free} and σ_{NN}^{free}, at $1.528A$ GeV within the framework of the IQMD.

Finally, the projectile and target components of protons are determined by using R_z. After decomposition of the measured overall proton rapidity distributions, a shift between two deduced rapidity distributions emerge, and they are clearly demonstrating incomplete mixing of projectile and target nucleons. In addition, the shift between two deduced rapidity distributions is more dramatic at $1.528A$ GeV. In order to quantify the separation between the projectile and target rapidity distributions, the mixing parameter M_{pr} has been introduced. The value of M_{pr} at $1.528A$ GeV is about a factor of two larger than that at $0.4A$ GeV. We conclude that the degree of nuclear transparency at $1.528A$ GeV is a factor of two larger than that at $0.4A$ GeV for the most central collisions.

R_p for the π^-/π^+ ratio at $0.4A$ GeV was also investigated as a possible bias due to the nuclear stopping. It is consistent with unity within the quoted errors. R_p and R_z for the π^-/π^+ ratio at $1.528A$ GeV was also investigated. R_p and R_z for the π^-/π^+ ratio at this energy shows partial transparency effect, although the effect is relatively small. The experimental results of R_p and R_z for the π^-/π^+ ratio are compared with the IQMD model calculations at $1.528A$ GeV. We find that there is no sensitivity to the nuclear Equation-of-State and the nucleon-nucleon cross section within the framework of the IQMD.

Bibliography

[1] R. Stock, Phys. Rep. **135**, 259 (1986).

[2] H. Stöcker and W. Greiner, Phys. Rep. **137**, 277 (1986).

[3] J. Stachel and G. R. Young, Annu. Rev. Nucl. Part. Sci. **42**, 537 (1992).

[4] P. Senger and H. Ströbele, J. Phys. **G 25**, R59 (1999).

[5] G. F. Bertsch, H. Kruse, and S. Das Gupta, Phys. Rev. **C 29**, R673 (1984).

[6] L. P. Csernai, Introduction to Relativistic Heavy Ion Collisions, Jone Wiley & Sons Ltd. (1994).

[7] P. Danielewize *et al.*, Phys. Rev. Lett. **81**, 2438 (1998).

[8] G. Peilert, H. Stöcker, W. Greiner, A. Rosenhauer, A. Bohnet and J. Aichelin, Phys. Rev. **C 39**, 1402 (1989).

[9] J. Aichelin, Phys. Rep. **202**, 233 (1991).

[10] Q. Pan and P. Danielewize, Phys. Rev. Lett. **70**, 2062 (1993).

[11] C. Hartnack, Rajeev K Puri, J. Aichelin, J. Konopka, S. A. Bass, H. Stöcker, and W. Greiner, Eur. Phys. J. **A 1**, 151 (1998).

[12] S. J. Yennello *et al.*, Phys. Lett. **B 321**, 15 (1994).

[13] H. Johnston *et al.*, Phys. Lett. **B 371**, 186 (1996).

[14] H. Johnston *et al.*, Phys. Rev. **C 56**, 1972 (1997).

[15] Nucl. Phys. **A 693**, (2001), special volume, edited by I. Tanihata.

[16] Isospin Physics in Heavy-Ion Collisions at Intermediate Energies, edited by Bao-An Li and W. Udo Schöder, Nova Science, New York (2001).

[17] B. A. Li, C. M. Ko, and W. Bauer, Int. J. Mod. Phys. **E 7**, 147 (1998).

[18] B. A. Li, Phys. Rev. **C 67**, 017601 (2003).

[19] W. Reisdorf and H. G. Ritter, Annu. Rev. Nucl. Part. Sci. **47**, 663 (1997).

[20] N. Herrmann, J. P. Wessels, and T. Wienold, Annu. Rev. Nucl. Part. Sci. **49**, 581 (1999).

[21] A. Andronic *et al.*, FOPI Collaboration, Phys. Rev. **C 67**, 034907 (2003).

[22] A. Andronic *et al.*, FOPI Collaboration, Nucl. Phys. **A 679**, 765 (2001).

[23] P. Crochet *et al.*, FOPI Collaboration, Nucl. Phys. **A 627**, 522 (1997), Nucl. Phys. **A 628**, 687 (1997).

[24] P. Crochet *et al.*, FOPI Collaboration, Nucl. Phys. **A 624**, 755 (1997).

[25] S. C. Jeong *et al.*, FOPI Collaboration, Phys. Rev. Lett. **72**, 3468 (1994).

[26] G. E. Brown, Phys. Rep. **163**, 167 (1998).

[27] C. M. Ko and G. Q. Li, J. Phys. **G 22**, 1673 (1996).

[28] A. Mangiarotti *et al.*, FOPI Collaboration, Nucl.Phys. **A 714**, 89 (2003).

[29] P. Crochet *et al.*, FOPI Collaboration, Phys. Lett. **B 486**, 6 (2000).

[30] K. Wisniewski *et al.*, FOPI Collaboration, Eur. Phys. J. **A 9**, 515 (2000).

[31] D. Best *et al*, FOPI Collaboration, Nucl. Phys. **A 625**, 307 (1997).

[32] J. Ritman *et al.*, FOPI Collaboration, Z. Phys. **A 352**, 355 (1995).

[33] C. Hartnack, Ph. D. thesis, GSI-report 93-05, (1993).

[34] S. A. Bass, C. Hartnack, H. Stöcker, and W. Greiner, Phys. Rev. **C 51**, 3343 (1995).

[35] J. Cleymans and K. Redlich, Phys. Rev. **C 60**, 054908 (1999).

[36] P. Braun-Munzinger, J. Stachel, J. P. Wessels, and N. Xu, Phys. Lett. **B 344**, 43 (1995).

[37] P. Braun-Munzinger, K. Redlich, and J. Stachel, GSI-Preprint 2003-13 (2003).

[38] H. Stöcker and W. Greiner, Phys. Rev. Lett. **44**, 725 (1980).

[39] B. Hong *et al.*, FOPI Collaboration, Phys. Rev. **C 57**, 244 (1998), Phys. Rev. **C 58**, 603 (1998).

[40] J. Barrette *et al.*, E814 Collaboration, Phys. Rev. **C 50**, 3047 (1994).

[41] J. Barrette *et al.*, E877 Collaboration, Phys. Rev. **C 62**, 024901 (2000).

[42] I. G. Bearden *et al.*, NA44 Collaboration, Phys. Lett. **B 388**, 431 (1996).

[43] H. Appelshauser *et al.*, NA49 Collaboration, Phys. Rev. Lett. **82**, 2471 (1999).

[44] W. Reisdorf *et al.*, FOPI Collaboration, Nucl. Phys. **A 612**, 493 (1997).

[45] H. H. Gutbrod *et al.*, Plastic Ball Experiment, Z. Phys. **A 337**, 57 (1990).

[46] S. A. Bass, J. Konopka, M. Bleicher, H. Stöcker, and W. Greiner, GSI Scientific Report. 94-1, 66 (1995).

[47] A. Hombach, W. Cassing, and U. Mosel, Eur. Phys. J. **A 5**, 77 (1999).

[48] B. Hong *et al.*, FOPI Collaboration, Phys. Rev. **C 66**, 034901 (2002).

[49] A. Gobbi *et al.*, FOPI Collaboration, Nucl. Inst. Meth. **A 324**, 156 (1993).

[50] J. Ritman for the FOPI Collaboration, Nucl. Phys. (Proc. Suppl.) **B 44**, 708 (1995).

[51] J. P. Alard *et al.*, FOPI Collaboration, Phys. Rev. Lett. **69**, 889 (1992).

[52] M. Eskef *et al.*, FOPI Collaboration, Eur. Phys. J. **A 3**, 335 (1998).

[53] N. Herrmann for the FOPI Collaboration, Nucl.Phys. **A 610**, 49 (1996).

[54] Ch. Plettner, Ph. D. thesis, Technische Universität Dresden, Germany (1999).

[55] R. Kutsche, Ph. D. thesis, Technische Universität Darmstadt, Germany (2000).

[56] W. Leo, Thchniques for Nuclear and Particle Physics Exp., Springer-Verlag Berlin, Germany (1987).

[57] W. Blum and L. Rolandi, Particle Detection with Drift Chambers, Springer-Verlag Berlin, Germany (1993).

[58] K. Hagiwara *et al.*, Particle Data Group, Phys. Rev. **D 66**(Review of Particle Physics), 010001 (2002).

[59] G. Goebels, Ph. D. thesis, Ruprecht-Karls-Universität Heidelberg, Germany (1995).

[60] A. Andronic, Ph. D. thesis, NIPNE Bucharest, Romania (1998).

[61] T. Kress, Ph. D. thesis, Technische Universität Darmstadt, Germany (2002).

[62] D. Best, Master thesis, Universität Mainz, Germany (1993).

[63] D. Best, Ph. D. thesis, Ruprecht-Karls-Universität Heidelberg, Germany (1996).

[64] C. Pinkenburg, Ph. D. thesis, Ruprecht-Karls-Universität Heidelberg, Germany (1995).

[65] GEANT User's Guide, CERN Program Library, CERN Geneva, Switzerland (1994).

[66] A. Devismes, Ph. D. thesis, Technische Universität Darmstadt, Germany (2001).

[67] F. Rami *et al.*, FOPI Collaboration, Phys. Rev. Lett. **84**, 1120 (2000).

[68] P. Danielewize and G. Odyniec, Phys. Lett. **B 157**, 146 (1985).

[69] M. Stockmeier, Ph. D. thesis, Ruprecht-Karls-Universität Heidelberg, Germany (2003).

[70] B. Hong *et al.*, FOPI Collaboration, preparation for the publication at Phys. Rev. .

[71] J. Harris *et al.*, Streamer Chamber Experiment, Phys. Lett. **B 153**, 377 (1985).

[72] J. Harris *et al.*, Streamer Chamber Experiment, Phys. Rev. Lett. **58**, 463 (1987).

[73] D. Pelte *et al.*, FOPI Collaboration, Z. Phys. **A 357**, 215 (1997).

[74] D. Pelte *et al.*, FOPI Collaboration, Z. Phys. **A 359**, 55 (1997).

[75] A. Wagner *et al.*, KaoS Collaboration, Phys. Lett. **B 420**, 20 (1998).

[76] J. Gosset *et al.*, Plastic Ball Experiment, Phys. Rev. **C 16**, 629 (1977).

[77] P. J. Siemens and J. O. Rasmussem, Phys. Rev. Lett. **42**, 880 (1979).

[78] M. A. Lisa *et al.*, EOS Collaboration, Phys. Rev. Lett. **75**, 2662 (1995).

[79] W. Reisdorf *et al.*, FOPI Collaboration, Submitted to Phys. Rev. Lett.

[80] A. Schüttauf *et al.*, ALADIN Collaboration, Nucl. Phys. **A 607**, 457 (1996).

[81] W. Reisdorf *et al.*, FOPI Collaboration, Submitted to Phys. Lett. B.

[82] W. Reisdorf *et al.*, FOPI Collaboration, Private communication.

[83] W. Scheid, H. Müller, and W. Greiner, Phys. Rev. Lett. **32**, 741 (1974).

[84] C. Pinkenburg *et al.*, E895 Collaboration, Phys. Rev. Lett. **83**, 1295 (1999).

[85] G. Stoicea *et al.*, FOPI Collaboration, Phys. Rev. Lett. **92**, 072303 (2004).

[86] C. Sturm *et al.*, Kaos Collaboration, Phys. Rev. Lett. **86**, 39 (2001).

[87] C. Fuchs, A. Faessler, and E. Zabrodin, Phys. Rev. Lett. **86**, 1974 (2001).

[88] F. Videbæk and O. Hansen, Phys. Rev. **C 52**, 2684 (1995).

[89] B. B. Back *et al.*, E917 Collaboration, Phys. Rev. Lett. **86**, 1970 (2001).

[90] D. Ouerdane *et al.*, BRAHMS Collaboration, nucl-ex/0403049, to be published in the Proceedings of the Quark Matter 2004 Oakland (US).

[91] B. A. Li, and S. J. Yennello, Phys. Rev. **C 52**, R1746 (1995).

[92] W. Benenson *et al.*, Phys. Rev. Lett. **43**, 683 (1979).

[93] S. Nagamiya *et al.*, Phys. Rev. **C 24**, 971 (1981).

[94] B. Hong *et al.*, FOPI Collaboration, Phys. Lett. **B 407**, 115 (1997).

[95] O. Hartmann, Ph. D. thesis, Technische Universität Darmstadt, Germany (2003).

Acknowledgements

First of all, I am grateful to Prof. Dr. Byungsik Hong, my thesis advisor, for his countless advice, support, and encouragement during all my graduate study. Based on his patience, I was able to complete this thesis. His understanding, enthusiasm, and passion of physics have been inspiring and stimulating me to reach this point.

I would like to express special thanks to Prof. Dr. Kwang Souk Sim for his continuous guidance. I appreciate also the committee members of Ph. D. thesis, Prof. Dr. Su Houng Lee at Yonsei University, Prof. Dr. In Kwon Yoo at Pusan National University, and Prof. Dr. Jungil Lee at Korea University.

I want to thank Prof. Dr. Peter Braun-Munzinger, the head of KP I at GSI, for giving me the chance to work and study at GSI. I have to appreciate to all members of FOPI Collaboration for their hospitality and support. Especially, Prof. Dr. Norbert Herrmann gave me encouragement and motivation to keep doing my project. Dr. Klaus D. Hildenbrand helps me to understand detector working principles from the basic to details. Dr. Yvonne Leifels produced all IQMD events in this thesis and it helped me a lot to understand my analysis in the side of nuclear transport model. Dr. Willibrord Reisdorf, Dr. Anton Andronic, Dr. Philippe Crochet and Dr. Andreas Schüttauf gave me their interest about my analysis and fruitful advice. Dr. Olaf N. Hartmann, Dr. Marek Kirejczyk shared an office and they provided for nice atmosphere. Dr. Victor Simion took care of me a lot and gave me wise man's wisdom, like my grandfather. I thank other collaboration members, Prof. Dr. Mihai Petrovici, Dr. Gabriel Stoicea, Dr. Zoltan Fodor, Dr. Jozsef Kecskemeti, Prof. Dr. Nicole Bastid, Xavier Lopez, Zbigniew Tyminski, Dr. Zhi Gang Xiao, Dr. Pjotr Koczon, Dr. Ralf Kusche, Dr. Christian Finck, Dr. Anne Devismes, Dr. Adriano Gobbi, Dr. Tarek Kress, Dr. Roland Kotte, Everard Cordier, M. Lotfi Benabderrahmane, Dr. Alessio Mangiarotti, Markus Mershmeyer, Dr. Marc Stockmeier, Prof. Dr. Dietrich Pelte, Dr. Alexander Lebedev, Dr. Alexander Zhilin, Igor Yushmanov, Prof. Dr. Fouad Rami, Dr. Brunon Sikora, Prof. Dr. Krystyna Siwek-Wilczynska, Dr. Krysztof Wisniewski, Dr. Zoran Basrak, Dr. Roman Caplar, Igor Gasparic, and Dr. Milorad Korolija, for their support. In addition, I thank Mrs. Gertraude Eisold, the secretary of KP I, for remarkable support. Thank you all.

I thank to all former and present members of Nuclear Physics Group at Korea University, Dr. Kyong Sei Lee, Dr. Seok Jae Lee, Jintae Yang, Kyungmin Baik, Wooyoung Jang, Donghee Kang, Donghwa Kang, Minjung Kweon, Sang Won Seo, Junyoung Park, Eunjin Choi, WooJin Park, Min Sang Ryu, Junyoung Suk, Hyun Ha Shim, Tae Im Kang, Dongho Kang, Dong Ho Moon, Byungil Kim, Kwangbok Lee, Mikiko Ito, and JiHyun Kim, for wonderful atmosphere. In addition, I thank many people at Korea University, please forgive me I can not write all names here, for sharing nice experiences during all my graduate study.

I thank you all my friends for keeping their interest about my graduate study.

I am grateful to my family, old sister, old brother, brother-in-law, sister-in-law, and four lovely nephews, for their love.

Finally, I am grateful to my parents for their endless love, support, and patience to their youngest son all the time only they can do. I hope that this small achievement can pay back to the part of the debt from my parents. Father and Mother, I love you.